Heat Assisted Magnetic Recording Media Based on Exchange Bias

Kelvin Elphick

DOCTOR OF PHILOSOPHY

UNIVERSITY OF YORK

PHYSICS

MAY 2016

Abstract

A study of a new paradigm for a heat assisted magnetic recording (HAMR) media based on the use of exchange bias is presented. Exchange bias occurs when an antiferromagnetic (AF) layer such as IrMn is grown in contact with a ferromagnetic (F) layer and the system if field cooled resulting in a hysteresis loop shifted along the field axis. In this concept the temperature dependent anisotropy is provided by IrMn. Therefore the information is stored in the AF layer and the recording layer is actually part of the read/write structure when field cooled. The F layer when magnetised, serves to align the F layer in the direction required to store the information and then provides a read out signal indicating in which direction the AF layer is oriented. Hence in a complex way the "recording layer" is actually part of the read/write head. The key to achieve a structure of this kind is the control of the orientation of the Mn ions of the IrMn such that they are aligned perpendicular to the plane of the film. In this way a perpendicular exchange bias required for information storage in the AF layer has been achieved. Over 300 samples have been prepared and evaluated to determine the optimised structure.

A segregated sample CoCrPt-SiO$_2$ was sputtered using a pressed powder target in a HiTUS deposition system. Dual Ru seed layers of 8nm and 12nm were deposited using 3mTorr and 30mTorr process pressure, respectively. The median grain size of D_m = (6.2 ± 0.2)nm was achieved using these sputtering conditions. High resolution cross section TEM imaging has been used to show that the CoCrPt grains remains segregated by SiO$_2$ after the deposition of IrMn.

The key feature of this media is that the recorded information is impossible to be erased by a demagnetising field. In order to achieve this requirement the hysteresis loop has to be completely shifted to a negative field. The highest shift or exchange bias of H_{ex} = (240 ± 5)Oe was measured at room temperature. This was achieved by depositing an ultrathin (0.8nm) Co interlayer above a Pt seed layer.

Contents

List of Figures

List of Tables

DECLARATION

I, Kelvin Elphick, declare that this thesis is a presentation of original work and I am the sole author. This work has not previously been presented for an award at this, or any other, University. All sources are acknowledged as References.

Chapter 1

Introduction

Since the areal density of perpendicular recording media (PRM) is approaching its limit, an alternative recording technology is required to increase the storage capacity in hard disk drives (HDDs). In conventional magnetic recording media the areal data density is limited by the thermal loss effect. The energy barrier that maintains the magnetisation orientation of a single domain particle is proportional to the anisotropy energy $K_U V_m$ where K_U is the anisotropy constant and V_m is the volume of the grain. In order to achieve high density storage and a high signal to noise ratio (SNR), the volume of the grains is reduced. Assuming that K_U remains constant the energy barrier is then reduced and leads to competition with thermal energy $k_B T$ where k_B is the Boltzmann's constant and T is temperature. Under these circumstances the magnetisation of the particle can reverse due to the demagnetising field of the bit and that from neighbouring bits even in the absence of an external magnetic field and this is the origin of the thermal loss effect, [1].

In order to improve thermal stability the value of K_U can be increased but this increases the required field to write the bit. This problem is known as the media-trilemma and is shown in Figure 1.1, [2].
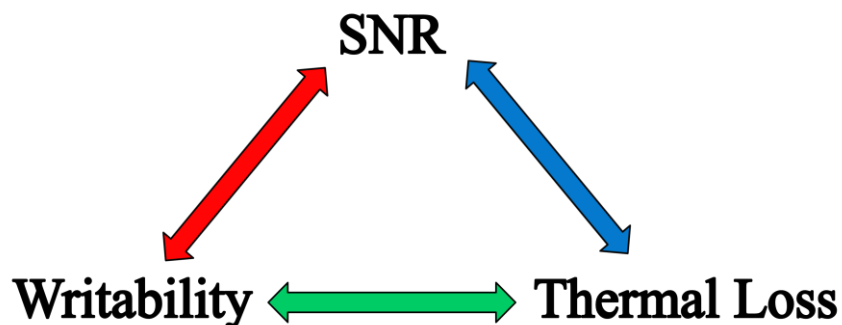
Figure 1.1 The media trilemma problem.

The areal density of current conventional HDDs is about 1TB/inch^2. In recent years because of availability of ion beam milling, significant advances in write head pole design have been made such that the peak value of field are achievable are now producing 1T, [3]. Several advanced recording media have been proposed to resolve the problem of lowering the write field: bit patterned magnetic recording (BPM), heat assisted magnetic recording (HAMR) and microwave assisted magnetic recording (MAMR) are the current future options for HDD storage. In BPM the information is stored in one single lithographically defined dot. Therefore the magnetic properties are highly dependent on the precision of the lithography process. However the main challenges for BPM is the cost of the fabrication process. The principle of HAMR and MAMR are similar to each other. They rely on an external energy which causes their grains to reverse their magnetisation during the "write" process.

It is generally accepted that the next step in the progression of magnetic information storage technology will be a move to a HAMR, [4]. Current information from the leading manufacturers of hard disc drives indicates that this technology should be in the market place within a year from the time of writing. The principle of HAMR is that a laser fed through a wave guide, delivers heat pulses via near field optics to the surface of a conventional disc with grains oriented in the usual perpendicular direction. The magnetocrystalline anisotropy of the material is thereby reduced enabling a conventional write head to switch the grains with a normal field pulse. Once the grains in the disc have been cooled, the anisotropy rises and allows a much higher data density of up to 4TB/inch^2 to be achieved as discussed by Weller et al., [4].

In all the systems currently under development the material of choice for the recording layer in the disc is based on the FePt alloy. The reason for this choice of material is because the bulk alloy FePt has extremely high magnetocrystalline anisotropy have reported to lie between 5 - $7x10^7$ergs/cc with a strong temperature dependence. Furthermore the alloy in thin film form has a high magnetic moment of 800 emu/cc which is comparable to that of CoCrPt-based alloys used in conventional disc recording, [4]. The alloy is also corrosion resistant, [5].

The use of FePt in a disc structure is in essence no different to the typical structure used for a conventional Co-based recording medium. In the normal way a soft underlayer (SUL) is required for field focusing and an exchange break layer is also required to prevent the generation of intergranular coupling via the SUL. Hence in principle a disc based on FePt requires very limited development of new technology. However the major problem with FePt is the fact that when it is deposited by sputtering it crystallises in an fcc phase. Hence a phase transformation to the $L1_0$ structure must be undertaken in order to achieve the large magnetocrystalline anisotropy required for information storage. In order to achieve the $L1_0$ phase transition the substrate temperature used in the sputtering system were heated to approximately 500-550°C (~800K), [6].

A number of attempts have been made to reduce the required phase transition temperature by doping and varying deposition conditions, [7]. However none of these techniques have succeeded in lowering the transition temperature much closer to 600K which is the normal temperature limitation for magnetic multilayer stacks. This requirement to anneal FePt to achieve the necessary phase transition is one of the parameters inhibiting the full commercialisation of HAMR technology.

In this work we describe an alternative strategy for the development of HAMR media. In our approach the need for a storage material to have a temperature dependent anisotropy and to provide a read out signal are separated so that each function can be optimised independently. This is achieved by the use of an exchange bias structure where a conventional $CoPtCr-SiO_2$ recording layer is exchange biased to an underlayer of the AF IrMn so that heating and cooling in the exchange field from the recording layer results in a shifted loop. IrMn is the AF material with high anisotropy and consequence thermal stability. Hence this material is used in high technology devices.

Exchange bias occurs when a ferromagnetic (F) material is grown immediately adjacent to an antiferromagnetic (AF) material and the structure is field cooled from near the Néel temperature of the antiferromagnet. The coupling of the spins at the interface then results in a hysteresis loop which is asymmetric about the $H = 0$ axis. This shift in the hysteresis loop is characterised by the shift in the loop from

its centre to the $H = 0$ axis which is called the exchange field H_{ex} as shown in Figure 1.2.
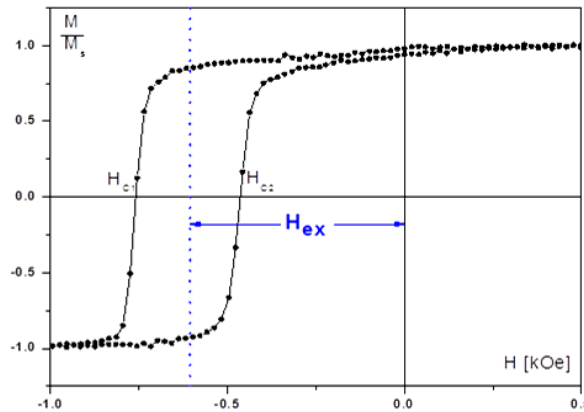
Figure 1.2 Hysteresis loop with exchange bias.

This strategy requires the re-orientation of the IrMn layer to allow coupling to the recording layer which has been achieved. Furthermore this re-orientation and the resulting exchange bias has been obtained in a recording layer with grain segregation by SiO_2. In this system the information is, in effect, stored in the AF layer and hence there is no demagnetising field generated by the stored bits. The conventional recording layer now becomes part of the read/write process to the AF layer. Furthermore for a loop shift where both values of coercivity lie to one side of the origin, the information can never be erased by the use of a magnetic field but only by a thermal process.

In order to achieve a proof of principle that such a system can be produced, it is necessary to achieve a number of well defined goals. The first of these is to show that it is possible to induce exchange coupling between the normal AF alloy used in exchange bias systems IrMn, to a conventional CoPtCr-SiO_2 recording medium. If such a coupling cannot be achieved and an exchange bias result, then clearly an alternative AF material or an alternative F material would have to be sought.

The second requirement for the system is that the texture of the IrMn be oriented in the perpendicular direction or in a direction such that an exchange bias can be induced in a material such as CoCrPt having perpendicular anisotropy. It is known that the effective anisotropy constant of an AF material such as IrMn is determined by the degree of texture of the (111) planes along which the Mn ions lie. In fact for an in-plane system it is possible to achieve almost perfect texture of the (111)

planes with a resulting measured value of the effective anisotropy constant of the IrMn of 2.9 x 10^7ergs/cc, this value comparable to that of an FePt thin film, [8].

The results presented in Chapter 7 show that this proof of principle has been achieved. However the loop shift to negative fields has not yet been achieved but a system has been developed that cannot be demagnetised by a reverse magnetic field alone.

1.2 Units

The use of cgs units has been adopted in this study which is used for all the results and equations which are presented. These units are widely used in the majority of the applied magnetism community. Most of the work by research groups and the magnetic recording industry are presented in cgs units.

Chapter 2

Principles of Magnetic Recording

The media configuration for heat assisted magnetic recording (HAMR) is similar to a conventional perpendicular recording media (PRM). The key components in conventional PRM are the read head and the recording medium. The read head uses the Tunnelling Magneto Resistance (TMR) effect to sense the transitions. Exchange bias is used in the head to pin the reference ferromagnetic (F) layer. $CoCrPt-SiO_2$ has a high perpendicular anisotropy and hence is used for the recording layer. It is deposited on top of an underlayer which is used to induce the desired crystallographic orientation to the recording layer. This chapter describes the theory and structure of recording media.

2.1 History of Magnetic Disk Recording

When IBM introduced the random access method of accounting and control as the first commercial computer, a magnetic recording device was used to store the information, [9]. The first generation of hard disk drives (HDDs) stored the information on iron oxide particles using was called the RAMCK. A longitudinal recording HDD was then invented and the information was stored as a magnetisation pattern in the plane of the disk in what is known as longitudinal recording. The information was written onto the recording layer using a horseshoe like inductive write head. Simply by applying an electric current through the write element the induced magnetic field magnetised the recording layer. Initially the signal was read back using an anisotropic magnetoresistance (AMR) element but it was then replaced by a giant magnetoresistance (GMR) read sensor which measured the transition between each north to south (N-S) or south to north (S-N)

region. The signal was then transformed into a digital readback signal. A schematic diagram of the system is shown in Figure 2.1.
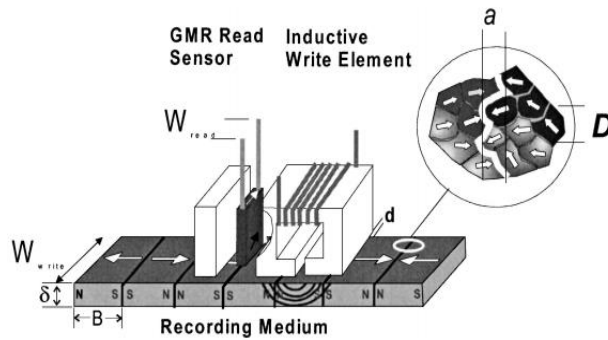
Figure 2.1 Schematic diagram of longitudinal recording system, [9].

Due to the capacity demands of HDDs there was a requirement to increase the areal density of the recording medium. This can be simply achieved by reducing the track width W_{write} and bit length B_L. However the drawback of reducing such parameters is the influence on the single to noise ratio (SNR). The SNR can be estimated via Equation (2-1), [9]. Therefore in order to maintain the device operation at high SNR, it is necessary to reduce the grain diameter D.

$$SNR \approx \frac{W_{write}B^2}{\alpha^2 D^2 (1+\sigma^{*2})}$$ (2-1)

where σ^* is the normalised grain size distribution and α is ratio of the transition width to the grain diameter a/D, [10].
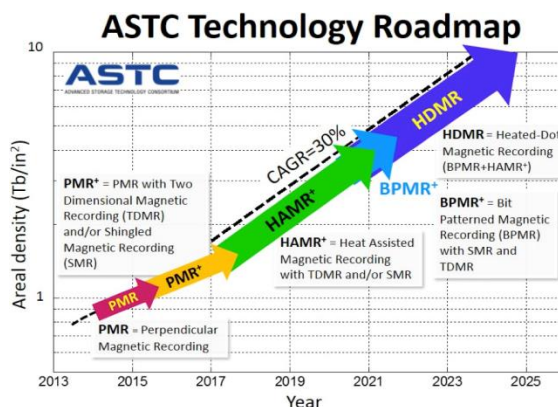
Figure 2.2 The areal density of HDD, [11].

Figure 2.2 shows a schematic diagram of the areal density of HDD products from 2013 to 2025. From 2014 perpendicular recording has been used for storage. However this recording technique cannot be used indefinitely to increase the areal density of HDD. Therefore heat assisted magnetic recording and heated-dot magnetic recording are predicted to be used to expand the areal density further.

Longitudinal recording approached its limit after 2000. This is due to the thermal stability issue which originated in the reduction of the grain size. Also the reduced bit length increases the demagnetising field from each bit and the bit-to-bit effect reducing the energy barrier, [12]. The energy barrier of a grain to reversal is given by [13]

$$\Delta E = K_U V_m \left(1 - \frac{H_D}{H_K}\right)^2 \tag{2-2}$$

where K_U is anisotropy constant, V_m the grain volume, H_D the demagnetising field and H_K the anisotropy field. Perpendicular recording was then developed to tackle the demagnetisation field issue based on the orientation of each bit. (See section 2.2.1).

2.2 Current & Alternative Magnetic Recording

2.2.1 Perpendicular Recording

Longitudinal recording media (LRM) generates a large demagnetisating field from bit to bit. Therefore the areal density of such media was limited. Perpendicular recording media (PMR) became an alternative option to replace LRM. In the 1970s Iwasaki and Nakamura introduced most of the basic ideas of PRM, in order to resolve the demagnetisation field problem which reduced the capacity in LRM, [14] [15] [16]. The criteria is that the anisotropy field H_K has to be greater than the demagnetisation field H_D. Since $H_K > H_D$ and $H_K = 2K_U/M_s$ and $H_D = 4\pi M_s$, hence $K_U > 2\pi M_s^2$.

The main difference between PRM and LRM is the orientation of the recorded bits. The reliability of PRM relies on a significant reduction of the demagnetisation field

at high density. This is based on the flux closure between neighbouring bits with opposite polarity. Another feature introduced by PRM was the soft underlayer (SUL) which improved the write field. Unlike LRM the write head of PRM was modified to a single pole head to utilise the advantages provided by the SUL. The purpose of the SUL is to create a magnetic mirror image of the write head under the intermediate layer. The image created by the SUL has the opposite polarity to that of the write head. Therefore it conducts the magnetic flux lines from the write head to the image in order to create a field large enough to overcome the high anisotropy of the grains for thermal stability.

Figure 2.3 shows a schematic diagram of PRM. A typical perpendicular recording medium consists of three different functional layers; recording, intermediate and soft magnetic underlayers. As discussed in the previous paragraph, the main purpose of the SUL was to improve the write field. This is achieved by the creation of a magnetic mirror image of the single pole write head in the SUL hence focusing field line. Alloy materials such as NiFe, FeTaC and CoTaZr are used as the SUL, [17]. However the SUL also generates a significant amount of noise which reduced the SNR of the media. In the absence of a magnetic field the SUL forms a domain structure to minimise the magnetostatic energy. The domain walls generate a signal to the head causing noise. One of the ways to resolve this problem is by depositing a Ru layer between the SUL and the recording layer. The advantages of this are it induces a hexagonal texture to orientate in the Co-alloy perpendicular direction and acts as an exchange break layer to stop the coupling between the recording layer and the SUL. Until 2009 there were a number of studies to resolve the noise issues. Eventually this issue was resolved by pinning the magnetisation orientation along the surface. This can be achieved using a harder magnetic material or an antiferromagetic material to pin the SUL surface as discussed by Piramanayagam et al. and references therein, [17].
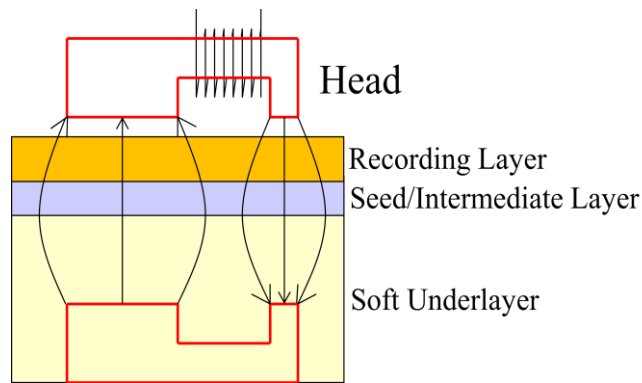
Figure 2.3 Schematic diagram of a cross section view of PRM write and read process.

A thin intermediate layer is deposited on top of the SUL. This layer provides multiple functionalities to the medium such as exchange decoupling between the SUL and the recording layer and provides an ideal texture for the recording layer growth. When the SUL is in intimate contact with the recording layer, the magnetic properties of both layers will be changed due to exchange interactions. For instance the coercivity of the recording layer is reduced. In practice to avoid noise generated by domain wall in the SUL a synthetic AF structure is used consisting of two F layers separated by a thin non magnetic layer so as to create anti-parallel alignment. Another purpose is to create epitaxial growth for the recording layer. The CoCrPt alloy has an hexagonal close-packed (hcp) crystal structure. For PRM it is essential to orientate the c-axis of the alloy perpendicular to the plane. Therefore the intermediate layer should have an hcp (002) or fcc (111) plane orientated perpendicular to the plane. Ru is one of the commonly used materials as an interlayer due to its hcp crystal structure, [17]. Recently an intermediate layer has also been used to provide an additional function of lateral exchange decoupling between grains. An extra Ru layer was sputtered on top of the first Ru layer using high Ar pressure. Void structures were then created which allows an insulating material such as SiO_2 to fill the gap when co-sputtered with the CoCrPt alloy, [18].

The recording layer is the most important layer for the media and has a typical thickness of 20 nm. This is the layer where the information is stored. The materials that are used in this layer have several required properties such as crystal structure, thermal stability and grain size distribution. In the late 1970s CoCr alloys were first proposed as recording layers due to their high uniaxial anisotropy perpendicular to

21

the plane, [17]. Cr was used to reduce the grain size, increase corrosion resistance and exchange decouple the grains when sputtered at high temperatures. It forms a partially non-magnetic grain boundary to enhance exchange decoupling between the grains. There were a numbers of studies regarding the introduction of a third element to the CoCr alloys such as Nb, Pt and Ta, [17]. Nowadays co-sputtered CoCrPt-SiO$_2$ is the material of choice for recording layers. Figure 2.4 shows a typical in-plane TEM image of CoCrPt-SiO$_2$ system with the grain size of 6.3nm
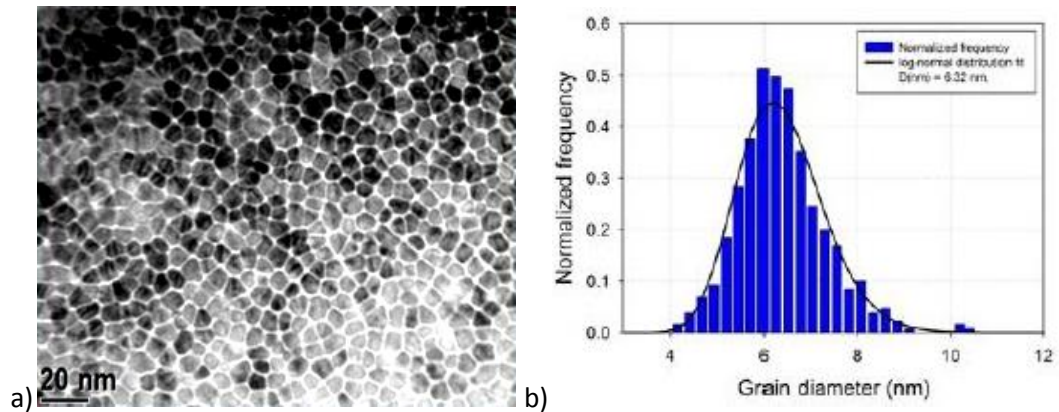
Figure 2.4a) In-plane TEM images of CoCrPt-SiO$_2$ grain structure b) its size distribution, [19].

Co provides an hcp crystal structure and perpendicular orientation of the media. Pt atoms locate at the middle of the lattice and stretch the c-axis lattice parameter to increase the anisotropy constant, hence increasing the thermal stability. However excessive Pt results an fcc structure in CoPt alloys above about 25 at%., [18]. An fcc structure reduces the anisotropy of the alloys, therefore the concentration of Pt usable is limited. SiO$_2$ is co-sputtered simultaneously with CoCrPt alloys using composite targets. The CoCrPt crystallises and forms a grain structure with a typical grain diameter of 6 – 8nm, while the SiO$_2$ is trapped between the grains. The width of the segregation is about 1nm. SiO$_2$ is a very good electrical insulator and prevents the Ruderman-Kittel-Kasuya-Yosida (RKKY) interaction. (See section 3.6) The medium is capped using a diamond-like carbon layer. This is used to protect the medium from mechanical damage by the write head.

2.2.2 Coupled Granular Continuous Recording Media

Coupled granular continuous (CGC) recording media is one form of PRM. The areal density of a conventional PRM was extended to 500 GB/inch^2 via increasing the

magnetocrystalline anisotropy or reducing the grain size in the film. However the capacity of PMR media is restricted by the thermal stability of the medium and SNR. Other challenges came from the distribution of the easy axis orientation, which leads to a large transition width a_0.

In 2001 Sonobe et al. [20] purposed the idea of coupled granular, continuous recording media. The principle of this idea was to combine an individual small grain layer with a perpendicular magnetically continuous layer as shown in Figure 2.5a, b. Two different types of continuous layer were used in this system. One of them was a stacked or capped media using a single thin layer of CoCrPtB, [21]. The other was a (Co/Pt) or (Co/Pd) multilayer system. These continuous layers provide a large advantage to PMR due to the strong pinning effect on the granular layer.
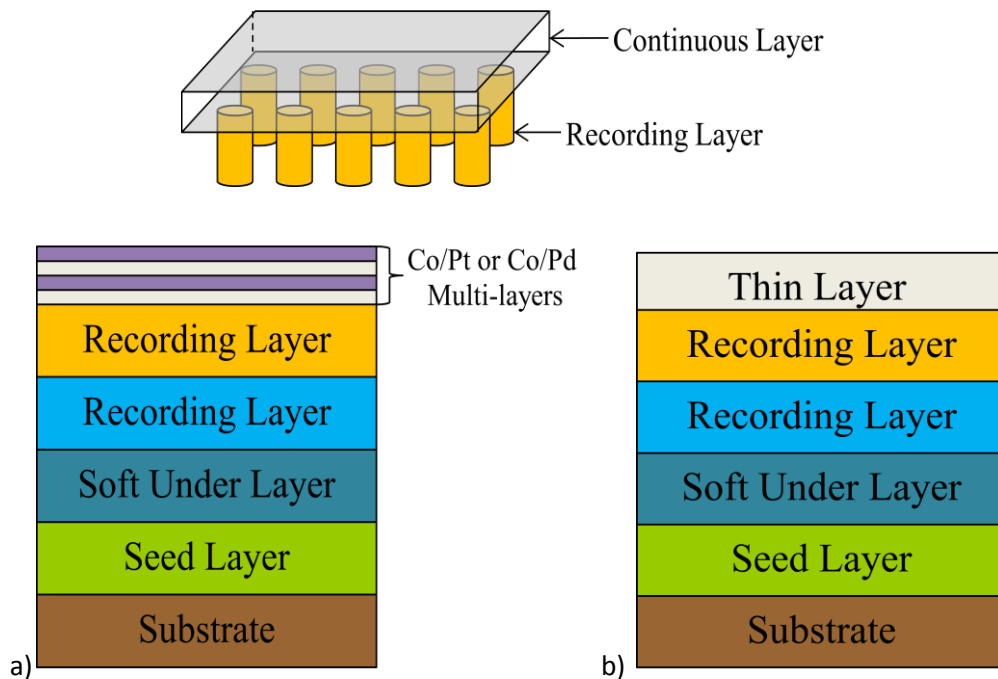
Figure 2.5 Schematic diagrams of CGC media structure with a) multilayer b) a thin continuous layer.

The main features of CGC media are an improved thermal stability and SNR for the medium. Therefore the grains size can be smaller and support a higher areal density. Tham et al. [22] showed that the SNR of CGC media was improved by depositing Co/Pd multilayers as a continuous layer on top of a granular CoCrPt-SiO$_2$ magnetic layer. This was due to transition smoothing and domain wall pinning effects. [23]

The grains in the granular layer are taken to have a cylindrical geometry and are oriented perpendicular to the plane. The interfacial exchange energy E_{iex} that is required to reverse a cylindrical grain can be calculated from [24]

$$E_{iex} = \frac{A_{ex}\pi D^2}{a} = \frac{M_s H_{iex} V_m}{2}$$

(2-3)

where A_{ex} is the exchange stiffness, D the grain diameter, a the lattice constant, M_s the saturation mangetisation of the grain, H_{ex} the interfacial exchange field and V_m the volume of the grain. Re-arranging Equation (2-3) the exchange field can be defined as

$$H_{iex} = \frac{8A_{ex}\pi}{a\delta_t M_s}$$

(2-4)

where δ_t is the thickness of the granular layer. Sonobe et al. [24] studied the energy barrier $K_U V_m / k_B T$ as a function of the interlayer exchange interaction, where K_U is the anisotropy constant, V_m the grain volume, k_B Boltzman's constant and T the temperature. The results showed that if the value of K_U for the granular layer is about 5 x 10^6ergs/cc, the grains can be stable at a data density of 1TB/inch² ($\frac{K_U V_m}{k_B T} \approx$ 60) with a low exchange field of only 4kOe required as shown in Figure 2.6. This is a significant result to show that the exchange field can be reduced with high K_U in CGC media. The other advantage of CGC media is that it increases the coercivity leading to a reduction of the transition width which is given approximately by [25]

$$a_0 = \frac{M_r \delta_{med}}{H_c}$$

(2-5)

where M_r is the remanent magnetisation, δ_{med} the thickness of the medium and H_c the coercivity. CGC media has been studied extensively in terms of the SNR and thermal stability and the fabrication is simple and low cost. Therefore it has the potential to replace conventional PRM and is already in production.
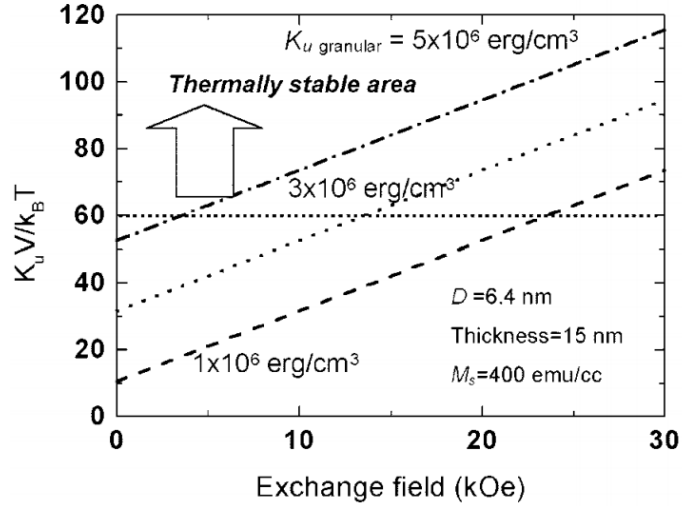
Figure 2.6 Dependence of $K_U V_m / k_B T$ as a function of exchange field for CGC media with different values of K_U, [24].

2.2.3 Exchange Coupled Composite Media

An alternative design of PRM was tilted media proposed in 2003 by Zou et al., [26]. The unique feature of tilted media is that the easy axis orientation of the grains is aligned at ~45° to the plane. Therefore the switching field required is reduced by half compared with conventional PRM following the Stoner-Wohlfarth model, [13]. Hence a material with higher K_U can be used. The comparison between conventional PMR and titled media is shown in Figure 2.7. The high anisotropy of the grains in the medium then give rise to data stability against thermal loss but there is also a loss of signal since only the perpendicular component of the magnetisation contributes to the change in the flux in the transition. Special seed layers would also be required to generate this orientation of the c-axis.
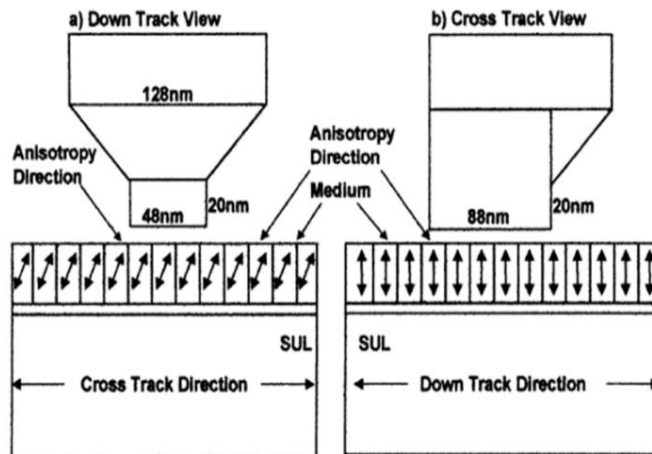
Figure 2.7 Schematic diagram comparing tilted and perpendicular media, [27].

In 2005 Shen, Victora and Suess et al. [28] [29] [30] proposed an alternative recording media called exchange coupled composite (ECC) media which consists of double layer grains. The principle of ECC media is to exchange couple a soft and hard magnetic material. The media also requires additional fabrication to achieve lateral exchange de-coupling between the grains. Therefore a columnar growth process is the key requirement of ECC media. The soft magnetic layer is located on top of the hard layer which acts as the storage layer. This layer consists of grains with a high anisotropy constant in order to remain thermally stable for a small grain size. The soft layer acts as a switching layer. The magnetisation of the soft layer is reversed when an external field is applied. The hard layer is then reversed to the same direction due to the exchange coupling effect at the interface. The magnetisation reversal of the bi-layer simply follows the Stoner-Wohlfarth model. Figure 2.8 shows a cross section TEM image of an ECC medium, [19]. The basal plane lattice matching between the Co-alloy layers are perfect and no boundaries were observed between the layers. This leads to direct exchange coupling between them and hence coherent switching. In this case the high coercivity layer was about 20nm and the soft layer about 16nm, [31].
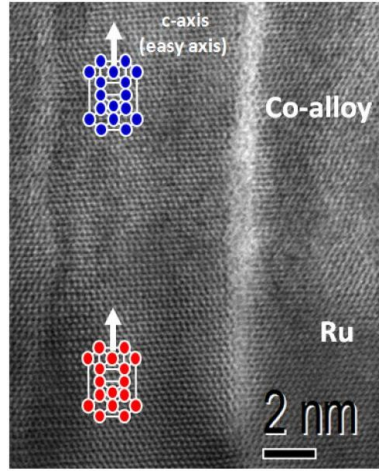
Figure 2.8 Cross section TEM for ECC media with the hcp structure, [19].

Assuming the grain has perfect alignment, the ratio of the energy barrier ΔE to the switching field H_S of ECC media can be calculated from

$$\zeta = \frac{2\Delta E}{V_m \, H_S M_S} \tag{2-6}$$

where V_m is the median grain volume, H_S the switching field, M_S the saturation magnetisation and ΔE is the energy barrier. ζ is the effective figure of merit for thermal stability of the data. Increasing the value of ζ improves the thermal stability and writability of the media. For instance tilted media has a ζ value of 2 and conventional PRM has a value of 1. Assuming both media have the same thermal stability. PRM requires twice the switching field of tilted media. The Laudau-Lifshitz-Gilbert (LLG) equation has been used to simulate the switching process of ECC media. The optimised value of ζ was very close to 2, [29].

In 2005 a successful experimental study of ECC media was undertaken by Wang et al. [31] using FeSiO as the soft layer and [Co-PdSiO]$_n$ as the hard layer. The results showed that the writability was dramatically improved using ECC media and the switching field of the media was less sensitive to the angular dispersion of the easy axes of the grains compared with PRM. A high coercivity alloy in the $L1_0$ phase such at FePt, CoPt and MnAl were reported to have thermally stable grains with grain diameters of about 4nm, [32]. A high saturation magnetisation soft layer material is required, and one of the most commonly used alloys is FeSiO, [33]. Lattice matching

between the soft and hard layer is also an important consideration for the selection of materials.
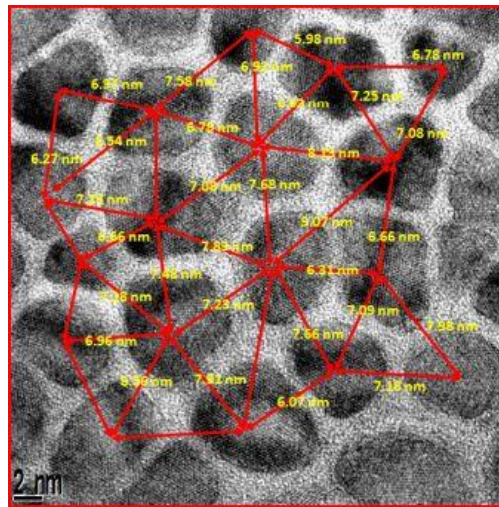
Figure 2.9 Bright field TEM image of an ECC media, [19].

Figure 2.9 shows a grain structure of a conventional ECC media, [19]. The thickness of the hard layer and the soft layer are 9nm and 5nm, respectively. A conventional recording material CoCrPt is used as the hard layer. Each grain was separated by SiO_2 to control the exchange coupling. One of the most important characteristics of ECC media is the easy axis dispersion which directly affects the switching field distribution $(f(H_S))$ of the medium. Based on the Stoner-Wohlfarth theory a deviation of 10° leads to a reduction of H_S of a single grain of 30% as shown in Figure 2.10, [13].

In order to improve the thermal stability of the media, a narrow distribution of easy axis orientation is required. There was an experimental study which reported that the distribution of the easy axis orientation is between 3.31° − 3.37°. The measurements were done using a dc magneto-optical Kerr effect (MOKE), [19].
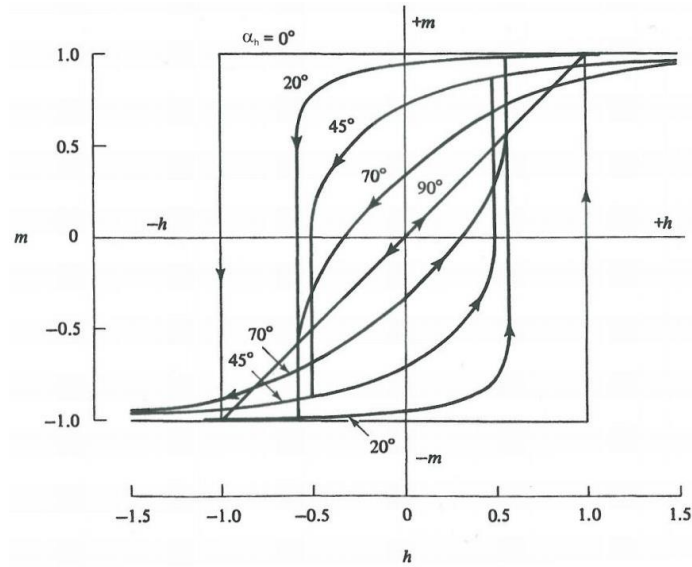
Figure 2.10 Magnetisation curves based on Stoner-Wohlfarth theory, [13].

2.3 Future Magnetic Recording Media

2.3.1 Bit Patterned Media

The idea of patterned media was proposed in 1990s, [34]. The unique structure in patterned media countered the thermal instability effect between grains. In conventional PRM the areal density can be enhanced by reducing the grain volume. If the grain size was reduced to sub-5nm the thermal loss effect occurs. This causes the grains to reverse under thermal fluctuations and leads to a loss of data as discussed by Terris and Thomson, [35].

Patterned media can be fabricated using nano-imprint lithography. Therefore each bit is stored in a single magnetic switching volume. The other concept of patterned media is to remove the need for servo track writing. Typical hard disk drives (HDDs) consist with servo track which was used to provide the position information for the write and read heads. However the area of the servo track occupies a significant fraction of the disk surface and as the track density of HDDs increases it takes up to 45 minutes to write the servo track, [36].

The critical problems of patterned media are the high cost of nano-imprint lithography and the precision of fabricating the bits on a circular track. There was a

prediction that the areal density of PRM can reach up to 1TB/inch^2, [11]. There are other alternative methods to increase the areal density such as microwave assistant magnetic recording (MAMR) and heat assisted magnetic recording (HAMR).

The principle of BPM is to increase the magnetic volume in order to improve the thermal stability of the media. In PRM and LRM a bit of information is stored in a statistical number of grains. However in BPM the information is stored in one single element. There are three different types of lithographically defined media: They are BPM, discrete track media (DTM) and patterned servo marks as shown in Figure 2.11, [35].
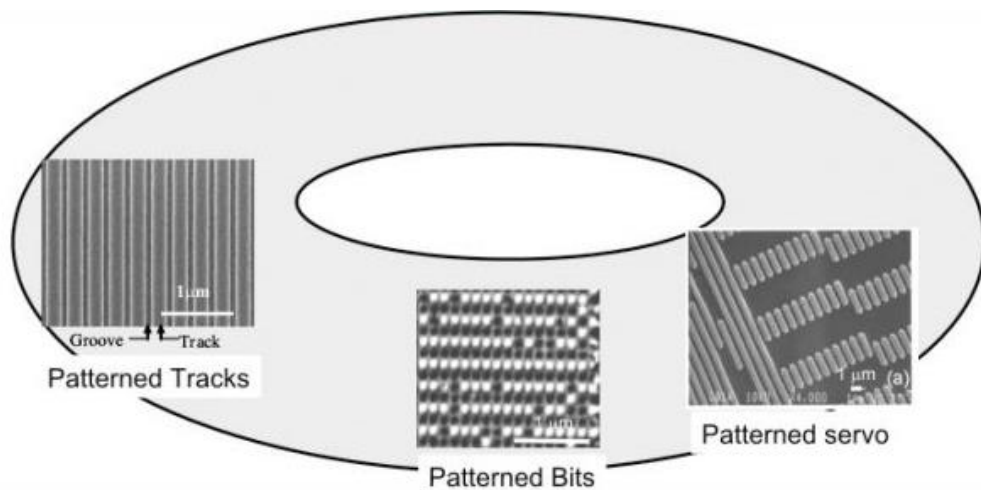
Figure 2.11 Patterned tracks and servo images taken by scanning electron microscope and patterned bit images taken by a magnetic force microscope, [35].

The first generation of prototype patterned media was a patterned servo. This media required a hard drive which contains between 1 to 6 disks run in a serial process. The recording process required the write head to fly over the surface of the disks and store the data in a servo mask. The drawback of this media is the time consuming and costly fabrication process. DTM requires a lithography patterned process to create "tracks" and each track is segregated using a non-magnetic material. Typical areal density of DTM can reach up to a few TB/inch^2 but cannot exceed 10 TB/inch^2, [37].

The areal density for BPM of up to 5TB/inch^2 was demonstrated by Kikitsu et al., [37]. The limit of the areal density for BPM is highly dependent on the dot size and it is possible to achieve more than 10TB/inch^2, [37]. For example a BPM density of 1,

5 and 10TB/inch^2 can be achieved using a bit pitch of 25 x 25nm^2, 11 x 11nm^2 and 7.9 x 7.9nm^2, respectively, [37]. The medium has to be patterned into discrete magnetic dots or islands using a lithography process. These magnetic areas are separated using a void or non-magnetic material. It allowed these structures to have strong exchange coupling so that the dots can act as a single domain which can store 1 bit of information as either a moment down or up. A schematic diagram of BPM and a comparison between BPM and PRM is shown in Figure 2.12.
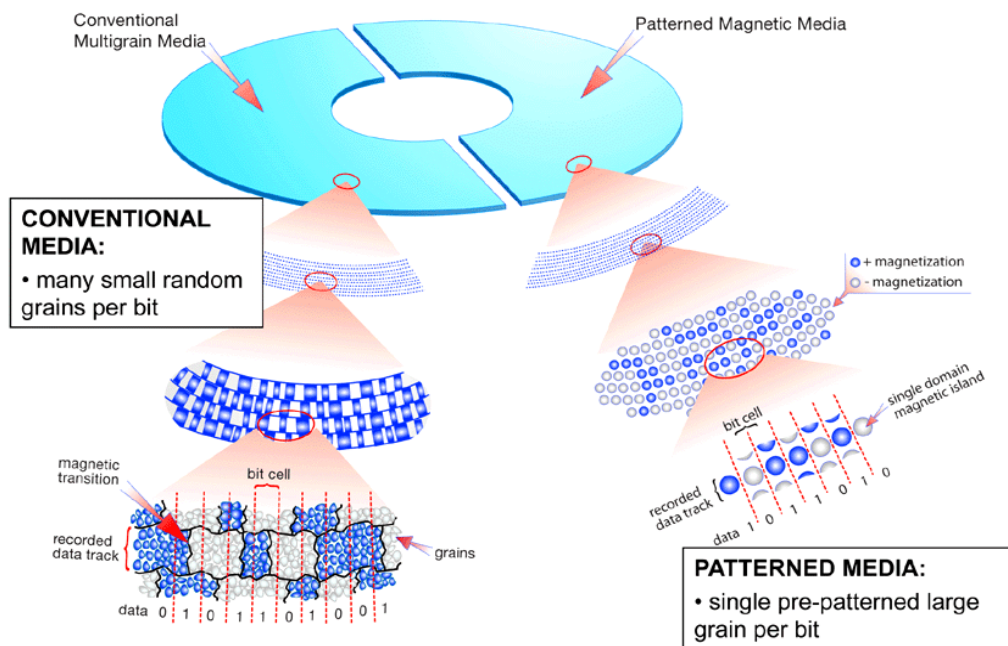
Figure 2.12 Comparsion between converntional media and patterned media, [38].

The magnetic properties of BPM are highly dependent on the precision of the lithography process of each dot and its location and size. Kamata et al., [39] demonstrated the distribution of coercivities of a CoCrPt BPM ranging from 0.5 – 6.0kOe as discussed by Kikitsu et al., [37]. X-ray diffraction rocking curve measurements were undertaken to analyse the distribution of the easy axis orientation of the element. The results showed that the easy axis deviated from dot by dot of up to 15° giving a change in switching field of approximately 36%, [13].

In ECC or continuous granular coupled media (CGC) there is no requirement to write data in a specific location. For instance ECC media requires about 10 - 20

grains to store a single bit. The SNR in such media was reduced by averaging the total number of grains across the transition width. In BPM the writing process requires synchronisation between the write head and the recorded bit. Therefore the shape and precision of the write head are highly restricted. The field gradient generated from the write head has the possibility to reverse neighbouring bits which leads to noise generation, [40].

2.3.2 Microwave Assistant Magnetic Recording

High areal density media requires high anisotropy materials to resolve the thermal stability issue. This defines the problem as being how to switch the materials at low switching field and fast enough to increase the data rate. In 2008 Zhu et al., [41] purposed a novel recording method called MAMR. The idea of this recording method is to introduce an external microwave field to the medium in order to improve the writing process.

In conventional PRM the head field has to be larger than the maximum switching field of the grains to saturate the medium. In a MAMR medium the saturation process can be achieved using a write field which is significantly below the medium coercivity. Therefore the medium is capable of high density recording. The first relevant experiment was demonstrated using a single Co nanoparticle. A significant reduction in the switching field was observed by applying an external ac field pulse, [42]. Few experimental demonstrations were reported as discussed by Shiroishi et al. [40] and references therein.

MAMR recording utilises the ferromagnetic resonance phenomenon. An external microwave alternating field H_{ac} is applied along a direction orthogonal to the write field which is parallel to the plane of the medium as shown in Figure 2.13. This alternating field is generated using a field generation layer (FGL). The microwave field is polarised in either an anticlockwise or clockwise orientation to align or reverse the grains respectively.

The precessional motion is initiated by an external microwave field with an amplitude of the order of kOe and a frequency calculated to be a few tens of GHz,

[40]. A significant reduction of switching field of a factor of 3 or 4 was observed, [43]. The medium absorbed the microwave energy if the ac field is matched to the F resonance frequency of the grain. This leads to a torque acting on the moment of the grain and initiates a precessional motion of the moment around its easy axis direction as shown in Figure 2.13. If the duration of the reversing field is sufficient this leads to an irreversible magnetisation reversal.
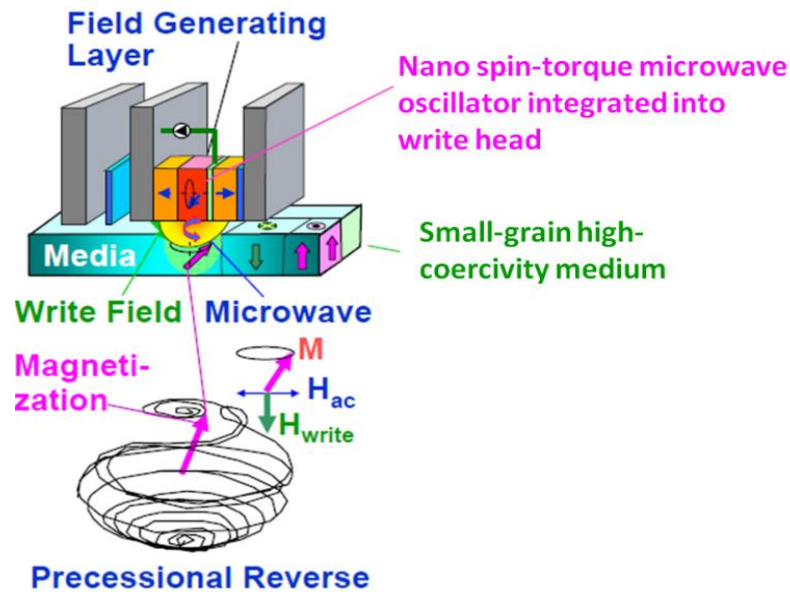
Figure 2.13 Schematic diagram of microwave assisted magnetic recording, [40].

The core of the MAMR system is the spin torque driven microwave oscillator. This oscillator structure was formed by a multilayer system. It consists of a perpendicular anisotropy layer which is used to polarise the injected current, a metallic interlayer, a FGL and a perpendicular anisotropy reference layer. The challenge in this system is the efficiency of the FGL. In order to deliver a sufficient H_{ac} to the medium, a low flying height h_m of about 3nm, [44] large FGL thickness t_{FGL} of about 25nm [40] and a reasonable size FGL width W_{FGL} are required as the thickness of the FGL of $t_{FGL}/h_m > 1$ and $W_{FGL}/h_m > 1$. This is due to the fact that the largest value of $H_{ac} = 2\pi M_s$ which occurs at $h_m = 0$.

The principle of MAMR is similar to HAMR where an external energy is used to activate the grain reversal process. In theory MAMR has the potential to achieve an areal density of up to few TB/inch² but not above 10TB/inch². There is a potential to

combine BPM and MAMR to achieve up to 10TB/inch^2 but a similar density could be achieved using a combination of BPM and HAMR.

2.3.3 Heat Assisted Magnetic Recording

Heat assisted magnetic recording (HAMR) was originally demonstrated by Fujitsu in 2006, [45]. HAMR has the potential to extend the areal densities in disk media up to 10 TB/inch^2. It can be achieved by reducing the medium grain size down to $3-5$nm in a perpendicular FePt media with a narrow grain size distribution. The idea of HAMR is to increase the anisotropy constant to improve the thermal stability $K_U(T)$ of the media. Experimental work shows the temperature dependence of the anisotropy constant for bulk FePt and is shown in Figure 2.14, [46].
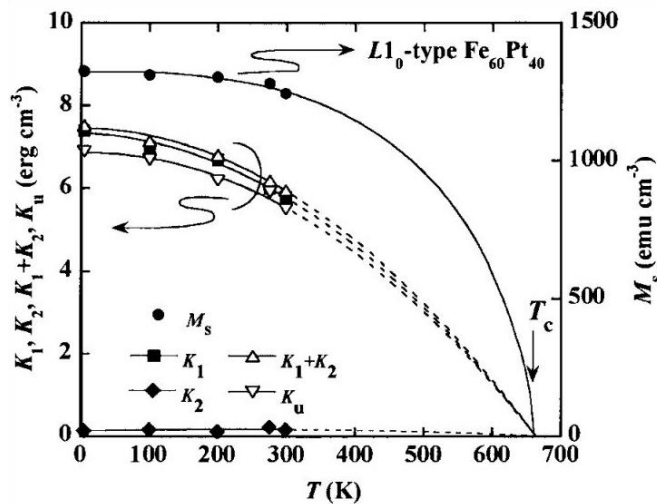
Figure 2.14 Variation of FePt properties with temperature, [46].

The principle of HAMR is to use thermal energy (usually a laser) to lower the coercivity of the recording layer. The magnetocrystalline anisotropy of a bulk L1$_0$ FePt material is 7 x 10^{7}ergs/cm^3 with a saturation magnetic moment of M_s = 1 x 10^{3}emu/cm^3 at room temperature, [46]. However as the temperature of the material approaches as its Curie temperature T_c, the magnetocrystalline anisotropy and hence the coercivity and magnetisation reduce to zero. In HAMR an external thermal energy is applied and the coercivity of the recording layer is then reduced to a value that is lower than the write field from the head. The medium is cooled down rapidly so that the anisotropy and coercivity are at their maximum values, [47]. Figure 2.15a shows a schematic of HAMR write process.

HAMR media requires the development of new components. For instance a rapid cooling system, a thermomagnetic write head system and a light delivery system, [48]. A schematic diagram of the HAMR system is shown in Figure 2.15b. A free-space laser beam is mounted in front of the write head and synchronised with a waveguide. The geometry of the waveguide has to form a planar solid immersion mirror and is used to focus the beam onto a desired position on the medium, [49]. To achieve high areal data density the medium must be within few nanometers. Therefore a near field transducer is used to overcome the diffraction limit. The write head is one of the main challenges of HAMR. The head is required to integrate with the light and write field delivery system and be able to fly along the medium at less than 10nm head to medium spacing. The write head needs to generate a head field of 5 – 10kOe at the position of the heat spot in order to reverse the magnetisation of the recording layer, [7]. One of the possible configurations for HAMR is called "optical spot defines the track". This system requires a narrow spot but a broad write field. The geometry of the write pole is able to generate a sufficient magnetic field to reverse the media rapidly. It is assumed that recording layer materials with high coercivity at room temperature are used. Therefore the write head field is not able to demagnetise the neighbouring region. The signal is then read back using a TMR head.
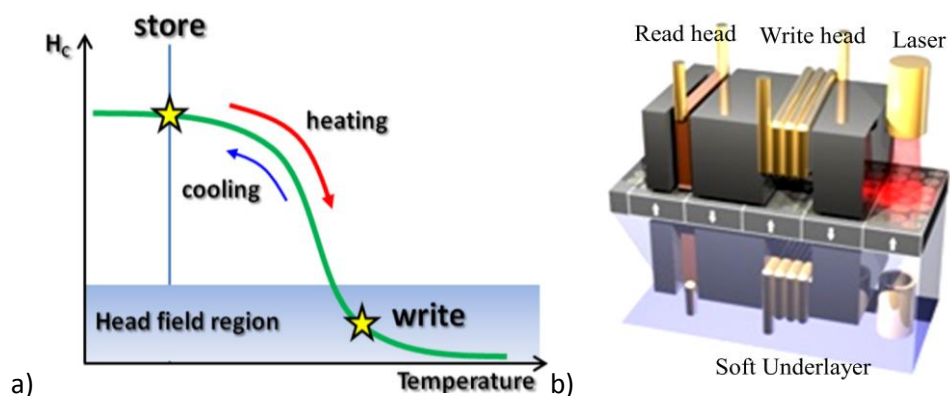
Figure 2.15 Schematic diagram of a) Coercivity variation with temperature in HAMR write process, [50]. b) HAMR system.

The schematic diagram of a HAMR is shown in Figure 2.15b. One of the unique features of HAMR is a heat sink which must be provided in order to mitigate the thermal stability of the media as shown in Figure 2.16. The recording materials for

HAMR media require a large temperature dependent anisotropy leading to a lower switching field, high magnetic anisotropy at the storage temperature and a small grain size. There were some studies of possible thin films alloy materials which are suitable for HAMR media. Such as NdFeB, $SmCo_5$, FePt which have a measured uniaxial anisotropy of up to 46×10^7, 200×10^7, 70×10^7 and 1×10^7ergs/cc, respectively, [50].

$L1_0$ type FePt has been extensively studied due to its high magnetocrystalline anisotropy and which remains thermally stable at 300K with a small grain size of 3nm, [51]. Fcc FePt does not exhibit high anisotropy therefore it is essential to achieve the $L1_0$ phase and annealing temperatures of higher than 600°C(873K) are required, [18].

There were several approaches to produce $L1_0$ FePt with small grain size. Chemical synthesis methods have been used to produce FePt particles with grain size of 4nm, the particles were then annealed to obtain $L1_0$ phase but this resulted in much larger grain sizes, [18]. An alternative approach was nanocluster beam deposition, [52]. This method requires annealing the FePt particles during deposition to achieve the $L1_0$ phase. However it resulted other challenges such as easy axis orientation and a large surface roughness, [53]. Another potential method was to use a synthetic nucleation layer method to achieve a grain size down to sub 6nm, [54]. A single underlayer was used to tackle the grain size reduction. The lowest grain size for an FePt thin film was reported by Shen et al. [55] of about 6.6nm using a RuAl underlayer, [55]. There were a few other studies of doping FePt with Cu, Ag and C in order to reduce the grain size and the required annealing temperature, [56]. None of the doping materials were capable of producing grain sizes smaller than 5nm, [18].
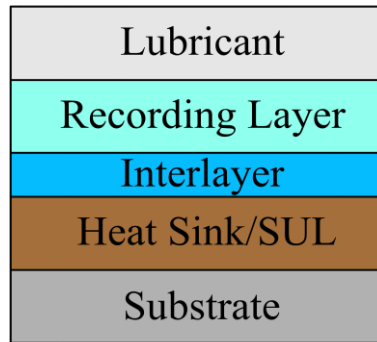
Figure 2.16 Schematic diagram of a typical layer structure for HAMR.

HAMR media is limited due to the external thermal energy generated in the media during the writing process. As the temperature of the recording material is close to its Curie temperature, the switching field approaches infinity because the anisotropy field H_K increases ($H_c \propto H_K = 2K_U/M_s$). This results in a large switching field distribution. 1.5TB/inch^2 HAMR was demonstrated by Nikkei Technology in 2012, [57]. New developments and ideas are required to extend the areal density of HAMR media to 5TB/inch^2. There is a potential to employ HAMR with BPM in order to extend the areal density up to 100TB/inch^2, [58]. But the first step is to make feasible HAMR media which is one of the main objectives of this study.

Chapter 3

Physics of Magnetic Recording Media

This chapter focuses on the basic theory of magnetism which is used in magnetic recording media. Fundamental underpinning science associated with magnetic recording such as the Stoner-Wohlfarth theory and the demagnetising field are discussed. The basis of this study was to utilise exchange bias to achieve Heat Assisted Magnetic Recording (HAMR). Therefore a brief review of exchange bias is included. This study was focused on The York Model of Exchange Bias because it is applicable to granular thin film samples, [59].

3.1 Single Domain Particles

A magnetic domain refers to a region of a material where the direction of the magnetic moments is aligned in same direction. The origin of the formation of the domains is to minimise the magnetostatic energy. Assume a large single crystal such as Co with uniaxial anisotropy which forms a single domain. If the domain is magnetised along the easy axis then free poles form at the ends. The magnetostatic energy is

$$E_{ms} = \frac{1}{8\pi} \int H_D{}^2 dV \qquad (3\text{-}1)$$

where H_D is the demagnetising field which depends on the orientation of the domain and its shape, V is the volume. It indicates that the magnetostatic energy depends on the demagnetising field and the c-axis orientation of the domain. Since $H_D = 4\pi M_S$ for a long cylinder differentiating Equation (3-1) for a minimum gives

$$E_{ms} = \frac{1}{2} N_D M_S{}^2 \qquad (3\text{-}2)$$

where N_D is the demagnetising factor and M_S is the saturation magnetisation. The saturation magnetisation is dependent on the material and the demagnetising factor is dependent on the displacement between north and south poles. If the poles are closer to each other the magnetostatic energy increases as H_D is increased.

The magnetostatic energy can be reduced if the crystal splits into two domains magnetised in opposite direction. If it splits into four domains the magnetostaic energy is further reduced. These domains are divided by a domain wall which is the boundary of a domain. However the domains cannot be split to an unlimited degree because of the energy associated with the domain wall. Hence the division will eventually stop at the equilibrium energy.

For a single cubic crystal in a perpendicular orientation where N_D is the demagnetising factor and for a sphere is equal to $4\pi/3$ the magnetostatic energy can be expressed as

$$E_{ms} = \frac{2}{3}\pi l M_S{}^2 \tag{3-3}$$

where l is the length of the domain. The domain wall energy per unit area is

$$E_{wall} = \sigma_w \frac{D_w}{l} \tag{3-4}$$

where σ_w is the domain wall energy per unit area of the wall and D_w is the wall width. The minimum size of the domain can be calculated by differentiating the sum of the E_{ms} and E_{wall}. The equation that relate D and l is

$$D = \sqrt{\frac{l\sigma_w}{0.85M_S{}^2}} \tag{3-5}$$

For a typical ferromagnet the critical size for single domain behaviour lies between 30nm and 50nm.

3.2 Stoner-Wohlfarth Theory

For a magnetic single domain with less than 20nm the only possible reversal mechanism is moment rotation and the theory that explains this process is known as Stoner-Wohlfarth theory, [13]. Figure 3.1 shows a schematic of a single domain ellipsoid with a field H applied at an angle α_h away from the easy axis.
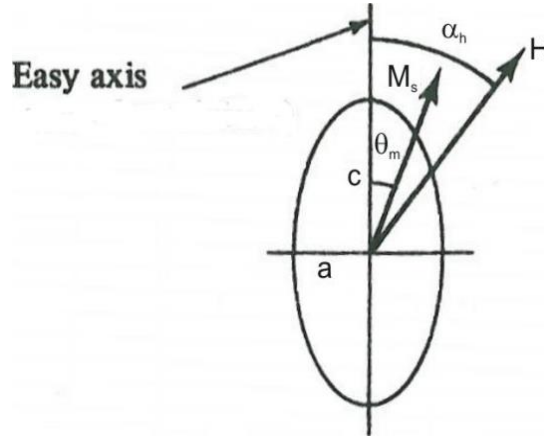
Figure 3.1 Definition of angles in the Stoner-Wohlfarth model. [60]

There are two energy terms associated with the particle which are the anisotropy energy E_a and the Zeeman energy E_Z that contribute to the total energy. The anisotropy energy of a single domain particle is given by

$$E_a = K_u \, sin^2 \, \theta_m \tag{3-6}$$

where K_u is the uniaxial anisotropy and θ_m is the angle between the c-axis and the magnetisation direction. The Zeeman energy is given by

$$E_Z = -HM_S \, cos(\alpha_h - \theta_m) \tag{3-7}$$

where H is the applied field, M_S is the saturation magnetisation and α_h is the angle between the c-axis and the applied field. The total energy is the sum of the anisotropy energy and the Zeeman energy expressed as

$$E_T = K_u \, sin^2 \, \theta_m - HM_S \, cos(\alpha_h - \theta_m) \tag{3-8}$$

In order to achieve an equilibrium position of the moment direction the total energy is differentiated with respect to the angle θ_m

$$2K_u \sin\theta_m \cos\theta_m - HM_S \sin(\alpha_h - \theta_m) = 0 \qquad (3\text{-}9)$$

Since the magnetisation component is $M = M_S \cos(\alpha_h - \theta_m)$ and assuming the field is normal to the easy axis α_h = 90° and $m = M/M_S$ Equation (3-9) becomes

$$m = \frac{HM_S}{2K_u} \qquad (3\text{-}10)$$

Equation (3-10) shows that if the field is applied along the normal of the easy axis direction the magnetisation exhibits a linear variation with field. At the saturation position $H = H_K = 2K_u/M_S$. If h is the normalised field ($h = H/H_K$) hence Equation (3-9) can be written as

$$m = \cos(\alpha_h - \theta_m) \qquad (3\text{-}11)$$

Equation (3-11) shows the variation of the normalised magnetisation as a function of applied field at a certain angle of α_h which can be calculated from the second derivative of Equation (3-8). The full mathematic derivation can be found in Cullity and Graham, [60]. Figure 3.2 shows hysteresis loops for a single domain particle associated with uniaxial anisotropy. α_h represents the angle between the easy axis and the field.
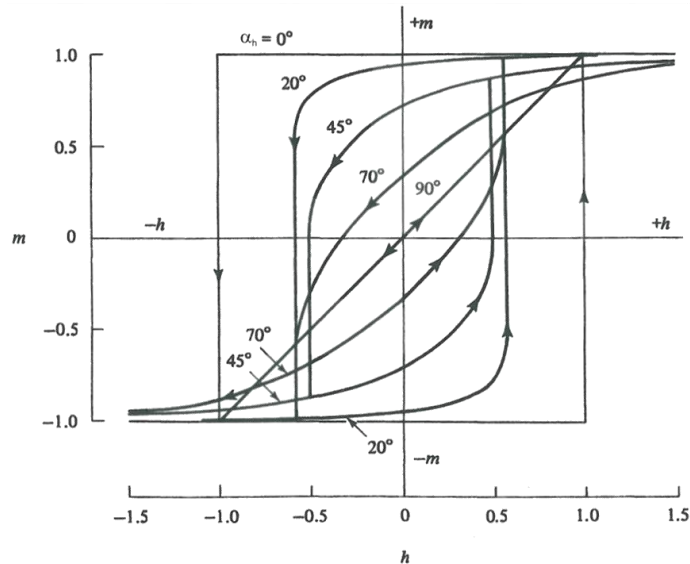
Figure 3.2 Hysteresis loop measurements for different value of α_h, [13].

Figure 3.2 shows that a small deviation of the easy axis direction from that of the applied field leads to a significant reduction of switching field. In the case of a deviation of 10° this leads to a reduction of the switching field of 30%.

In perpendicular recording media (PMR) the deviation of the easy axis direction of the grains largely determines the thermal stability and will be discussed in Section 3.8. The energy required for a single grain reversal is

$$\Delta E = K_U V_m \left(1 - \frac{H}{H_K} \right)^2 \qquad (3\text{-}12)$$

where ΔE is the energy barrier, K_U is the anisotropy constant, V_m is the volume of the grain, H the applied field and H_K the anisotropy field. The H/H_K term does not have a significant value at remanence at H = 0 and is usually assumed to be 0. The other factor that affects the energy barrier ie the anisotropy constant is determined by the crystallinity of the material. The switching field distribution in perpendicular and advance recording media is given by

$$H_S = \frac{\alpha_a K_U}{M_S} \qquad (3\text{-}13)$$

where α_a is the alignment factor of the grain. Chureemart et al. studied the orientation distribution in advanced recording media via coercivity measurements as a function of angle and found that the standard deviation σ was typically 6°. However this gives a 3σ value of 18°, [61].

The standard deviation of the grain size distribution and that of the anisotropy constant are the factors which affect the switching field distribution in recording media. In advanced recording media the standard deviation of the grain size distribution is lower than 0.2, [61]. The media is now deposited using a heated substrates and results in fully crystalline grains in the CoCrPt-SiO$_2$ layer. Therefore the distribution of the anisotropy constants is very small. Hence the key factor that affects the switching field is the orientation of the grains as shown in Equation (3-13).

3.3 Magnetocrystalline Anisotropy

Magnetocrystalline anisotropy also known as crystal anisotropy is an intrinsic property of a magnetic material. The effect is manifested as the applied field required to saturate the crystal being dependent on the direction of the field. The origin of magnetocrystalline anisotropy is due to spin orbit coupling in the crystal lattice. When atoms are bonded together the orbital angular moment of the electrons is fixed and the spin angular momentum of the electrons is coupled via the spin orbit interaction. In order to re-align the spin of the electrons to a desired direction an external energy is required to overcome the spin orbit coupling. This energy is the magnetocrystalline anisotropy energy E_K. This can be expressed in terms of a series expansion of the direction consines denoted α_1, α_2, α_3 of M_s with respect to the crystal axes

$$E_K/V = K_0 + K_1(\alpha_1^2\alpha_2^2 + \alpha_2^2\alpha_3^2 + \alpha_3^2\alpha_1^2) + K_2(\alpha_1^2\alpha_2^2\alpha_3^2) + \cdots \qquad (3\text{-}14)$$

where V is the volume, K_0, K_1 and K_2, ... are energy densities expressed as constants for a specific material at a given temperature and are expressed in ergs/cm^3 (cgs). It is important to note that the first and third terms are usually neglected. This is because K_0 is independent of angle and K_2 is small. The only significant term is K_1 which gives the energy per unit volume required to rotate the saturation magnetisation from one direction to another.
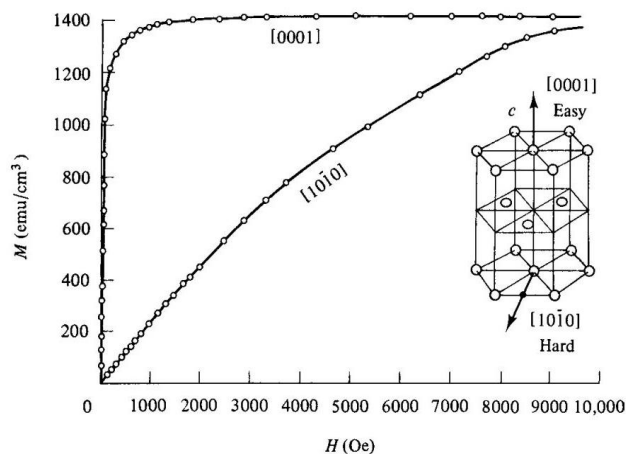
Figure 3.3 Magnetisation curves for a single crystal of Co, [60].

For a hexagonal close packed structure such as Co and Co alloys, the easy axis is along the c-axis and all directions in the basal plane are found to be equally hard as shown in Figure 3.3. Therefore the anisotropy is only dependent on a single angle θ_U i.e. uniaxial. Hence the magnetocrystalline anisotropy energy is now given by

$$E_K/V = K_0 + K_1 \sin^2 \theta_U + K_2 \sin^4 \theta_U + \cdots \qquad (3\text{-}15)$$

where θ_U is the angle between the easy axis direction and the magnetisation. E_K is still dependent on the K_1 term and the third term is small due to $\sin^4 \theta_U$ and is neglected.
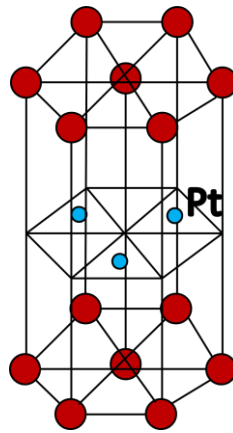
Figure 3.4 Pt atom locations in a CoCrPt alloy.

In perpendicular recording media the recording layer is based on a CoCrPt alloy. A small amount of less than 25 at % of Pt is used to increase the magnetocrystlline anisotropy, [18]. This is because the Pt atoms are located in the middle of the unit cell between two hexagonal rings of Co as shown in Figure 3.4. This leads to a stress along the c-axis of the crystal and hence increases the value of K_1. In perpendicular recording media the CoCrPt alloy used has a typical value of K_U above 8 x 10^6 ergs/cc, [62]. The grain size of the media is about 6nm. In Section 3.8 we will discuss that the transition width is dependent on the grain size. Since the signal to noise ratio (SNR) is highly dependent on the transition width therefore a medium with small grain size results a better SNR. In HAMR the proposed recording media is L1$_0$ phase FePt structure. For an areal density of 4Tbits/inch^2 hard drive the value of its K_U at room temperature is 5 x 10^7ergs/cm^3, [4].

3.4 Interfacial Anisotropy

Co/Pt and Co/Pd multilayers are examples of systems exhibiting perpendicular anisotropy created by interfacial anisotropy. The Pt or Pd layer is used to separate the Co layer because if there are more than 2 atoms of Co the anisotropy will collapse. The typical thickness of the Co layer is limited to a range of about 0.3 to 0.7nm, [63] at this thickness the Co is not thick enough to crystallise therefore this is an interfacial anisotropy instead of a magnetocrystalline effect. An optimised Co/Pt multilayer structure in terms of coercivity is shown in Figure 3.5.

| Pt (1.6 nm) |
| Co (0.6 nm) |
| Pt (1.6 nm) |
| $\mathbf{K}_F$ Co (0.6 nm) |
| Pt (1.6 nm) |
| Co (0.6 nm) |
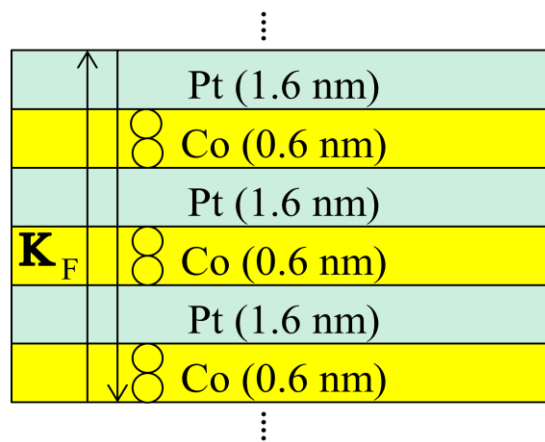
Figure 3.5 Schmatic diagram of the Co/Pt multilayer system with typical stack thicknesses.

Co/Pd and Co/Pt multilayer systems are proposed for future nano-technologies such as spin-torque transfer (STT) devices [64] [65] [66] and bit patterned media (BPM), [67] [68]. Barton et al. showed that the interfacial anisotropy of Co/Pd multilayers is controlled by the interface roughness, [69]. However the interfacial roughness is dependent on the grain size as illustrated in Figure 3.6. For a thin film sample the atomic growth is not evenly distributed across the surface. Assuming the layer thickness is 0.6nm, which is approximately 2 atoms thick, there are areas which have only 1 or more than 2 atoms. In Figure 3.6 it can be seen that the blue grains are bigger than the red grains. Hence the surface roughness of the red grains is less than that of the blue grains. Hence the grain size is proportional to the surface roughness Δt. In a study by Vopsaroiu et al., [70] the grain size was shown to be proportional to the deposition rate using the HiTUS deposition system. Hence

the surface roughness of a multilayer sample can be controlled. In order to achieve low surface roughness a low deposition rate is required.
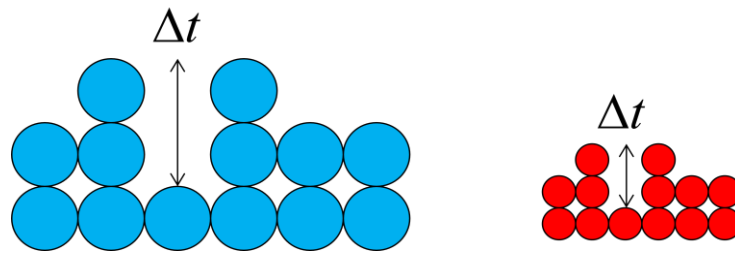
Figure 3.6 Schmatic diagram of the surface roughness affected by the grain size.

3.5 Demagnetising Field in Recording Media

The origin of the demagnetising field is due to Gauss law which specifies that there are no magnetic monopoles. For a bar magnet the field diverges into a north pole and a south. If a magnet is magnetised from left to right (say) the demagnetising field H_D will acts against the direction of the magnetisation (right to left).
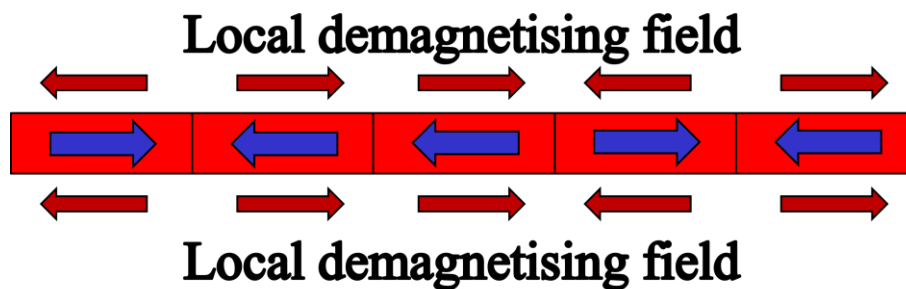
Figure 3.7 Local and global demagnetising field in longitudinal recording media.

In longitudinal recording the magnetisation orientation lies in the plane, therefore the global demagnetising field is zero. There are two different demagnetising field associates with the system which are illustrated in Figure 3.7. The first is the demagnetising field from the bit which tries to demagnetise itself. The second demagnetising field is generated between the bits. The demagnetising field generated from a single bit is fixed but the demagnetising field generated from bit to bit is dependent on the data density. Hence the areal density in longitudinal recording is limited by the demagnetising field.

Perpendicular recording was invented in order to reduce the demagnetising field so that a higher areal density can be achieved. The demagnetising field in a perpendicular recording media is illustrated in Figure 3.8. Due to the orientation of the grains the global demagnetising field is

$$H_{GD} = -4\pi M \qquad (3\text{-}16)$$

In perpendicular recording the demagnetising field generated from a bit is known as local demagnetising field as shown in Figure 3.8. This field is reduced by neighbouring bits with the opposite magnetisation direction. As the bit density increases the local demagnetising field is reduced.
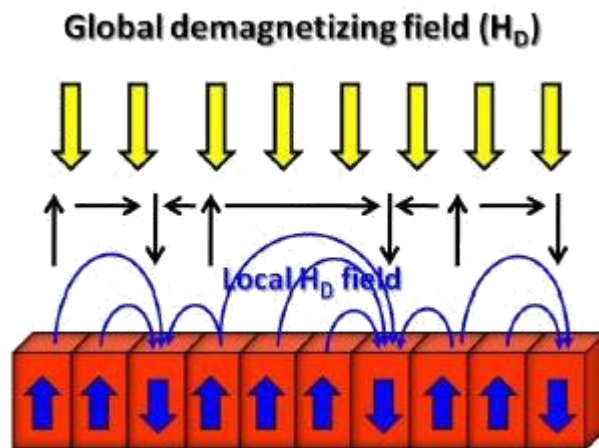
Figure 3.8 Local and global demagnetising field in perpendicular recording media.

In order to achieve high bit density a small grain size is required and will be discussed in Section 3.8. The energy required to reverse a grain is given by

$$\Delta E = K_U V_m \left(1 - \frac{H}{H_K}\right)^2 \qquad (3\text{-}17)$$

Hence as the volume of the grains decreases the magnetocrystalline anisotropy has to be increased to maintain thermal stability. CoCrPt alloy is the selected material used as the storage layer in PRM. From the Neel-Arrhenius law to give stability for 10 years, the grain size in such media is ~6.3nm.

3.6 Exchange Interactions

Direct Exchange

In disk media there are direct and indirect exchange interactions. The origin of the direct exchange interaction is due to the quantum mechanical exchange force described by Heisenberg in 1928. If there are two hydrogen atoms close to each other with the angular spin moment S_i and S_j, the wave functions of these atoms can overlap and minimise the energy. This can be achieved via orientation the spins in opposite directions. The energy associated with this interaction is

$$E_{ex} = -2J_{ex}\underline{S_i}\underline{S_j} \tag{3-18}$$

where J_{ex} is the exchange integral which determines whether the atomic spins should align parallel or anti-parallel. The sign of J_{ex} is dependent on the ratio of r_A/r_{3d} where r_A is the radius of an atom and r_{3d} is the radius of its $3d$ shell of electrons. Figure 3.9 is known as the Bethe-Slater curve which shows the exchange integral for different elements with different ratios r_A/r_{3d}. If the value of J_{ex} is positive then the exchange energy in Equation (3-18) will be a minimum if the spins are aligned parallel. However if J_{ex} is negative then the lowest energy state is achieved by anti-parallel alignment as shown in Figure 3.9.
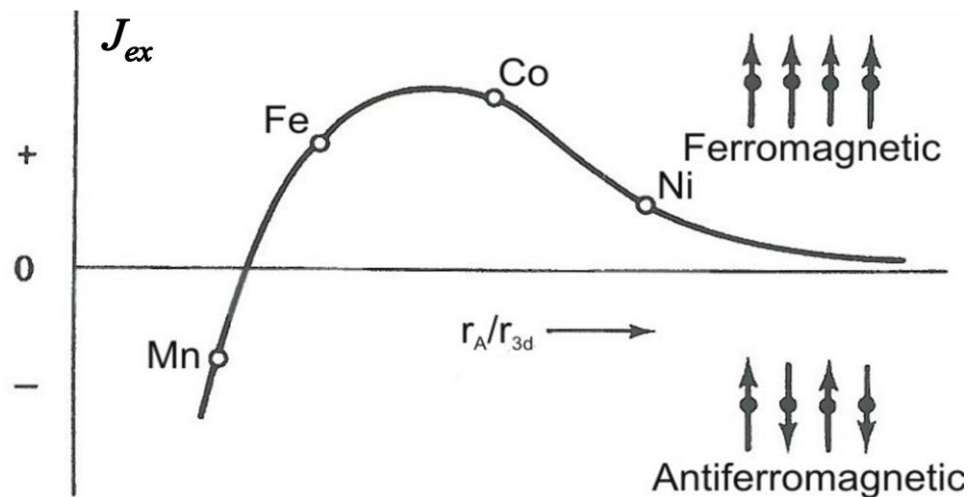
Figure 3.9 Bethe-Slater curve showing J_{ex} against interatomic spacing, [60].

Mn has a negative value of J_{ex} leading to the anti-parallel alignment and antiferromagnetism. As the atomic radius decreases the exchange integral becomes positive and the spins are now held in a parallel alignment by strong exchange forces hence exhibiting ferromagnetism.

Indirect Exchange

The indirect exchange is also known as the Ruderman-Kittel-Kasuya-Yosida (RKKY) interaction and was proposed by Ruderman and Kittel (1954), [71] Kasuya (1956) [72] and Yoshida (1957) [73]. The origin of indirect exchange is the local magnetic moment polarising the conduction electrons which align nearby moments even across grain boundaries. Hence it is a long range coupling. The exchange integral J_{ex} oscillates between positive and negative values as the separation between the atoms varies.
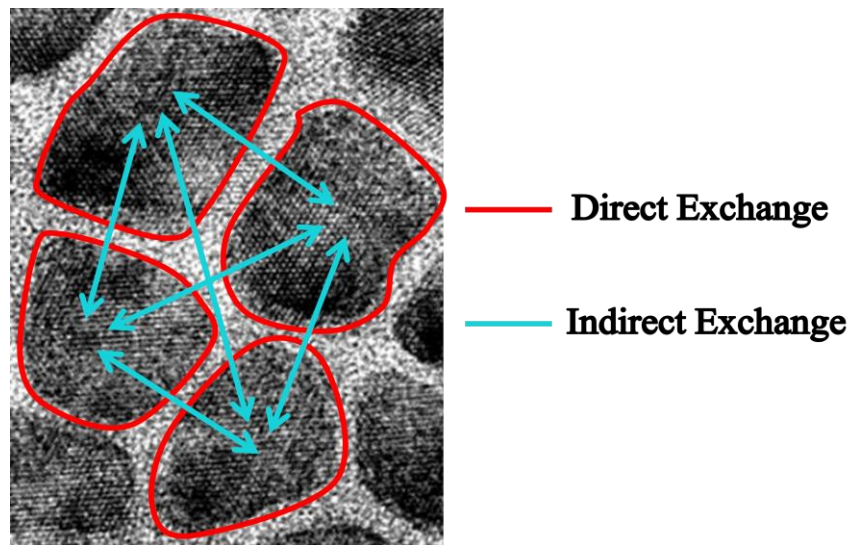
Figure 3.10 High resolution TEM image of advanced recording media labelled with direct exchange and indirect exchange interaction between grains, [61].

In advance recording media the grain itself exhibits direct exchange interaction and the exchange coupling between grains is due to RKKY coupling as illustrated in Figure 3.10. In Section 3.6 a detail discussion is presented that shows it is possible to reduce the transition width by reducing the grain size. However if the grains are coupled this results a large effective grain size in the media. Hence an SiO_2 insulator is used to eliminate the RKKY coupling.

3.7 The York Model of Exchange Bias

In order to achieve HAMR using exchange bias an antiferromagnetic (AF) layer is required in the thin film samples. The measurements in this study were based on The York Model of Exchange Bias which was described in detail by O'Grady et al. in 2010, [59]. All the experimental works presented in The York Model were on polycrystalline thin film structures. This model is partially based on the work of Fulcomer and Charap where the AF layer is made of independent single domain AF grains, [74] [75]. Therefore the energy required to reverse an AF grain is

$$\Delta E = K_{AF}V(1 - \frac{H^*}{H_K^*})^2 \qquad (3\text{-}19)$$

where K_{AF} is the anisotropy of the AF, H^* is the exchange field from the ferromagnetic (F) layer and H_K^* is a pseudo anisotropy field. The relaxation time τ of an AF grain is then given by the Néel-Arrhenius law

$$\tau^{-1} = f_0 e^{-\Delta E/k_B T} \qquad (3\text{-}20)$$

where ΔE is energy barrier, k_B is the Boltzmann's constant, T is temperature and f_0 is an attempt frequency with a typically value of 10^{12} s^{-1} as shown by Vallejo Fernandez et al., [76]. This model is capable of predicting the relationship between exchange bias, grain volume, time dependence measurements and interfacial effects, [59].

The York Model describes the exchange bias in polycrystalline thin film with grain sizes in the range between 5 - 15nm. It has also been adapted to describe the behaviour of epitaxial single crystal films and large grain polycrystalline films based on strong domain wall pinning, [59]. The York Model had a significant impact in hard disk drive manufacturers and it was applied to characterise exchange bias materials used in read heads, and was used to redesign the AF layers in read heads by Seagate Technology, [77] .

Grain Volume & Thickness Dependence

Exchange bias occurs when an AF layer is in intimate contact with a F layer and is cooled through its Néel temperature. If a magnetic field is applied to reverse the F layer the spins in the AF layer pin the F layer at the interface leading to a shift of the hysteresis loop. The displacement between the origin and the centre of the loop is known as exchange bias H_{ex} as shown in Figure 3.11.
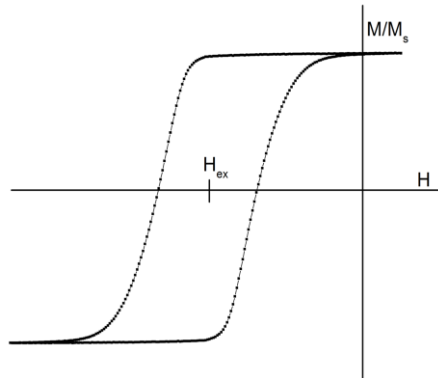
Figure 3.11 Hysteresis loop with the position of $\boldsymbol{H_{ex}}$.

The AF material used in this study and described in The York Model is IrMn. There are two possible phases of IrMn which are the ordered $L1_2$-IrMn$_3$ and the disordered γ-IrMn$_3$ with Néel temperatures of T_N = 1000K and T_N = 730K, respectively, [78]. However heating the thin film to such a high temperature will causes significant damage to the sample. Therefore a thermal activation process is used to set the AF layer as shown in Figure 3.12.
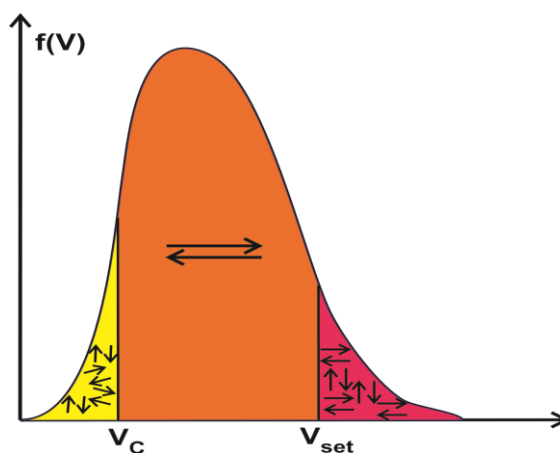
Figure 3.12 Schematic diagram of the AF grain volume distribution, [59].

After the sample is set at a setting temperature T_{set} over a time t_{set} it is cooled back to a measurement temperature T_{ms}. Some of the AF grains are not thermally stable and are labelled in yellow in Figure 3.12. The yellow region when $V < V_c$ is where the AF grains are too small and are not thermally stable (labelled in red). This is analogous to superparamagnetic particles, [59]. For the grains with $V > V_{set}$ the grain volume is too large and cannot be set by the exchange field from the F layer at the temperature T_{set}. Hence the AF grains that contribute to the exchange bias are those with $V_{set} > V > V_c$. H_{ex} is then given by [59]

$$H_{ex}(T_{ms}) \propto \int_{V_{c(T_{ms})}}^{V_{set}(T_{set})} f(V)dV \qquad (3\text{-}21)$$

In this work all measurements were undertaken at measurement temperature T_{NA} at which with no thermal activation occurs for the smallest grains.

The actual values of V_c and V_{set} can be calculated by combining equations (3-19) and (3-20)

$$V_c = \frac{ln(t_{ms}f_0)k_B T_{ms}}{K_{AF}T_{ms}} \qquad (3\text{-}22)$$

where t_{ms} is measurement time at the measurement temperature T_{NA} and K_{AF} is the anisotropy constant of the AF and it is temperature dependent. Similarly the value of V_{set} can be calculated from

$$V_{set} = \frac{ln(t_{set}f_0)k_B T_{set}}{K_{AF}T_{set}} \qquad (3\text{-}23)$$

where t_{set} is the setting time at the setting temperature T_{set} before the field cooling process. Hence the exchange bias is proportional to the number of grains with the size between V_c and V_{set} which can be express as

$$H_{ex} \propto \int_{V_c}^{V_{set}} f(V)dV \qquad (3\text{-}24)$$
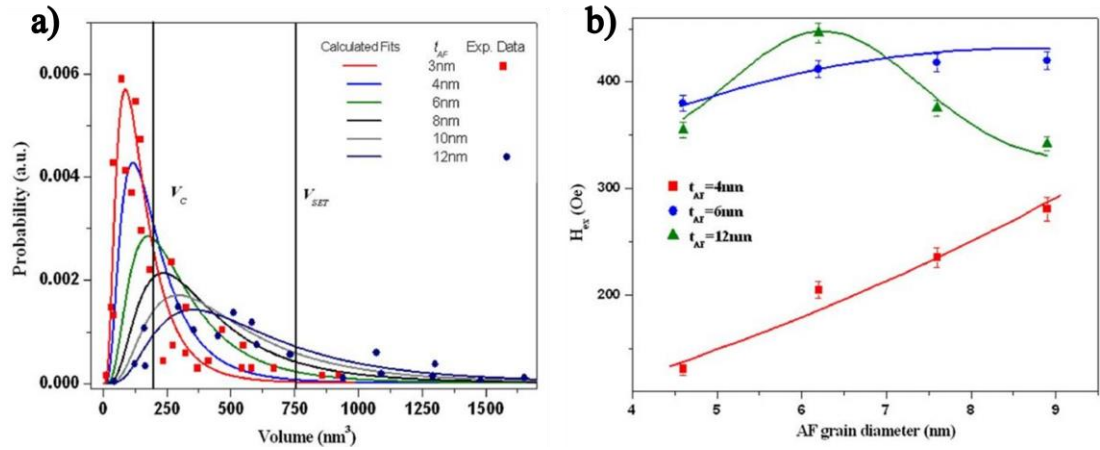
Figure 3.13a) Grain volume distributions for the samples with different AF thickness. b) Exchange bias as a function of AF grain diameter, [79].

Vallejo-Fernandez et al. [79] calculated the exchange bias as a function of the AF grain diameter. The AF grain volume distribution is shown in Figure 3.13a. This was achieved measuring more than 500 grains manually using an equivalent circle method. In Figure 3.13b the lines correspond to the theoretical values which were calculated using Equation (3-24). The parameters used in this calculation were T_{ms} =293K, t_{ms} =1800s, T_{set} =498K and t_{set} =5400s. The points correspond to the experimental data. The experimental data shows an excellent fit and it was fitted with a scaling factor C^* which is the interfacial coupling constant. The determination of the value of K_{AF} is described later in this section.

Figure 3.14 shows the variation of exchange bias with the thickness of the AF layer. The samples were set using a positive saturation field of 1kOe at 498K for 90 minutes. The hysteresis loops were then measured at room temperature where there was no thermal activation. The data points were fitted with a theoretical calculation using Equation (3-24). The figure shows H_{ex} increases rapidly as the thickness of AF layer increases. The peak was found using a thickness of 8nm of AF layer and H_{ex} decreases using thicker AF layers. This result can be explained using Figure 3.13a. It can be seen that the area under the 8nm curves between V_c and V_{set} is the largest. Hence according to Equation (3-24) the largest exchange bias was measured using 8nm thick AF layer.
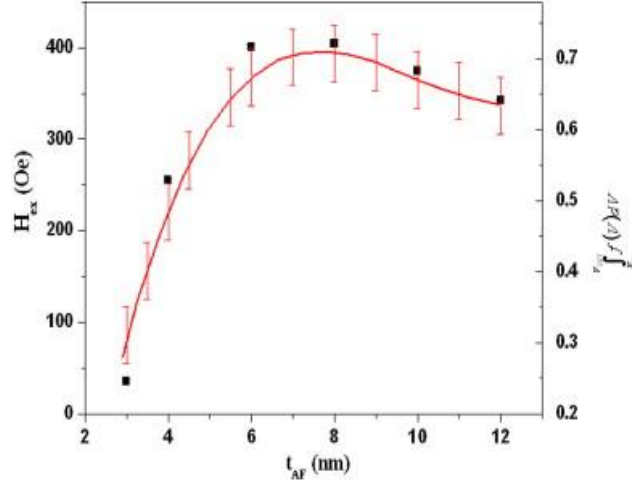
Figure 3.14 H_{ex} as a function of AF thickness and theoretical fit to equation (3-24), [79].

Measurement of AF Anisotropy

A measurement process to determine the anisotropy of an AF was developed by Vallejo Fernandez et al, [80]. The measurement involves a thermal activation process at a temperature T_{Act}. At the beginning the sample is heated to a setting temperature T_{set} in an applied field for a time t_{set}. During the setting time the F layer is saturated. The sample is then field cooled to a temperature T_{NA} where there is no thermal activation of the AF grains. The sample is then heated to thermal activation temperature T_{Act} in a reverse applied field for a time t_{Act}. At this point a fraction of AF grains is thermally active in the opposite sense to the original setting process. As the activation temperature increases the fraction of the reversed AF grains will increase. Hence the exchange bias that is measured is given by

$$H_{ex} \propto \int_{V_{Act}}^{V_{set}} f(V)dV - \int_{0}^{V_{Act}} f(T_B)dT_B \qquad (3\text{-}25)$$

where V_{Act} is the volume of the largest grains which can be thermally activated at T_{Act}. The value of V_{Act} is given by

$$V_{ACT} = \frac{ln(t_{Act}f_0)k_B T_{Act}}{K_{AF} T_{Act}} \qquad (3\text{-}26)$$

The value of exchange bias is plotted against T_{Act} to give what is known as blocking temperature curve as shown in Figure 3.15.

54
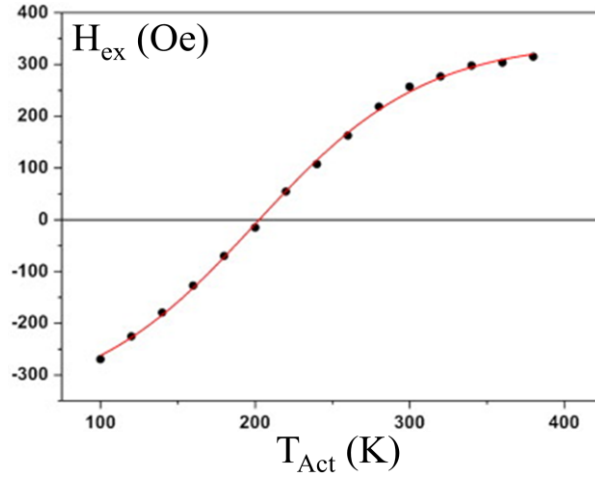
Figure 3.15 Typical blocking curve used to measure the blocking temperature, [59].

In Figure 3.15 the sample was set using a positive field. The curve is not flat at the beginning which indicates that the smaller AF grains were not thermally stable at T_{NA}. At the point where H_{ex} is equal to zero there are equal fractions of the AF grain volumes orientated in opposite directions. The median blocking temperature $< T_B >$ is defined as the activation temperature at which H_{ex} goes to zero. The anisotropy of the AF can then be calculated

$$K_{AF} = \frac{ln(t_{SET}f_0)k_B<T_B>}{V_m}$$ (3-27)

where V_m is the median grain volume. The blocking temperature shown in Figure 3.15 can be differentiated with respect to T_{Act} giving a Gaussian like distribution of $f(T_B)$.

3.8 Limitations of Recording Media

The most significant way to achieve high areal density for hard disk drive media is to reduce the transition width. The transition width parameter a_0 represents the magnetic transition distance between opposite moments of either up or down direction in the medium. In the case of perpendicular recording media the approximation of the transition width a_w is [25]

$$a_w = -\frac{\delta_{med}}{4} + \frac{(d_s + \frac{\delta_{med}}{2})\,[SFD + M_r/H_{cr}]}{\pi Q_\perp}$$

$$+ \left[\left(\frac{(d_s + \frac{\delta_{med}}{2})\,(SFD + M_r/H_{cr})}{\pi Q_\perp} - \frac{\delta_{med}}{4} \right)^2 + \frac{(d_s + \frac{\delta_{med}}{2}) \cdot SFD \cdot \delta_{med}}{\pi Q_\perp} \right]^{\frac{1}{2}}$$

(3-28)

where a_w is Williams-Comstock transition width [81], δ_{med} is the thickness of medium and d_s is the spacing between the head and the medium. The switching field distribution $SFD = (1 - S^*)$ is defined as the width of the SFD, [82] where S^* is illustrated in Figure 3.16, M_r is the remanent magnetisation, H_{cr} the remanent coercivity and $Q_\perp$ is the head field gradient defined in Equation (3-29). Equation (3-28) has been modified based on Williams-Comstock transition width for longitudinal recording. The head field gradient used in equation (3-28) is now in perpendicular direction.

There is a first approximation of the transition width a_0 which is equal to $M_r \delta_{med}/H_c$.
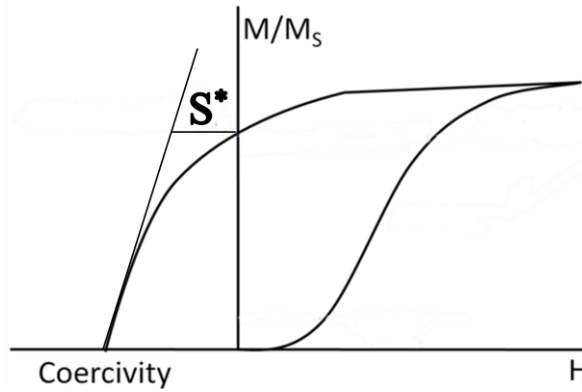
Figure 3.16 Schematic diagram of S^* in a hysteresis loop.

Equation (3-28) indicates that a_w is dominated by the third term where the SFD dependence is weak. It also indicates that the writing process is not demagnetisation free even if the coercivity is greater than the saturation magnetisation. The head field gradient parameter $Q_\perp$ is given by

$$Q_\perp = -\frac{(d_s + \frac{\delta_{med}}{2})}{H_{cr}} \cdot \frac{dH_z}{dx}$$

(3-29)

56

where H_z is the field in the z-direction. Therefore the value of a_w can be reduced by decreasing the parameters M_r and δ_{med} or increasing the value of H_{cr}. An alternative way to approximate the transition width is to express it in it terms of the average grain diameter D_a [83]

$$a_0 \cong \sqrt{0.35a_w^2 + \left(\frac{D_a}{2}\right)^2} \qquad (3\text{-}30)$$

The transition is then $\propto D_a$ and a high areal density can be achieved by reducing the grain size. Figure 3.17 shows a schematic diagram of a perpendicular recording media and grain structure. The recording medium is magnetised in either the up or down direction using a single pole head. The transition width includes the grain boundary width labelled as the yellow line in Figure 3.17. The red grains in the top TEM image are magnetised up and the blue grains down. The transition width can be seen to depend on the grain size for geometrical reasons. Also exchange interactions will result in an increase in the effective grain size and hence a_w
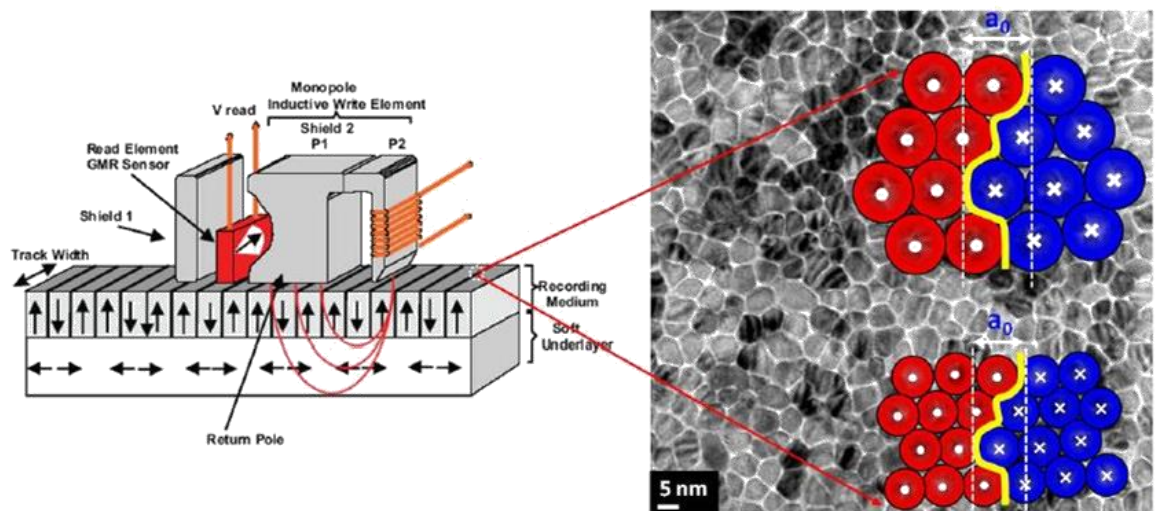
Figure 3.17 Schematic diagram of perpendicular recording media and the transition width dependence on grain size, [84].

There are three important factors which limit the storage density known as the trilemma of magnetic recording shown in Figure 3.18, [2].
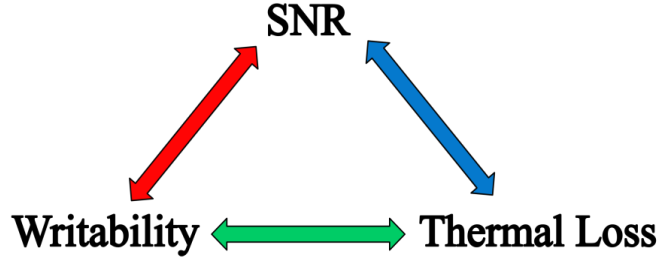
Figure 3.18 The magnetic recording trilemma.

The SNR determines the performance of the disk and an approximation for the SNR is given by [2]

$$SNR \propto \frac{B_L}{D^2} \qquad (3\text{-}31)$$

where B_L is the bit length and D is the grain diameter This equation indicates that the SNR is inversely proportional to the grain diameter. The equation is primarily dominated by the grain size as all of the terms in the denominator are dependent on the grain size. Hence reducing the diameter of the grain increases the SNR.

For thermal stability high anisotropy of the grains is required. The energy required to reverse a grain can be expressed as

$$\Delta E = K_U V_m \left(1 - \frac{H}{H_K}\right)^2 \qquad (3\text{-}32)$$

where ΔE is the energy barrier, K_U is the anisotropy constant, V_m is the volume of the grain, H is the applied field and H_K is the anisotropy field. The other critical factor is the switching field distribution which is define as

$$H_S = \frac{\alpha_a K_U}{M_S} \qquad (3\text{-}33)$$

A detail discussion about Equation (3-32) and (3-33) is given in Section 3.2.

For an ideal medium the anisotropy field H_K should be maximised. This can be achieved by increasing the total anisotropy K_U or reducing the saturation magnetisation M_S. The term $\left(1 - \frac{H}{H_K}\right)^2$ will then become close to a value of 1 and the energy barrier is only dependent on the anisotropy, M_S and the grain volume. In

58

order to achieve a high density small grain volumes are required. Hence an alloy with high anisotropy should be used as the recording layer.

The demagnetising field H_D

$$H_D = -4\pi M_s \tag{3-34}$$

In conventional recording media Cr is included in the alloy to lower M_s. In order to achieve perpendicular recording media the recording layer must achieve the criteria of $H_K > H_D$ or

$$K_U > 2\pi M_s{}^2 \tag{3-35}$$

The magnetisation of a grain will decrease over a time τ due to thermal energy, following a Néel-Arrhenius law

$$\tau^{-1} = f_0 e^{-\Delta E/k_B T} \tag{3-36}$$

or

$$\tau^{-1} = f_0 e^{-KV(1-\frac{H}{H_K})^2/k_B T} \tag{3-37}$$

Equation (3-36) indicates the time taken for magnetisation decreases to 37% of its original value. For recording media the energy barrier ΔE should be greater than $40 k_B T$ which gives a relaxation time of 10 years, [12]. Since the grain volume is equal to $\pi D_m{}^3/6$ the time constant is extremely sensitive to the median grain diameter.

Increasing the anisotropy improves the thermal stability of the grains but makes it more difficult to magnetise the grains in the desired orientation. The write field H_w is limited by the saturation magnetisation of the write head. The areal density of current conventional HDDs is about 1TB/inch² with a head field of approximately 1T. In order to write information to the medium the write field must be greater than the switching field $H_w > H_S$. The switching field can be expressed as [85]

$$H_W > H_S = H_K \left[1 - \left(\frac{\ln(f_0 t_m) k_B T}{K_U V_m} \right)^{1/2} \right] \tag{3-38}$$

where t_m is the time taken for the magnetisation to cross zero after the application of the field. This means that for a high frequency writing process the coercivity is larger than at low frequency. In the case of conventional recording media the operating frequency is at gigahertz and this leads to a large switching field. Also if K_U is increased to give thermal stability, H_K increases and the increase in H_S reduces the writability.

In order to design or demonstrate a HAMR medium using exchange bias the alignment of the spin structures of the antiferromagnetic and ferromagnetic layers is required. One objective of this study is to couple IrMn to CoCrPt-SiO$_2$. The preferred strategy is by depositing a seed layer to align the (111) orientation of the IrMn with the c-axis of the Co alloy.

Chapter 4

Experimental Techniques

This chapter is focused on the experimental apparatus and methods which have been used to accomplish this study. All the thin film samples prepared were sputtered using a Plasma Quest Ltd. High Target Utilisation Sputtering (HiTUS) system. A thickness calibration process was carried out to show that the crystal rate monitor used in this system is reliable. In recording media the magnetic and structural properties determine the capability of the system. A VSM and AGFM were used to characterise the magnetic properties of the films. A Rigaku X-ray diffractometer and a JEOL 2011 TEM were used to observe the structural and physical properties of the films. High resolution cross section TEM was also used. Based on the exchange bias dependence on the grain size, accurate grain size analysis was undertaken.

4.1 Thin Film Growth

4.1.1 High Target Utilisation Sputtering

All the thin film samples studied in this work were grown using a growth system called High Target Utilisation Sputtering (HiTUS), manufactured by PlasmaQuest Ltd, [70]. It is often difficult to achieve an efficient, precise and controllable sputtering process. However, this sputtering system provides controllable grain size and hence it controls the magnetic properties of the samples, it also capable of achieveing grain segregation of thin film samples using a composite target, [70]. An INFICON XTM/2 deposition rate monitor was used to measure the sputtering rate and hence, the film thickness. These were the essential factors to control the magnetic properties of the samples.
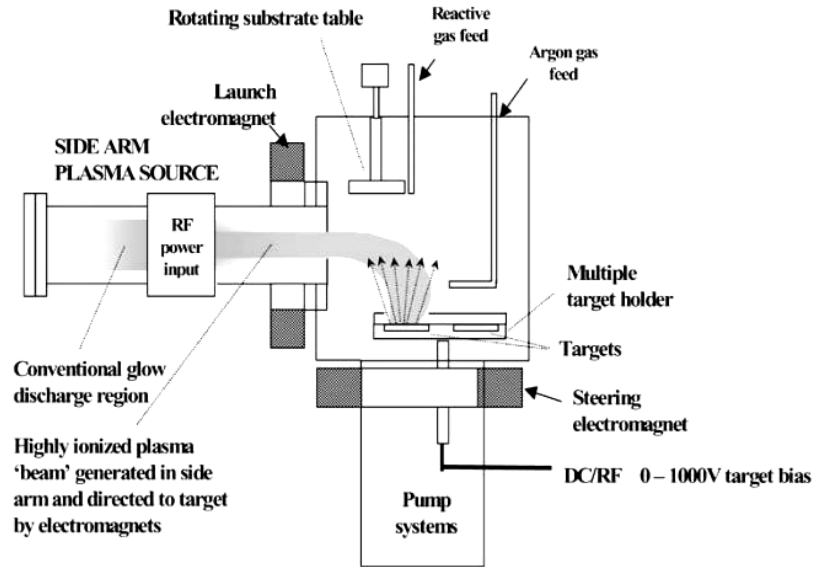
Figure 4.1 Schematic diagram of the HiTUS sputtering system.

A schematic diagram of the system is shown in Figure 4.1. High purity (99.999%) Ar gas was injected into the chamber via the Argon gas feed. The plasma was then generated in a quartz tube which was wound with a three turn coil. A radio frequency (RF) power of 2.5kW at 13.56MHz was generated in the coil by a power supply via a matching unit. Once the plasma was generated, it was then launched into the chamber by the launch electromagnet. A steering electromagnet guided the plasma towards 50mm diameter water cooled targets. Eight different targets can be placed on the multiple target holder, which is driven by a stepper motor. The applied fields of the launch and steering electromagnet were approximately 50Oe and 500Oe, respectively. The HiTUS system generates high intensity plasma of up to 10^{12}-10^{13} ions cm^{-3} at conditions of Ar process pressure 3 x 10^{-3} mbar and an RF power 2kW, [70].

In order to grow high quality thin films, a base pressure of < 5 x 10^{-7}mbar must be reached in the chamber. This can be achieved by a series of pumps which are a rotary pump, a turbo pump and a cryopump. It takes about three hours to pump the chamber down to 5 x 10^{-7}mbar. These pumps are controlled by an in-built Programmable Logic Controller (PLC). This controller also controls the DC bias voltage, RF power, conditioning, pre-sputter and growth time.

No significant sputtering occurs unless a bias voltage is applied to the target. A range of negative dc bias voltages from 0V to -1000V can be applied to the target. When the bias voltage is greater than 100V, significant sputtering of material occurs. At this point, the target current saturates and becomes independent of the bias voltage as shown in Figure 4.2. But as the bias voltage increases the energy of the ions increase and leads to an increased sputtering rate.
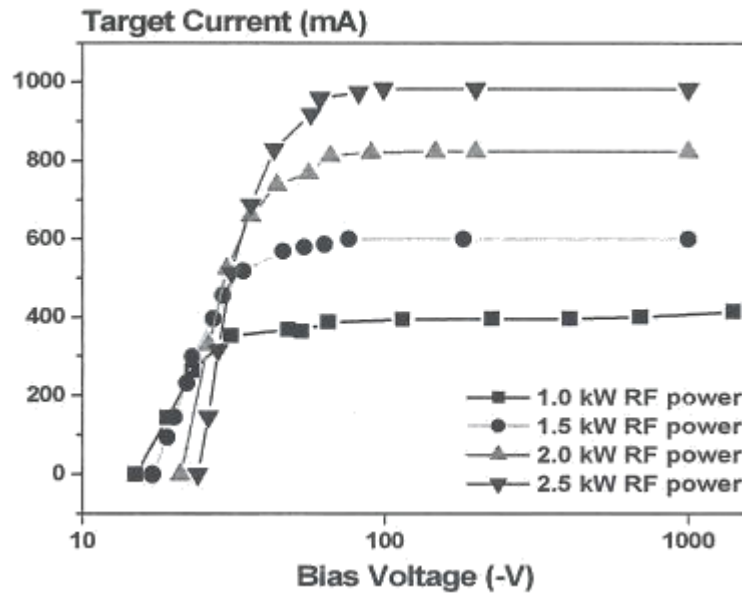
Figure 4.2 Target current verses bias voltage for the HiTUS system, [86].

The grain size affects the physical and magnetic properties dramatically. Therefore, controlling the grain size and size distribution in polycrystalline thin films is the major challenge. The grain size can be controlled by applying different dc bias voltages, Ar gas pressure and RF power, [70]. By changing the target bias voltage, the energy of the Ar ions can be varied. Hence the sputtering rate is varied directly. The grain structure formation in polycrystalline thin films involves crystal nucleation, growth and coalescence. The grain size will be affected by the nucleation and growth if coalescence does not influence grain boundary motion. When nucleation occurs at a random position, a Johnson-Mehl structure results, [87] and the mean grain size can be calculated from Equation (4-1), [88].

$$D_m = 1.203 \times \left(\frac{G}{N_r}\right)^{1/3}$$ (4-1)

63

where D_m is the mean grain size, G is the growth rate in units of Å/s and N_r is the nucleation rate. Therefore, mean grain size increases as the target bias voltage increases.

The substrate holder contains four 5.2mm squares and two 2mm diameter circular holes for Si substrates and copper TEM grids, respectively. It was mounted on a rotating substrate table. This sputtering system allows sputtering of 6 different samples without breaking vacuum. The separation between the substrate holder and the target was approximately 25cm, hence there is a large distance between the target and substrate causing insignificant interaction between the plasma and the substrate. This feature is important for this study because it results in the grain size in the film deposited on a copper TEM grid to be exactly the same as that on the silicon substrate, [86].

Target and substrate cleaning are essential to produce high quality thin films. The targets to be used were cleaned by sputtering for 60 seconds using 1000V bias voltage and 1.5kW RF power. The purpose of this is to remove the top oxidised layer and any other contaminants. The substrates were then cleaned by an Ar plasma for 45 seconds using an RF power of 1.5kW. Before the plasma was switched on the bias voltage was set to zero and the steering magnet was turned off, so that the plasma filled the chamber.

Before deposition started the plasma was conditioned for 20 seconds in order to stablise the Ar gas pressure. The flow of the Ar gas was controlled using a Mass Flow Controller. The range of the Ar gas flow is between 0 to 99 standard cubic centremeter per minute (sccm). In this study process pressures of 1.86mTorr, 3.00mTorr and 30.00mTorr were used. Therefore the corresponding Ar gas flows in sccm units were ~19.5, 27.7 and 245.5, respectively.

A further 10 seconds of pre-sputtering was used to clean the target to make sure the target is ready to deposit. The shutter was then opened to allow the selected material to deposit on the substrate. The layer thickness is proportional to the shutter opening time duration and it is usually set to 9999 seconds. The shutter was then closed manually.

4.1.2. HiTUS Calibration

The thickness of material deposited on the substrate was measured using an INFICON XTM/2 Deposition Monitor. This device is able to measure the thickness of the material deposited on a substrate. It operates by applying an alternating voltage across a piezoelectric quartz crystal. The crystal will then be distorted proportionally to the applied voltage. The alternating voltage causes the crystal to oscillate with a periodic motion. When a specific alternating voltage frequency applied is identical with the natural frequency of the crystal, it causes electro-mechanical resonance. When a small amount of substance is added on top of the crystal its resonant frequency is reduced. The reduced resonant frequency can be calculated from

$$\frac{M_f}{M_q} = \frac{(\Delta F)}{F_q}$$

(4-2)

where M_f is the mass difference due to deposition, M_q is the original mass of the quartz crystal, ΔF is the change in frequency and F_q is the uncoated resonant frequency of the crystal, [89].

The INFICON XTM/2 Deposition Monitor is able to measure the crystal oscillation frequency continuously and therefore has the ability to calculate the thickness of the material via the Z-match equation

$$t_f = \left(\frac{N_{at}\rho_q}{\pi \rho_q F_c Z}\right) \tan^{-1}\left\{Z \tan\left[\frac{\pi(F_q - F_c)}{F_q}\right]\right\}$$

(4-3)

where t_f is the film thickness, N_{at} is the frequency constant of the quartz, ρ_q is the density of the deposited film, Z is the acoustic impedance ratio and F_c is the coated resonant frequency of the quartz, [90]. In order to fulfil the Z-match equation, the INFICON XTM/2 Deposition Monitor requires the density and atomic number ratio for each corresponding material deposited to be known.

It is essential to calibrate the INFICON XTM/2 Deposition Monitor. The calibration was carried out using a calibration tooling factor (TF),

$$TF(\%) = TF_i \left(\frac{t_a}{t_c}\right) \qquad\qquad (4\text{-}4)$$

TF_i is the initial tooling factor, t_a is the deposited thickness and t_c is the thickness displayed on the deposition monitor.

The calibration process was carried out using single layer thin film samples of Ru of different thicknesses in a range of 10nm to 150nm. The thickness of the deposited material was measured using a Mettler UMT2 digital blance with 0.1µg accuracy. 99.99% pure Ru was selected for this calibration due to it being one of the major materials used in this study. Ru has a high degree of corrosion resistance and does not oxidise at room temperature. The bulk density and Z-ratio of Ru are also well defined.

Initially the weight of a 2mm square Si substrate was measured using the Mettler balance. After deposition the weight of the Si substrate and sample was measured using the same balance. As the dimensions of the substrate and the bulk density were known. The thickness of the deposited Ru layer can be calculated. The result is shown in Figure 4.3 where calculated thickness is plotted against deposited thickness.
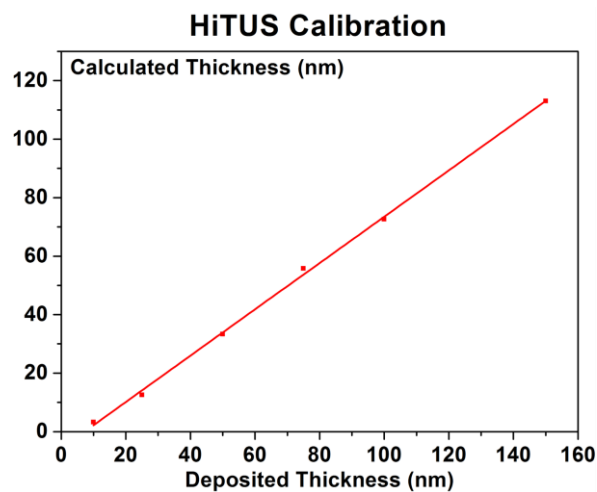
Figure 4.3 The tooling factor calibration for a Ru layer.

The data points shown in Figure 4.3 were fitted by a best fit line. The gradient of the best fit line was 0.79 which means that $t_a < t_c$. In an ideal case, the gradient of the best fit line should be 1. However the Ru that was deposited on the Si substrate was

not 100% dense. This indicates that the measurement follows the tooling factor equation precisely. However the data in Figure 4.3 can be used to give a sufficiently accurate value for film thickness. This technique has been validated previously by calibration against X-ray fluorescence, [91].

In this work the actual thickness of the deposited film was also measured using X-ray Reflectivity (XRR). (See section 4.3.6) Films of nominal thickness of 10nm, 50nm and 150nm where measured and the results are shown in Table 4.1.

Nominal Thickness (nm)	Measured Thickness ± 0.5 (nm)	Difference (%)
10	9.2	8%
50	46.7	7%
150	138.3	8%

Table 4.1 Comparison between deposited and measured thickness from XRR.

Table 4.1 shows the results of the deposited thickness and the measured thickness of a Ru single layer thin film. The results show the reliability of the INFICON XTM/2 Deposition Monitor and the accuracy of the tooling factor. All measurements contain an error within ±8%. A thickness between 5nm to 20nm was most commonly used in this study.

4.2 Magnetic Characterisation

4.2.1 Alternating Gradient Force Magnetometer

The Alternating Gradient Force Magnetometer (AGFM) was invented by Zijlstra in 1970 and modified by Flanders in 1988, [92] [93]. The AGFM is one of the most convenient and sensitive pieces of apparatus used to measure the magnetic properties of materials at room temperature. Measurements such as hysteresis loops, time dependence, isothermal (IRM) and dc demagnetisation (DCD) remanence curve can be made. The time taken for measuring a hysteresis loop is less than three minutes. Therefore the AGFM is ideal for rapid measurements at room temperature of hysteresis loops.

The principle of the AGFM is that by applying an alternating magnetic field gradient to a magnetised sample an alternating force is produced. The sample is mounted on

a quartz leg. This interaction exerts an alternating force on a piezoelectric bimorph. The system is operated at its resonant frequency along the applied field direction. This allows the system to improve the signal to noise ratio giving a noise base of 2 x 10^{-8}emu. The resonant frequency is given by [94]

$$f_{res} = \frac{1t}{2\pi l^2} \left(\frac{Y}{\rho}\right)^{\frac{1}{2}}$$
(4-5)

where t_0 is the thickness, l is the length, ρ is the density and Y is the Young's modulus of the quartz leg. The mechanical resonance quality Q factor determines the quality of the probe. In this study a commercial probe designed to measure thin films with perpendicular magnetisation was used to measure the magnetic properties of the thin film samples. The probe had a Q-factor between 30 – 40 depending on the weight of the sample to ensure that the magnetic measurements were performed with a high signal to noise ratio. The amplitude of the motion is proportional to the magnitude of the field gradient and the magnetic moment of the sample. The signals were then converted to a dc voltage using a lock-in amplifier.

A Model 2900 Princeton Measurement System AGFM was used in this study. A schematic diagram of an AGFM is shown in Figure 4.4. The pole pieces were separated by 12.5mm providing a root mean square field gradient of approximately 4, 0.4 or 0.04Oe/mm. The maximum magnetic field range of the AGFM is between -22kOe to 22kOe. The magnetic moment resolution is $2x10^{-8}$emu for an averaging time of 0.1 second.
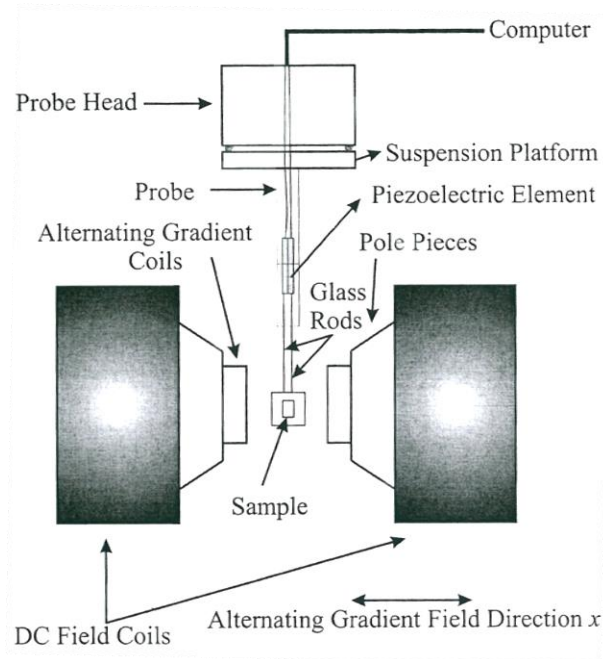
Figure 4.4. A schematic diagram of an AGFM.

A piezoelectric bimorph probe is required in order to measure a sample using the AGFM. The piezoelectric material has a unique feature that it is not sensitive to a changing magnetic field but responds to mechanical motion and acoustic noise. Therefore a high quality measurement requires a quiet environment. The bimorph was attached to a single piece of 2cm long glass rod. At the bottom of the glass rod was a 3mm square glass plate where the sample is placed. The probe was attached to a spring mounted suspension platform.

In order to measure an accurate value of magnetisation, a calibration process was required. The AGFM was calibrated using a 5mm square Pd sample. The size and the magnetic moment of the calibration sample are similar to that of the sample to be measured. The AGFM was used for initial rapid screening of samples.

4.2.2 Vibrating Sample Magnetometer (VSM)

The vibrating Sample Magnetometer (VSM) measures the magnetic properties of a sample. The original VSM was developed by Foner in 1959, [95]. Most of the detailed magnetic measurements presented in this work were measured using a Microsense Model 10 VSM. Figure 4.5 shows a schematic diagram of the system.
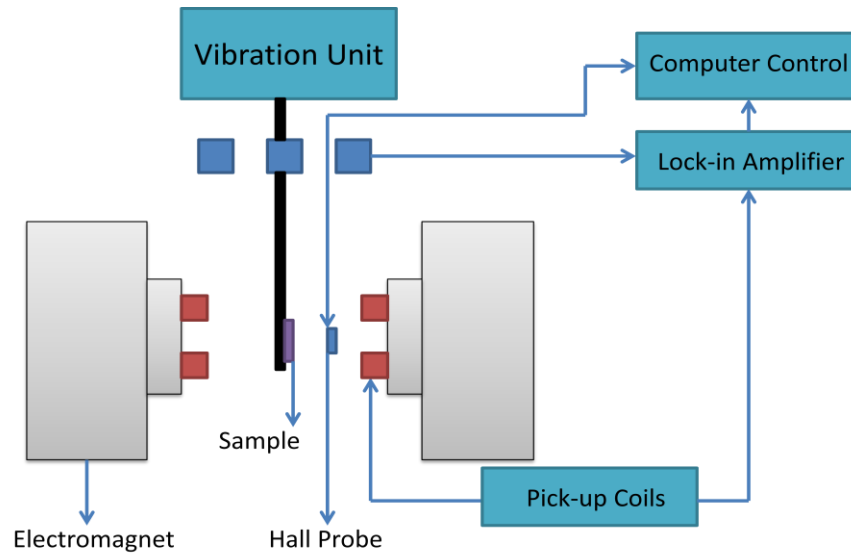
Figure 4.5 Schematic diagram of the vibrating sample magnetometer.

The VSM is based on the principle of Faraday's law. The equation of electromagnetic induction is.

$$\varepsilon = -N\frac{d\varphi}{dt}$$

(4-6)

Where ε is the induced electromagnetic force (e.m.f), N is the number of turns in the coils and $\frac{d\varphi}{dt}$ is the rate of change of flux. The change of flux is induced by a mechanical vibration of the sample under an external magnetic field from the electromagnet. The total magnetic flux penetrating the sample is.

$$\varphi = \overrightarrow{B_M} \cdot \vec{A}$$

(4-7)

where $\overrightarrow{B_M}$ is the magnetic flux density in the material and A is the area of the sample. When the sample is vibrating it induces an e.m.f. which is calculated by Faraday's law

$$\int \varepsilon \, dt = -N\vec{A} \cdot \overrightarrow{M}$$

(4-8)

where M is the magnetisation of the sample.

The sample is located between the pole pieces of an electromagnet, with a field of up to 2T applied perpendicular to the plane. It allows vector measurements with an

accuracy of the determination of the magnetisation vector and angle of ±1.5% and ±1.5°, respectively. The average noise in the vector signal is below 0.5μemu. The vibrator vibrates the sample with an amplitude of approximately 1.5mm and at a frequency of 81Hz, [96]. The change in flux induces an ac voltage which is detected by eight coils, forming four pairs each of two coils. Two pairs of coils measure the magnetic signal in a given direction. The other two pairs of coils mounted orthogonally to the first two pairs and measure the signal at 90° with respect to the first pair. The signals are then amplified and measured by two lock-in amplifiers, which convert the ac signal to a dc voltage proportional to the magnetic moment of the sample. The other feature of the VSM is that the pole pieces can rotate ±540° with a resolution of better than 0.1°. The accuracy and repeatability of the angular setting is ±0.2°, [96].

A calibration is required in order to measure the moment. The geometry and dimension of the calibration sample must be similar to that of the sample to be measured. In this study a Palladium sample was used to calibrate the VSM. Palladium is a Pauli paramagnetic material where susceptibility is independent of temperature around 300K. Another advantage of Palladium is its high corrosion resistance, [97]. The susceptibility of this calibration sample used was 5.86×10^{-7} emu/Oe.

The Microsense model 10 VSM has less sensitivity than an AGFM, but is capable of a greater variety of magnetic measurements. The system is able to perform measurements in the temperature range from 100K to 773K. The variable temperature chamber is 10mm in diameter. The temperature was controlled by a model 9700 temperature controller and an airflow valve, [96]. For high temperature measurements, the airflow valve was used to control the nitrogen gas flow over a heater. At low temperatures, a heat transfer-line is required which is submerges in a liquid Nitrogen dewar. The proportional-integral-derivative (PID) temperature controller system provides a temperature resolution of <0.5K, [96].

4.2.3 Magnetisation Curves

The basic magnetic properties of the thin film samples can be determined from a hysteresis loop. Figure 4.6 shows a typical perpendicular hysteresis loop measurement of a segregated thin film sample.
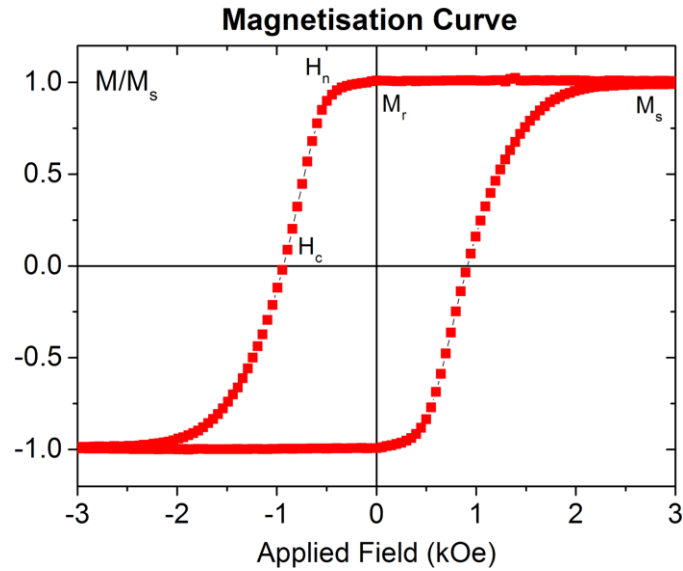
Figure 4.6 Perpendicular hysteresis loop measurement of CoCrPt-SiO$_2$ system.

The majority of the magnetic parameters such as coercivity (H_c), saturation magnetisation (M_s), remanent magnetisation (M), squareness (M/M_s), nucleation field (H_n) and switching field distribution (SFD) can be measured from the hysteresis loop. The most common technique for the measurement of the SFD is based on the Williams and Comstock construction, [81].

$$\left(\frac{dM}{dH}\right)_{H=H_c} = \frac{M/M_s}{(1-S^*)H_c} \qquad (4\text{-}9)$$

where H is the applied field, M is the magnetisation, M_s is the saturation magnetisation, H_c the coercivity and The quantity S^* is defined in Section 3.8.

These parameters are crucial because they can determine the capabilities of a recording medium. In storage media the information is stored in the presence of demagnetising field. Therefore a high coercivity is required in order to sustain the magnetisation in the recording layer. Remanence refers to the remaining magnetisation after the magnetic field removed. For an ideal recording medium a

squareness (M_r/M_s) of 1 is required to prevent information being lost after the field is removed.

Perpendicular recording media is associated with a large demagnetising field (Section 3.5) of ($H_D = -4\pi \cdot M_s$) due to its geometry. Where H_D is the demagnetisaion field and M_s is the saturation magnetisation. It gives rise to an issue when measuring SFD, coercivity and remanence. There have been a number of attempts via experiments and theory to correct the demagnetising field in perpendicular recording media measurements, [98] [99] [100]. However none of them can provide a possible solution to remove the demagnetising field. Therefore the hysteresis loops which are shown in this study have been plotted using magnetisation against applied field as shown in Figure 4.6.

4.2.4 Thermal Activation Measurements

The Model 10 VSM is capable of measuring the saturation magnetisation from a ferromagnetic (F) material via its hysteresis loop. The Model 10 VSM is also able to measure the magnetic properties of antiferromagnetic (AF) materials. This can be achieve using thermal activation measurements.

Thermal activation measurements were used to measure the blocking temperatures of the samples, [101]. Blocking temperature measurements for granular AFs can be undertaken by the following steps and summarised in Figure 4.7. There are known as the York Protocols, [59]. The theory of the York Protocols was discussed in Section 3.7.

1. The AF grains were set under a saturating applied field of 20kOe at a temperature T_{set} for 3600s.

2. The sample was field cooled to T_{NA}.

3. The applied field was then reversed and the sample was heated to a thermal activation T_{Act} for 1800s.

4. The sample was then cooled to T_{NA} with the field applied.

5. A reverse field was then applied so that the training effect was removed.

6. Hysteresis loops were then measured at T$_{NA}$ where all AF grains are thermally stable.

After the first hysteresis loop subsequent loops were measured from step 3 until $T_{Act} = T_{set}$.
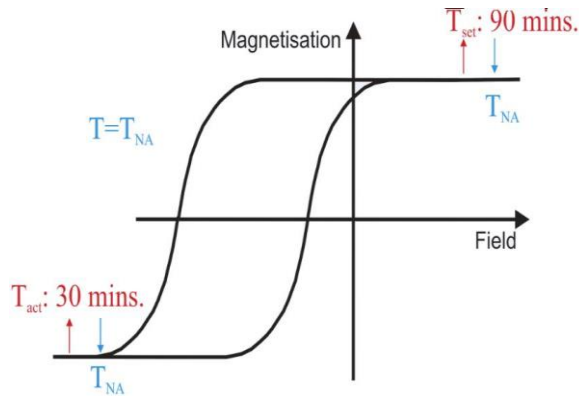
Figure 4.7 Schematic diagram of measurements steps of the York Protocol, [59].

This measurement procedure is based on the York Model of exchange bias. The volume of the AF grains in a polycrystalline sample exhibit a grain volume distribution as shown in the schematic diagram in Figure 4.8. V_c is the minimum AF grain volume which is thermally stable at T_{NA}. AF grains with volume below V_c are too small and do not contribute to the loop shift H_{ex}. V_{set} is the maximum AF grain volume that can be set at T_{set}. For the AF grains with volume above V_{set}, they are not able to align with the applied field due to the energy barrier $K_{AF}V_m$ being too large.
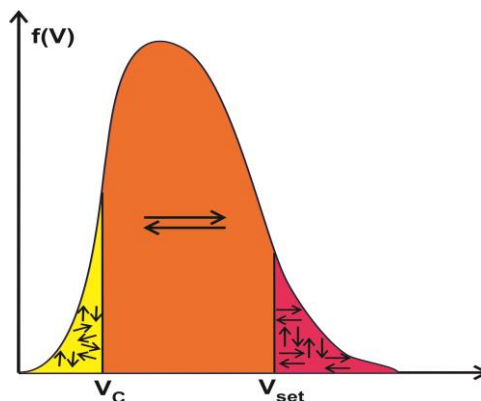
Figure 4.8 Schematic diagram of AF grain size distribution, [59].

As T_{Act} is increased, progressively more AF grains will be reversed in the opposite direction. This eventually leads to the exchange field H_{ex} being reduced to zero

74

when half of the AF volume is oriented in the opposite direction. H_{ex} will eventually become positive. This is due to more of the reversed AF grains being re-orientated. A blocking temperature curve will then be obtained an example of which is shown in Figure 4.9. The median blocking temperature $< T_B >$ can then be measured at H_{ex}= 0. At this point equal volumes of the AF grains are orientated in opposite directions which allows for the calculation of K_{AF} using

$$K_{AF} = \frac{ln(t_{set}f_0)k_B<T_B>}{V_m} \qquad (4\text{-}10)$$

where t_{set} is the setting time at the setting temperature T_{set}, f_0 is an attempt frequency with a typically value of $10^{12}\,s^{-1}$, [76]. k_B is the Boltzmann's constant, $< T_B >$ is the median blocking temperature and V_m is the grain volume.
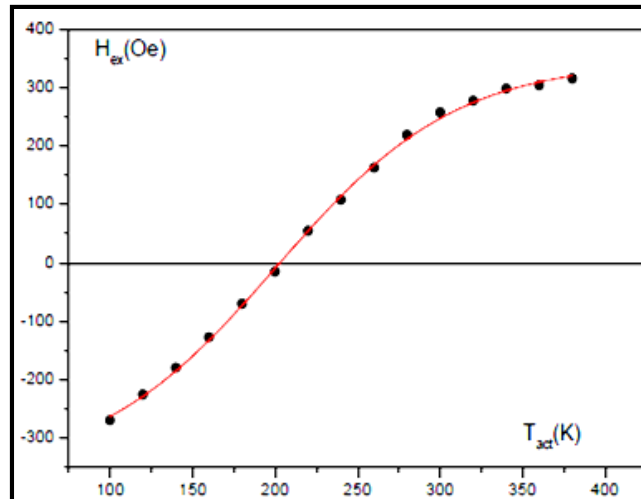
Figure 4.9 Typical blocking temperature measurement, [59].

4.3 Structural Characterisation

4.3.1 Transmission Electron Microscopy

Transmission Electron Microscopy (TEM) is one of the main techniques used to measure the physical structure of a thin film sample on an atomic scale. The resolution of a TEM can be explained using the classical Rayleigh criterion which is shown in Equation (4-11), which states that the smallest distance than can be resolved is δ.

$$\delta = \frac{0.61\lambda}{R^* \sin\beta} \qquad\qquad (4\text{-}11)$$

where δ is the smallest distance can be resolved in a unit of radian, λ is the wavelength, R^* the refractive index of the viewing medium and β is the semi-angle of collection of the magnifying lens. The value of β is very small and the refractive index is ~1. Therefore Equation (4-11) can be modified to $\delta = \frac{0.61\lambda}{\beta}$. Green light is in the middle of the visible spectrum. Its wavelength is approximately 500nm. Therefore the resolution for a visible light microscope is about 300nm, [102]. The wavelength of a 100keV electron is about 4pm. Therefore a TEM can provide a resolution 10,000 times that of a visible microscope, [102].

A JEOL JEM-2011 TEM was used to identify the grain sizes and grain boundries in this work. Figure 4.10 shows a schematic diagram of the TEM. A Lanthium hexaboride (LaB$_6$) filament with a $1\mu m$ tip is located at the top of the column which is operated under an ultra high vacuum of 10^{-10} mbar. It requires a series of pumps which are roughing, diffusion, turbomolecular, ion and cryogenic pumps. The electrons are emitted through a thermionic process where the filament is heated to a temperature greater than the work-function φ_W. The electrons are then accelerated by a potential of 200keV. The electrons pass through a condenser lens which consists of many electromagnetic copper coils. The current through these coils deflects the path of the electrons. The role of the condenser lens is to control the number of electrons travelling through the system. The electrons then interact with a specimen located at the top of the objective lens. This is used to focus the diffracted electrons after the interaction with the specimen. An intermediate image is then produced. A set of intermediated lenses and projector lenses then magnify the image which is projected onto the fluorescent screen. A digital image is collected by a charge-couple device (CCD) camera.
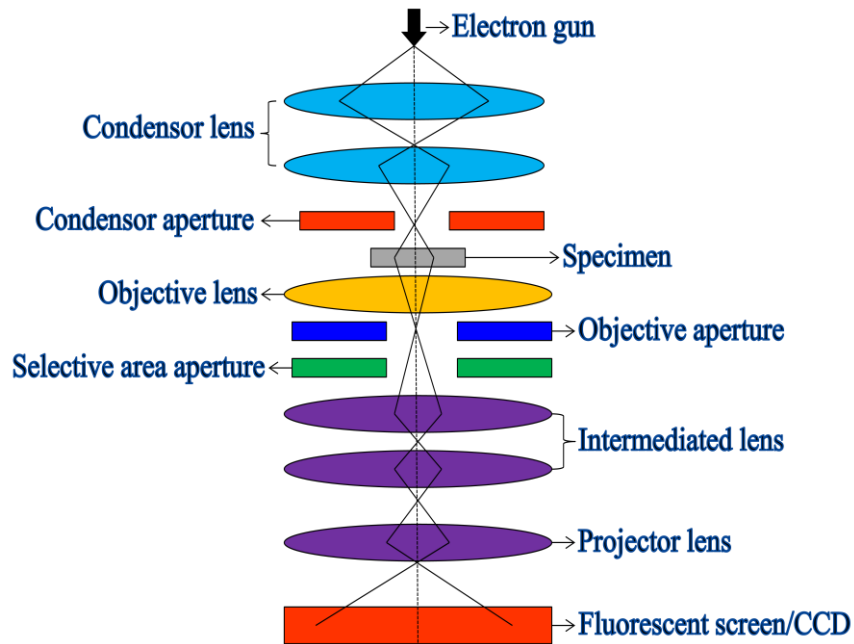
Figure 4.10 Schematic of a conventional transmission electron microscopy.

The TEM also allows the observation of the crystal structure of the specimen. This can be achieved using selective area diffraction pattern. A selective area aperture was inserted at the intermediate image as shown in Figure 4.11. The diffraction pattern is then produced on the fluorescent screen.
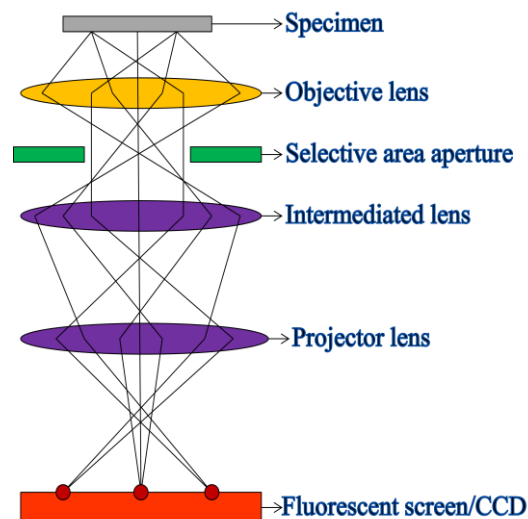
Figure 4.11 Ray diagrams of the diffraction process.

The ring pattern that appears on the fluorescent screen can be explained using Bragg's Law. However the diffraction angle in the TEM is so small that Bragg's Law can be modified to

$$Rd = \lambda L \qquad (4\text{-}12)$$

where λ is the wavelength of the electron, R is the radius of the diffraction ring, L is effective length between the sample. The effective length was calibrated by a JEOL engineer using a pure Al sample. d is the lattice spacing given by

$$d = \frac{a}{\sqrt{h^2+k^2+l^2}} \qquad (4\text{-}13)$$

where a is the lattice constant and h, k, l are the Miller indices which correspond to a grain diffraction plane. The selected area diffraction pattern was used in this study to identify the orientation of IrMn (111) planes.

In this study bright field imaging mode was most commonly used to identify the physical structure of a thin film sample, such as the median grain size, its distribution and grain boundaries (Section 4.3.4). The principle of bright field imaging is to select a direct electron beam using an objective aperture as shown in Figure 4.12a, [102]. A bright field TEM image of a segregated CoCrPt-SiO$_2$ thin film sample is shown in Figure 4.12b. The grains which achieved the Bragg condition appears as a dark colour.

a.) b.)
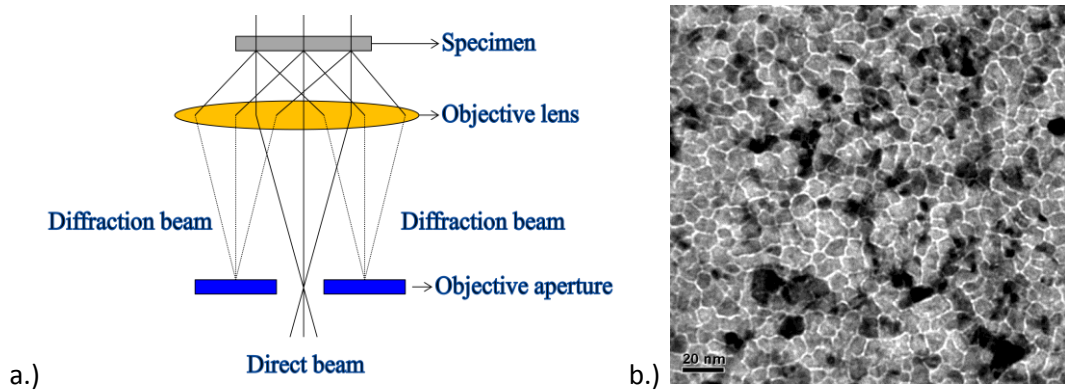
Figure 4.12a) Ray diagrams of bright field imaging. b) Bright field TEM image.

4.3.2 Cross Sectional Sample Preparation

Cross sectional TEM provides information regarding the physical structure of thin film samples. The images can show effects such as diffusion and roughness between multiple layers, selected area electron diffraction and segregation. However sample preparation is time consuming and complicated. A 5mm square

sample was cut into half. The two pieces of the samples were glued together face to face using epoxy resin. Two pieces of Si wafer were glued at the top and bottom of the sample as shown in Figure 4.13. These were used to monitor the thickness of the specimen during the polishing process.
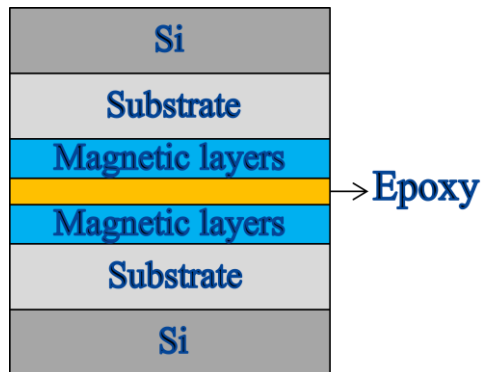
Figure 4.13 The overall structure of a cross section sample.

One side of the sample has to be polished to a smooth surface before sticking it to a Cu TEM grid as shown in Figure 4.14. This can be achieved using 15 μm diamond polishing pads to square off the sample. This is followed by the use of 9, 6, 3 and 1 μm polishing pads to give a high quality polished surface. The Cu TEM grid was then glued perpendicular to the sample. The sample was then flipped over and polished on the other side. A 15μm polishing pad was used to grind down the sample thickness to ~0.30mm. The sample was then polished to ~0.15mm using a 6μm polishing pad. A 3μm pad was used to polish down to ~0.10mm. The thickness of the sample can be checked using a micrometer up to this stage. An optical microscope was then required to check the sample thickness once it was less than ~0.10μm. When the sample thickness was down to approximately 20μm an orange colour can be observed through the microscope. The sample is now ready for the final polishing stage.
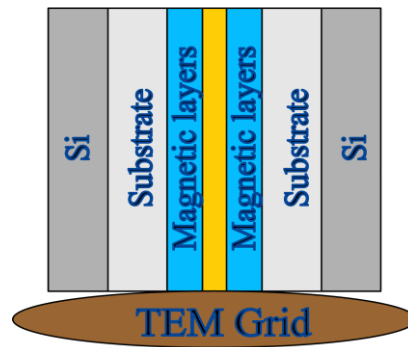
Figure 4.14 Schematic diagram of a sample which is ready for polishing

The sample was placed in an Ar-ion Precision Ion Polishing System (PIPS). In this system there are two ion guns which are positioned to the left and right hand side with respect to the sample. The energy of the ion beams was set to 3.5keV for samples on Si substrates. Each electron gun was set to a top and bottom angle of 6° with respect to the sample. The sample was rotated at about 3 revolution per minute during the thinning process to ensure that the sample is thinned evenly. A schematic diagram of the ion beam polishing process is shown in Figure 4.15.
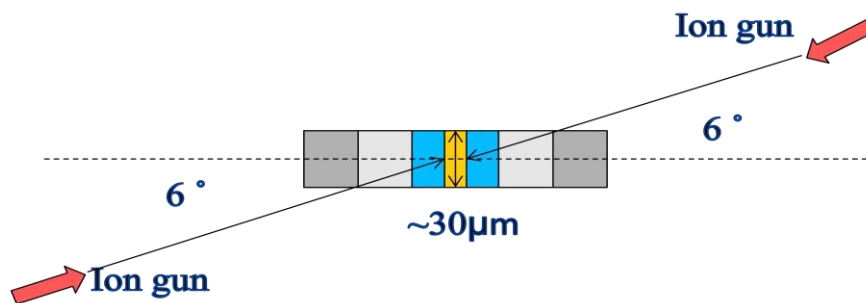
Figure 4.15 Schematic diagram of the PIPS process.

Figure 4.16 shows a typical bright field cross section TEM image of a segregated CoCrPt-SiO$_2$ sample. The image clearly shows the void structure which was created by sputtering two layers using different process pressures. Also the grain structures and SiO$_2$ insulator can be observed in this image.
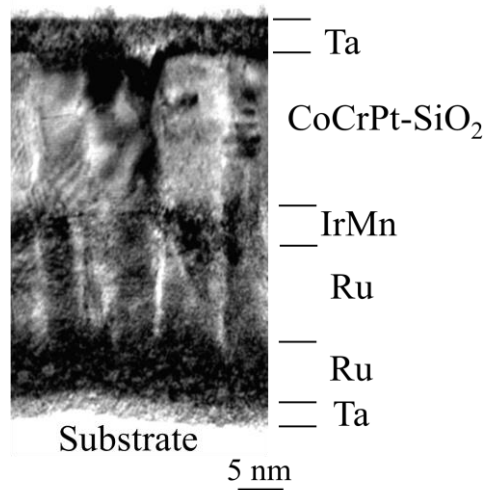
Figure 4.16 Bright field cross section TEM using 250k magnification.

It is not essential to achieve high quality segregation and dispersion of the CoCrPt-SiO$_2$ layer in this study. The primary objective is to discover a possible way to exchange couple between the conventional recording layer CoCrPt-SiO$_2$ and the IrMn layer in the perpendicular direction.

4.3.3 Scanning Electron Microscopy

This study has largely focused on IrMn which is an AF material. The atomic ratio between these compounds has a significant influence on the crystallographic structures and magnetic properties. An FEI Sirion XL30 scanning electron microscope (SEM) was used in order to indentify the compositions of the AF material precisely. This system operates with an Oxford Instruments INCA energy-dispersive X-ray spectroscopy (EDX) system which was used to analyse the composition of the materials. A schematic diagram of the SEM is shown in Figure 4.17.

The principle of EDX is to rely on the X-ray emission spectrum from the samples. A high energy electron beam is emitted from the electron gun to interact with the sample. Electrons in the film are then excited from their ground state into an excited state. When the electron is de-excited to its original state, X-ray photons are emitted. These photons are characteristic of the energy between two states for a given atom and allows the composition to be measured.
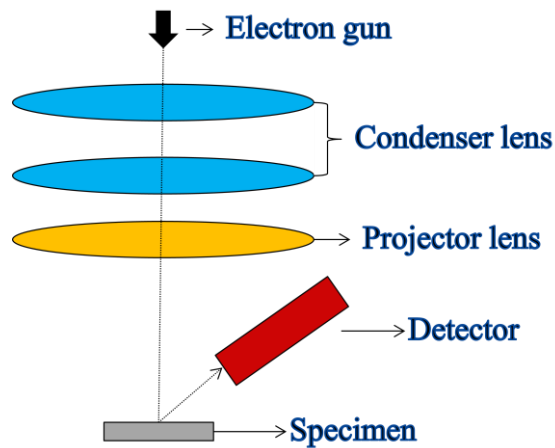
Figure 4.17 Schematic diagram of the FEI Sirion XL30 (SEM).

This system consists of three main components which are the electron gun, the demagnification unit and the detection unit. A W filament was used in this system with a current of about 2.4A. The SEM was operated at 15kV so that the electron beam has high enough energy to penetrate the sample. A series of electron optical systems were used to focus the electron beam onto the specimen. A secondary electron detector, which is a scintillator type, was used for all scans. The operation of the detector uses secondary electrons generated by the primary beam to produce a signal which is then amplified and converted into an electrical voltage.

Ir and Mn have melting points of 2410°C and 1244°C, respectively, [103]. The large difference in melting points results in Mn rich alloy formation in the thin film samples. Therefore composition analysis was required to determine the atomic ratio between Ir and Mn. A single layer of 10nm IrMn was deposited on a Si substrate using six different bias voltages. The samples were measured using the EDX system and the results were analysed using an analysis package program called Noran System Six which is provided by Thermo Scientific. This analysis technique assumes a homogenous distribution of the elements within the interaction volume in the sample of the incident beam. The 15kV electrons excite X-rays in the IrMn layer as well as the Si substrate. Hence the value of the Ir and Mn concentration is not accurate. However as the analysis conditions are identical the EDX analysis performed in this work was used to observe the trends of increasing the Ir to Mn ratio as the bias voltage is varied.

The EDX scans were performed using an electron beam energy of 15kV for three minutes to ensure the accuracy of the scan. The results in Table 4.2 show that in low bias voltage growth the level of Ir in the film was reduced below the 25% composition in the target. However at high biases, greater than 25% Ir results. Therefore Mn was dominant when low bias voltages were used. In effect a low bias voltage leaves the target surface Ir rich so that subsequent growth at high bias results in a high Ir content in the film. This indicates the need for careful target conditioning prior to growth. However Ir content in the range between 12.9% to 22.5% gives the optimum values of exchange bias, [104]. Note that the required composition is $IrMn_4$ not $IrMn_3$, [107].

Sample Bias Voltage (V)	Ir (± 2 at.%)	Mn (± 2 at.%)
400	17	83
500	18	82
600	20	80
700	27	73
800	29	71
900	30	70

Table 4.2 IrMn composition in different bias voltages.

There was a recent study of the variation of H_{ex} as a function of Ir content by Aley et al. [105] as shown in Figure 4.18. It was based on the work of Tsunoda et al., [104]. It is interesting that when the Ir content is between 17.5% and 20% a small drop of H_{ex} was observed. Since we have already shown that the IrMn content of the sample is approximately 80 at. % Mn and 20 at. % Ir. As the extra Mn atoms diffuse to the IrMn it resulted an excessive Mn content and therefore Ir content was reduced to less than 20 at. %. The H_{ex} was then decreased slightly compared with the original result.
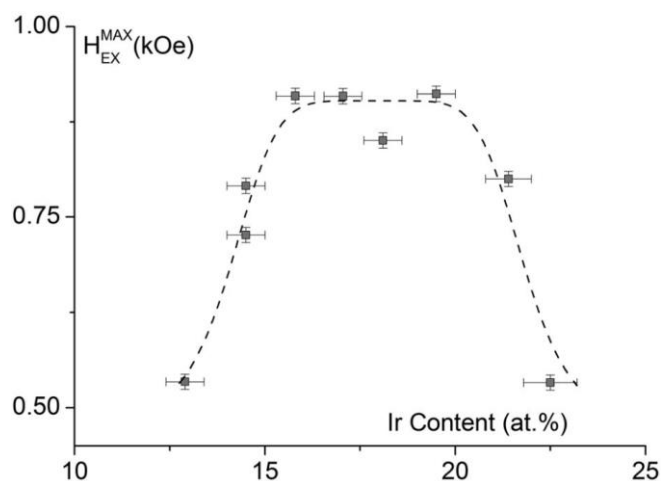
Figure 4.18 Variation of H_{ex} with Ir cotent, [105].

The most accurate way to calibrate the EDX system is by analysis of the sample using chemical techniques. However since Ir does not dissolve in acid there is no possible way to use this technique. The data shown in Table 4.2 was based on an experimental EDX technique therefore it has a large error of about 10%. The result shown in Table 4.2 should also be interpreted as a trend rather than absolute values.

There is a physical feature which can be noticed by observing the IrMn target. The sputtering target used in HiTUS is made by compressed Ir and Mn powder. The surface of the target can be seen as small Ir practical. Hence during the deposition using high energy plasma the substrate would expected to result Ir rich content.

4.3.4 Grain Size Analysis

One of the challenges of heat-assisted magnetic recording media is the reduction of grain size. In FePtX-Y perpendicular media the average grain size is about $3 - 5nm$, CoCrPt-SiO$_2$ perpendicular magnetic recording media has a relatively large grain size of $6 - 8$ nm as discussed by Weller et al., [4].

A bright field TEM image is required for grain size analysis. Typical examples of bright field TEM images for polycrystalline and segregated thin film samples are shown in Figure 4.19a and 4.19b, respectively. In Figure 4.19b the dark and grey

areas correspond to the CoCrPt alloy. This is because of the CoCrPt alloy is composed of relatively heavy atoms compared with SiO_2. Therefore the scattering from the electrons is stronger. Hence the dark areas of the images are used to measure the grain size. Only the grains which met the Bragg's condition were used in the analysis.
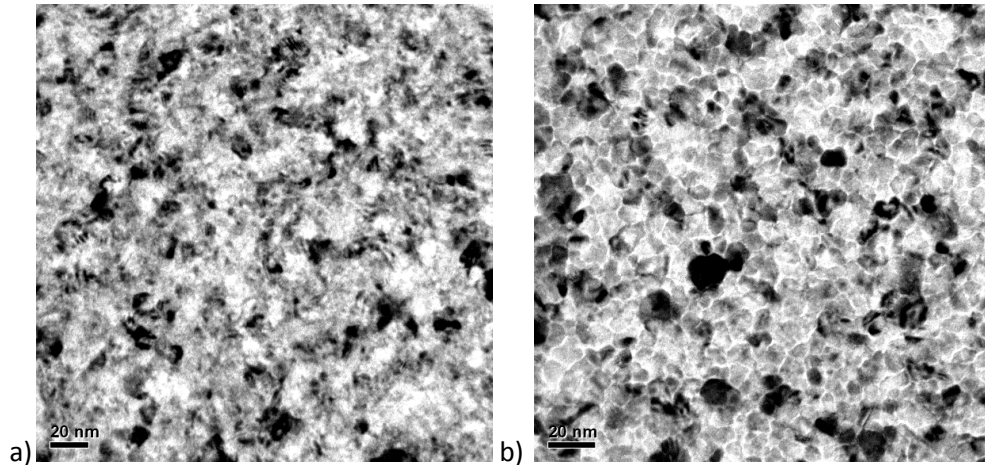
Figure 4.19 Bright field TEM image with a) a $(Co/Pt)_n$ polycrystalline structure and b) a segregated thin film sample with CoCrPt-SiO_2 system.

A Zeiss particle size analyser shown in Figure 4.20 was used to measure the grain size and its distribution. An original TEM image is required to print on paper in order to measure the grain size accurately. The particle size analyser projects a circular light spot onto a screen. The diameter of the light spot can be adjusted by an aperture. When the area of the light spot is equivalent to that of the grain, a pedal is depressed and a hole is punched through the image and registered as a voltage using a Lab View program. However, the grains that grow in a thin film sample are not perfectly circular. Therefore the area of the light spot has to be adjusted to be equal to that of the grain.

Figure 4.20 Zeiss particle size analyser.

The data was then converted to an actual scale using the size bar. The size distribution of a polycrystalline film follows a log-normal distribution. It is defined as a function so that the log of a random variable follows a Gaussian distribution, [106].

$$f(D)dD = \frac{1}{\sqrt{2\pi}\sigma_{lnD}D} exp\left\{-\frac{[(lnD)-\mu^2]^2}{2\sigma_{lnD}^2}\right\}dD \qquad (4\text{-}14)$$

Where σ_{lnD} is the standard deviation of lnD, D is the grain diameter and μ is the mean of lnD which defined as $\mu = \frac{\sum Nln(D)}{\sum N}$. The log-normal distribution is normalised by a factor of $\frac{1}{\sqrt{2\pi}\sigma_{lnD}D}$ therefore

$$\int_0^\infty f(D)dD = 1 \qquad (4\text{-}15)$$

The key parameters of the distribution are the median grain diameter D_m and σ_{lnD}, which can be calculated using [106]

$$D_m = e^\mu \qquad (4\text{-}16)$$

$$\sigma_{lnD} = \left[\frac{1}{\sum N}\sum N(lnD)^2 - \left(\frac{1}{\sum N}\sum NlnD\right)^2\right]^{1/2} \qquad (4\text{-}17)$$

The standard deviation of the grain diameter distribution is related to that of the grain volume distribution

$$\sigma_{lnV} = 3\sigma_{lnD} \qquad (4\text{-}18)$$

The median volume of the grains $< V_m >$ can be calculated using $< V_m >= \pi t D_m^2$ where t is the thickness of the layer.

For all the grain size analysis presented in this work at least 500 grains were measured for each sample in order to obtain an accurate statistical measurement.

4.3.6 X-ray Diffractometer

X-ray diffraction (XRD) is one of the most commonly use methods to identify the crystallographic structure of thin film samples. A schematic diagram of Bragg diffraction is shown in Figure 4.21 and the functions of the labelled parts are shown in Table 4.3. The principle of XRD is based on Bragg's Law given by

$$\lambda = 2d \; sin\theta \tag{4-19}$$

where λ is the wavelength of the X-ray, θ is the scattering angle between the incident beam and the crystal planes, d is the lattice spacing, which for a cubic strucutre is given by

$$d = \sqrt{\frac{a^2}{h^2+k^2+l^2}} \tag{4-20}$$

where a is the lattice constant of the material and h, k and l are the Miller indices for a specific plane,.
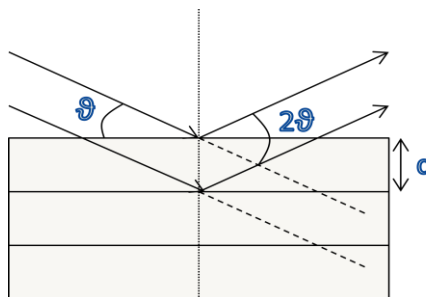
Figure 4.21 Schematic diagram of X-ray diffraction.

All scans were undertaken using a Rigaku SmartLab X-ray diffractometer shown in Figure 4.22 and the functions of the labelling parts are listed in Table 4.3. This system is equipped with a high intensity 9kW rotating anode X-ray generator. The

maximum voltage and current are 45kV and 200mA, respectively. The stability of the voltage and current are within ±0.005% for a 10% input power variation.
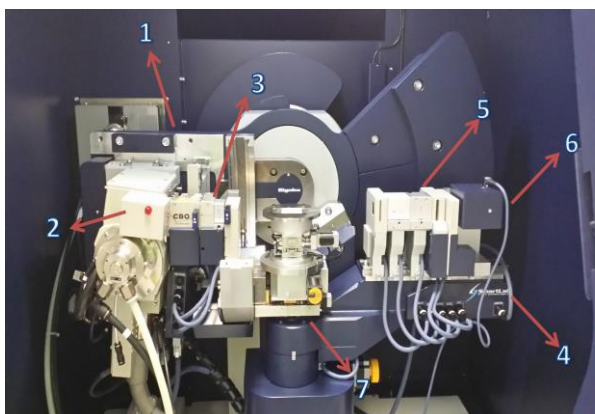
Figure 4.22 Rigaku SmartLab X-ray diffratometer.

The wavelength of the X-rays depends on the type of target. In this study a Cu target was used to generate $K\alpha$ X-rays. The beam contains both $K\alpha_1$ and $K\alpha_2$ X-rays whose wavelengths are 1.541Å and 1.544Å, respectively. An optimal measurement can be achieved just using $K\alpha_1$ X-rays. This can be achieved using a Ge monochromater crystal to remove the $K\alpha_2$ component for incident optical setting. The reflected X-rays were detected by a NaI scintillation counter.

1. Theta_s arm	Arm for controlling X-ray beam incident angle.
2. X-ray tube	X-ray generating device.
3. Incident optics	Optical device for achieving desired incident X-ray conditions.
4. Theta_d arm	Arm for controlling the X-ray detector angle.
5. Receiving optics	Optical device for achieving desired X-ray receiving conditions.
6. Detector	X-ray detector.
7. Sample stage	Adjusts the position and orientation of the sample to be measured.

Table 4.3 The corresponding labels of Figure 4.22.

Figure 4.23 shows a schematic diagram of a (NaI) scintillating counter detector. When the incident radiation strikes the NaI crystal, its atoms are excited by the radiation and photons are emitted. The photocathode is then excited by the photoelectric effect and more electrons are emitted. The electrons interact with the dynodes inside the photomultiplier tube. Each dynode has the ability to release further electrons. This is achieved as the electrical potential of the subsequent

stages of the dynodes are higher than the previous stages. The electrons eventually strike the anode and a pulse signal is then generated.
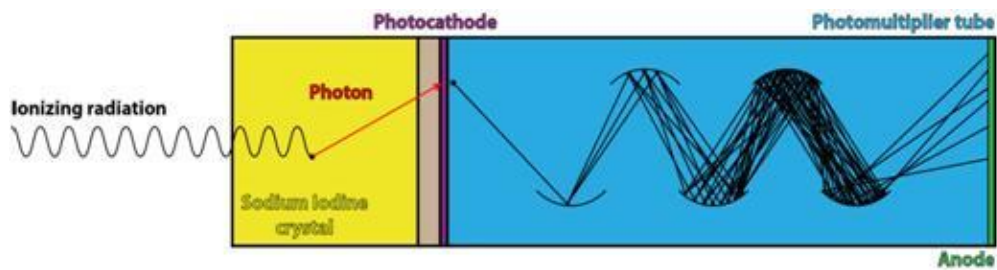
Figure 4.23 Schematic diagram of scintillating counter (NaI) detector.

The Rigaku SmartLab XRD is equipped with a high resolution $\vartheta - \vartheta$ goniometer which enables the X-ray source and detector to be positioned with an accuracy of 0.001° step size which is provided by the Rigaku handbook. This allows the system to perform high resolution $\theta - 2\theta$ scans. To obtain a $\theta - 2\theta$ scan the detector moves twice the angle of the incident X-ray source as shown in Figure 4.24. Therefore as the angle θ increases, the scattering vector K_g, move upwards in reciprocal space. This gives all the crystallographic information from the planes perpendicular to the substrate normal, [107].
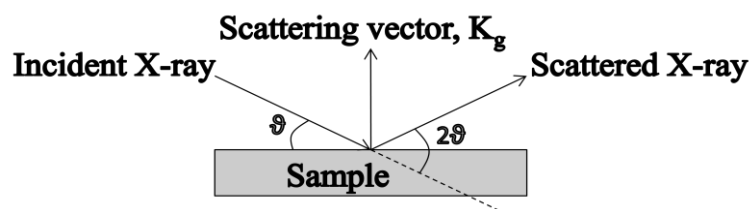
Figure 4.24 Schematic diagram of $\theta - 2\theta$ scan.

Rocking curve measurements have been used to analyse the distribution of the crystal orientations in the films. The crystal quality of a thin film sample with perpendicular anisotropy is partially defined via the distribution of crystallographic axes normal to the film surface and the distribution of crystallographic axes across the surface. Figures 4.25a, b show schematic diagrams of the rocking curve geometry for tilt distribution and twist distribution, respectively. A rocking curve measurement can be achieved by setting an X-ray source and detector at a 2ϑ value for a targeted reflection. The source and detector are then rocked over a

range of values of Ω. The receiving slits are relatively wide so that the changes in intensity can be scanned accurately.

a) Geometry of tilt distribution   b) Geometry of twist distribution
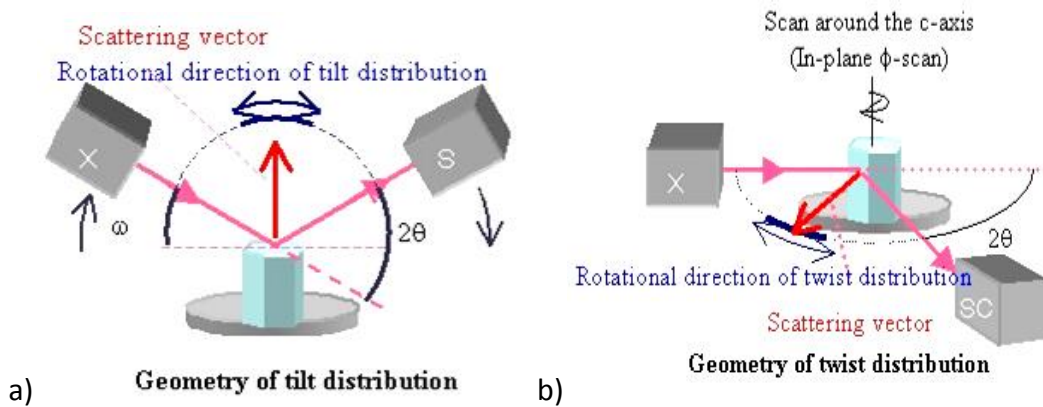
Figure 4.25. Schematic diagram of a) perpendicular b) in-plane rocking curve measurements, [108].

In this study rocking curve measurements have been used to measure the crystalline c-axis distribution of segregated Ru dual seed layer samples. A typical out-of-plane rocking curve measurement is shown in Figure 4.26. The full width half maximum of curves such as that shown in Figure 4.26 corresponds to the dispersion of the Ru c-axes. For this study it was essential to perform rocking curve measurement on dual seed layers samples since the c-axes of the Ru (002) and CoCrPt-SiO$_2$ (002) are extremely close to each other. Even so the optical configuration of the Rigaku system is not able to resolve the peaks completely. Therefore a possible way to estimate the c-axis distribution of the CoCrPt-SiO$_2$ is by measuring the FWHM of the dual Ru seed layer sample.
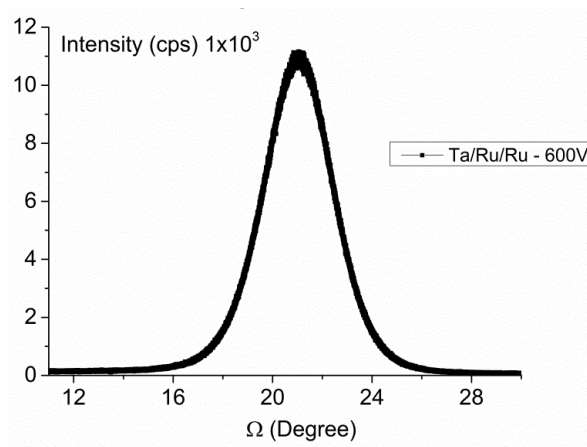
Figure 4.26 Typical rocking curve measurements.

The technique of pole figure measurement has also been used in this study to analysis the texture of samples averaged over a large area. The scan can be achieved by fixing the 2θ angle and the diffracted intensity is then collected by changing either the angle α or β, where α is the tilt angle from the sample surface normal direction and β is the angle around the sample surface normal as shown in Figure 4.27. For a polycrystalline sample an even distribution intensity will be observed from the scan.
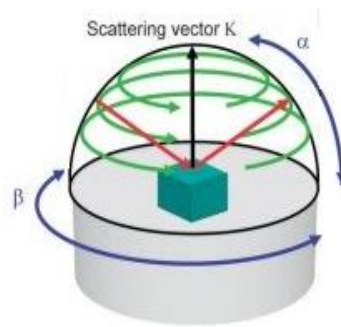
Figure 4.27 Pole figure scan configuration with a fixed 2θ angle, [109].

4.3.6 Reflectivity Scans

An X-ray reflectivity (XRR) scan is typically used to measure the density, thickness and roughness of thin film samples. In this study reflectivity scans were used to measure the thickness of single layer thin film samples. (See section 4.1.2) The principle of the reflectivity scan is based on the physical phenomenon of total reflection as shown in Figure 4.28.

For an incident X-ray the refractive index R^* is given by

$$R^* = 1 - \delta_{R^*} - i\beta_{R^*} \qquad (0 \leq \delta, \beta) \qquad (4\text{-}21)$$

where δ_{R^*} and β_{R^*} can be calculated from the wavelength of the incident X-rays, the composition and density of the material. For normal materials the values of δ_{R^*} and β_{R^*} are approximately 10^{-6}, [110].
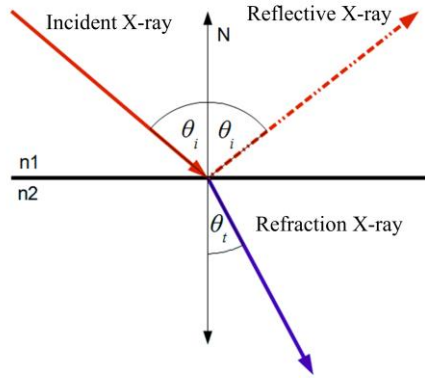
Figure 4.28 Schematic diagram of X-ray reflectivity.

When the incident X-ray is at an angle smaller than a critical angle, total reflection occurs. Therefore the intensity of the reflected X-ray is equal to that of the incident X-ray. However when the incident angle is larger than the critical angle, refraction and reflection occurred. Hence the intensity of the reflected X-rays decreases. An oscillation is observed in the intensity of the X-rays reflected from multilayer samples. This is due to the interference between two reflected X-ray components of the multilayer. The incident angle and reflected X-ray intensity are then used to measure the composition or density of the materials.

Figure 4.29 shown a typical reflectivity scan for a multilayer sample. It also shows the relationship between reflectivity profile and structure parameters. The period of oscillation represents the thickness of the films. The amplitude of the oscillations depends on the density differences between the films and the substrate and the roughness of the surface and interface.
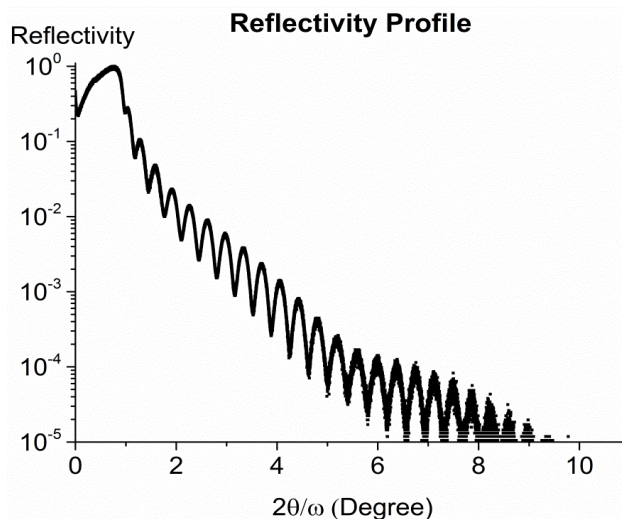
Figure 4.29 Reflectivity measurement of a multilayer sample, [111].

It has been shown that the HiTUS system is capable of producing a segregated thin film sample similar to a conventional recording medium. These segregated regions are filled by SiO_2 which is used to prevent the RKKY exchange coupling between grains. The crystal monitor equipped in HiTUS gives a highly accurate thickness confirmed by the XRR scans. The Model 10 VSM provides a temperature range control in order to examine thermal stability of the samples. Detailed experimental measurements are presented in Chapters 5 & 6.

4.4 Errors and Calibration

The sample film thickness monitor was calibrated and is discussed in Section 4.1.2. The TEM was calibrated by the JEOL engineer and the accuracy of images at 100k is 0.1nm. 500 grains were measured for grain size analysis to ensure good statistics and the error in the median grain diameter and the standard deviation of lnD are 0.2nm and 0.02, respectively. The field resolution of the Model 10 VSM is less than ±5Oe in 10kOe and ±10Oe in 1kOe. All hysteresis loops in this study were plotted M/M_s against applied field to avoid any consideration of the sample volume. The typically error in M/M_s for the samples studied is about 2%. The applied field is calibrated by a Hall probe.

Chapter 5

Perpendicular Exchange Bias Using [Co/Pt]$_n$

An initial study of perpendicular exchange bias has been undertaken using Co/Pt multilayers. Such a system could find application in patterned heat assisted magnetic recording media. The magnetic properties such as squareness and coercivity are dependent on the deposition conditions. This is due to the interfacial anisotropy of the Co/Pt multilayers. Hence a series of structural optimisations were undertaken. In order to achieve exchange bias spin alignment between the antiferromagnetic (AF) and ferromagnetic (F) layers is required. Different seed layers were used to induce the desired structure to achieve perpendicular exchange bias.

5.1 Growth Conditions

For many potential device applications of Current Perpendicular to Plane-Giant magnetoresistance (CPP-GMR) or Tunnel Magnetoresistance (TMR) there is a requirement for one of the F layers in the stack to have its magnetisation fixed or pinned in one direction. This can be achieved via either the use of high coercivity materials or an exchange bias structure. Any ferromagnetic material with strong perpendicular anisotropy can be used to form a high coercivity layer. The most commonly used ferromagnetic layer is a Co/Pt multilayer as discussed by Liu et al., [112]. In this system it is easy to control the out of plane anisotropy by varying the number of repeat units or the Co or Pt layer thicknesses, [113]. These anisotropy tuning method have also been used in (Co/Pd) multilayer systems, [114]. Therefore

this is a model material system for bit patterned media as discussed by Hellwig et al. [114] and references therein.

(Co/Pt)$_n$ multilayers grow naturally with perpendicular anisotropy. This is due to the 2-ion anisotropy induced in the Co layer. The objective of this part of the study was to identify the optimum magnetic structure (e.g. coercivity (H_c), exchange bias (H_{ex}) and squareness (M/M_s) and growth conditions (e.g. bias voltage and process pressure) for the multilayers. The magnetic properties of Co/Pd multilayers are controlled by the number of repeats, layer thickness, crystallographic texture, grain size and interface roughness as discussed by Barton et al, [115]. Therefore a series of samples of the Co/Pt system with similar structures were prepared in order to optimise their magnetic properties. Parameters such as the thickness of the Pt layer, the number of repetitions in the multilayer (n) and the effects of the deposition conditions have been varied.

The samples were sputtered using an Ar$^+$ pressure of 1.86mTorr. This process pressure is that used in our research group. A set of six samples were sputtered with various bias voltages in order to vary the grain size and hence optimise the coercivity of the multilayer system. The sample structures were: Ta(5)/Ru(5)/[Co(0.6)/Pt(1.6)]$_5$/Ta(5) as shown in Figure 5.1. The sputtering rate of the 5nm Ta was 0.5Å/s. This layer was used to create an amorphous surface to suppress crystal habit from the Si or SiO$_2$ of the substrate. Ru was chosen as a seed layer material due to it having a crystallographic structure similar to that of Co. 5 repeat units of Co/Pt were used as a similar number of stacks was used in previous studies, [113]. The samples were then capped with 5nm of Ta to prevent oxidation.
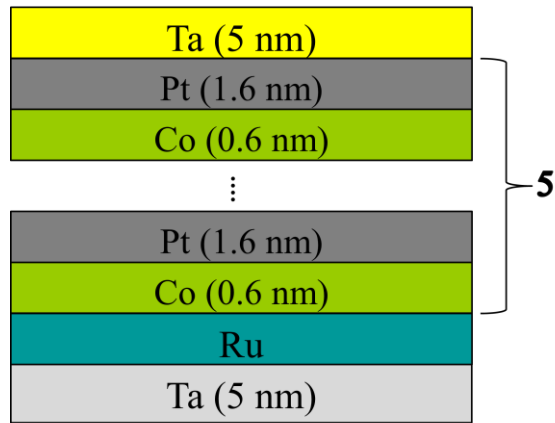
Figure 5.1 Schematic diagram of Co/Pt multilayer structure.

Magnetic measurements were made in the perpendicular direction using a VSM to examine the coercivity as a function of the number of the Co/Pt repeats. The coercivity was measured as a function of the bias voltage used to grow the samples as shown in Figure 5.2. The highest coercivity of H_c = (320 ± 5)Oe was measured for a sample grown using a 300V bias voltage. There are no review papers which explained how the bias voltage and hence the growth rate affects the coercivity of Co/Pt multilayers. However the suggestion is that the roughness between the Co and Pt layers were minimised at 300V which generates a small grain size. Hence it induced the highest coercivity in the perpendicular orientation.
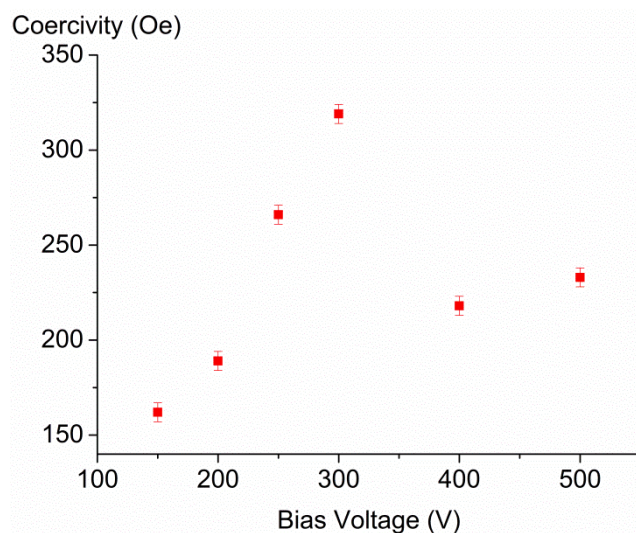
Figure 5.2 Coercivty of (Co/Pt)₅ samples as a function of the bias voltage.

After the optimisation of the bias voltage for this system, the next step of the study was to optimise the coercivity as a function of the number of repeat units (n). A set of six samples were sputtered using a 300V bias voltage with different numbers of repeat units. The sputtering conditions were identical to those used for the previous set of samples. Hysteresis loops were measured using an AGFM at room temperature. Figure 5.3 shows the coercivity as a function of n. The highest coercivity was measured with 5 repeats of Co/Pt with a value of $H_c = (320 \pm 5)$Oe. A previous study on perpendicular exchange bias using a Co/Pt multilayer system was reported by Maat et al. [113], who obtained a coercivity of about 500Oe at room temperature using five repeat units of Co/Pt.
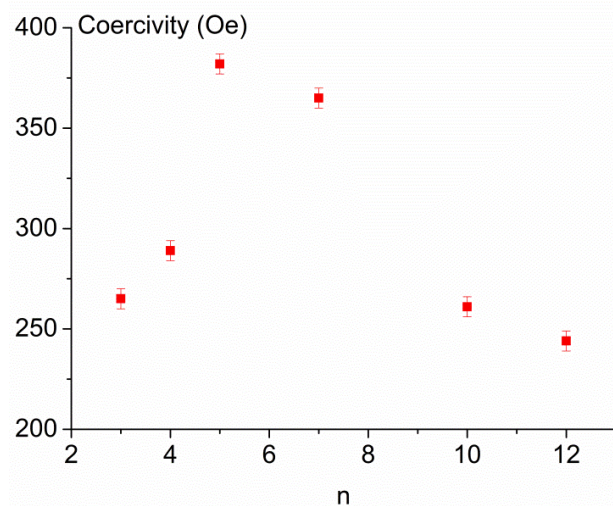
Figure 5.3 Coercivity as a function of n.

The thickness of the Pt layers was also optimised in the range 1.2 - 2.0nm which is approximately 3 to 5 atoms thick. An amorphous Ta layer and Ru seed layer were again used to induce perpendicular anisotropy. The Co/Pt multilayers were sputtered using 300V bias voltage which had been shown to generate the maximum coercivity in the films. The number of repeats (n = 5) remained unchanged. The samples were then capped with a 5nm Ta layer to prevent oxidation. The magnetic properties of the samples were measured using the AGFM at room temperature.
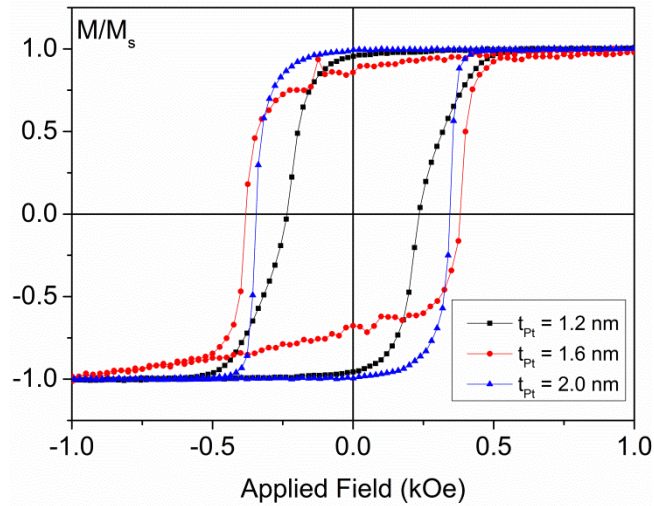
Figure 5.4 Hysteresis loop measurements for different thickness of the Pt layer.

The highest coercivity of (382 ± 5)Oe was obtained using a 1.6 nm thick Pt layer as shown in Figure 5.4. There are few Co/Pt multilayer studies on tuning the thickness of Pt layer, [116]. The Pt thickness used in the studies was 1.6nm in each case because this thickness gave the highest value of coercivity. The squareness of 1 was measured using a Pt layer thickness of 2.0nm. However the squareness reduced to 0.78 using 1.6nm of Pt. The objective of this optimisation was to maximise the coercivity of the thin film samples. This could be due to this thickness of Pt layer gives the smoothest surface between each layer. Therefore the thickness of 1.6nm of Pt was used for the rest of the experiments.

The reversal mechanism in these layers is domain wall pinning because of the exchange coupling. As can be seen in Figure 5.4 the squareness of the hysteresis loop is usually 1. This arises because of the exchange coupling between the layers of Co across the grain boundary. Therefore it is a form of intergranular RKKY coupling. Hence reversal proceeds via the initial nucleation of one or more domains followed by fairly rapid domain wall motion throughout the sample impeded by domain wall pinning.

As domain wall pinning is generally an unpredictable process most of the pinning will be due to interfacial roughness and perhaps weak pinning at grain boundary. The main factor affecting the reversal and hence the coercivity is the nucleation of the reverse domains which to some degree will be controlled by the anisotropy of

the film. However the nucleation of the reverse domains will be affected by other factors such as defects in the film. The nucleation is not uniform because the hysteresis loops shown in Figure 5.4 are rounded. The general trend is that the domain wall pinning increases with the thickness of the Pt layer up to a limit of 1.6nm.

5.2 Role of Seed layers

A seed layer was deposited under the AF layer as shown in Figure 5.5. Seed layers play an important role by inducing the desired crystallographic texture or anisotropy orientation in exchange bias samples, [8]. The induced texture of the AF or F layer is usually dependant on the crystal structure and lattice matching of the IrMn to the seed layer.
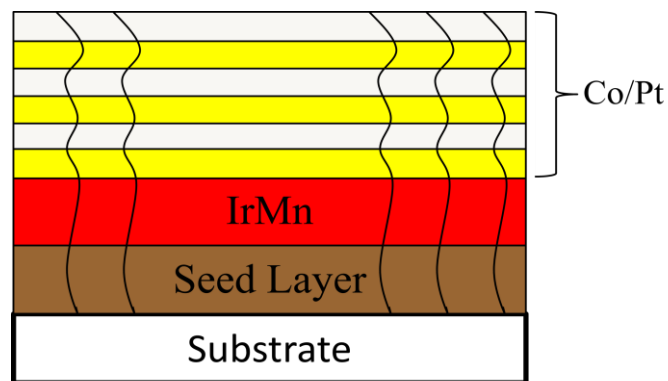
Figure 5.5 Schematic diagram of a multilayer sample structure.

Four different materials with different crystal structures have been used to optimise the magnetic properties of the Co/Pt multilayer system. The sample structures were: Ta(5)/seed(5)/[Co(0.6)/Pt(1.6)]$_5$/Ta(5). The chosen seed layers were Cu, NiCr, Pt and Ru. Cu, NiCr and Ru are the most commonly used seed layers for the growth of IrMn used previously in our research group. This was because the lattice mismatches between the (111) to IrMn(111) are below 6.0% as shown in Table 5.1.

Material	Structure	Lattice Constant		d(111)	d(0001)	Mismatch to IrMn (%)
		a (Å)	c (Å)			
IrMn	fcc	3.78	-	2.67	-	0
Ru	hcp	2.70	4.67	-	2.70	1.2
NiCr	fcc	3.56	-	2.52	-	5.6
Cu	fcc	3.61	-	2.56	-	4.4
Pt	fcc	3.92	-	2.77	-	3.6

Table 5.1 Seed layer lattice constants and the mismatch to IrMn, [117].

The induced in-plane texture for IrMn grown on different seed layers was evaluated by Aley et al. and is shown in Figure 5.6, [8]. In a grazing incident scan the absence of the peak indicates the corresponding plane is orientated parallel to the sample surface. Hence for the samples grown using Cu and Ru seed layers an IrMn (111) peak was measured which indicated that a poor in-plane (111) texture was induced. For the NiCr seed layer sample the IrMn (111) peak was not observed. This implies that the IrMn (111) planes are strongly textured along the substrate surface.
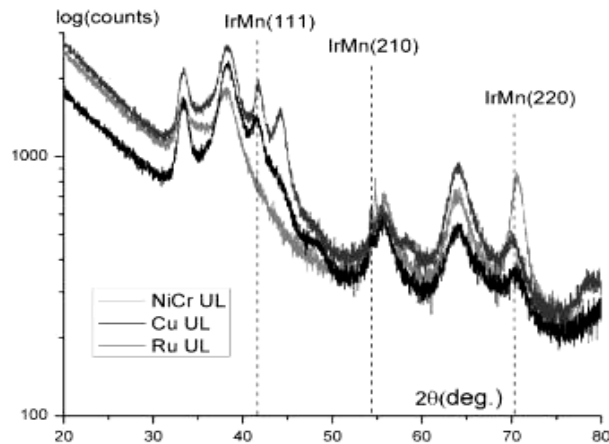
Figure 5.6 Grazing incident scans for samples grown on different seed layers, [8].

All samples were sputtered using 1.86mTorr process pressure and 300V bias voltage. An amorphous Ta layer was sputtered on top of the Si substrate to suppress crystal habit from the Si or SiO_2. The seed layer was then sputtered on top of the Ta followed by 0.6nm of Co and 1.6nm Pt multilayer structure. Five repeat units of the Co/Pt multilayer was used. This 2-ion thick Co layer exhibits a strong perpendicular anisotropy. This is because the strong interfacial anisotropy for

thickness values ≲ 10Å, [113]. The samples were capped with 5 nm of Ta to prevent oxidation.

Room temperature magnetic measurements were undertaken for all samples in the perpendicular orientation using the AGFM as shown in Figure 5.7. Table 5.2 shows a summary of the data for samples grown on different seed layers i.e. coercivity and squareness. The data shows that Ru, Pt and NiCr seed layer based systems were able to induce a perpendicular anisotropy in the Co/Pt multilayers with a coercivity of about H_c = (300 ± 5)Oe. However the Cu seed layer gave a sample with a much lower coercivity as shown in Figure 5.7. This is because the Cu seed layer does not induce an (111) texture parallel to the plane. This leads to a basal plane mis-match between the Cu seed layer and Co/Pt multilayer and resulted in poor out-of-plane anisotropy in the sample.
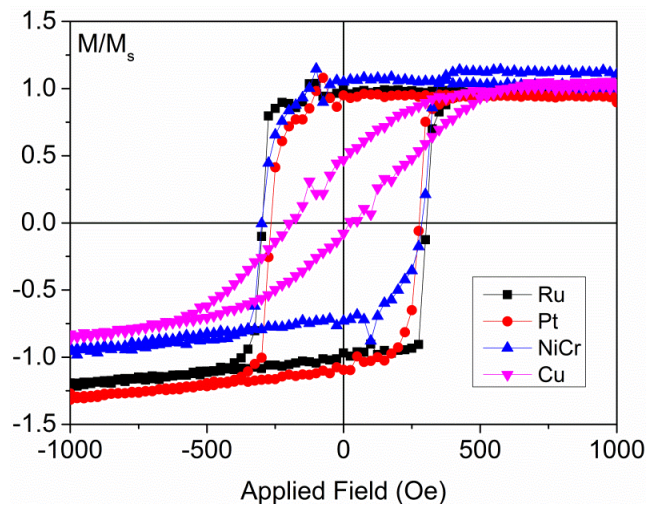
Figure 5.7 Room temperature hysteresis loops using different seed layers.

Ru has an hcp crystal structure and has been reported to induce a perpendicular anisotropy of up to 1.2 x 10^7ergs/cm³ in the Co/Pt multilayer system, [118]. Pt, NiCr and Cu have an fcc structure as shown in Table 5.1. NiCr induces a (111) texture in the IrMn parallel to the plane as shown in Figure 5.6, [8]. Cu does not texture the (111) texture parallel to the substrate and therefore the squareness and coercivity are lower than for the other samples.

Seed Layer	H_c (± 5Oe)	M/M_s (±0.02)
Ru	301	1.00
Pt	301	1.00
NiCr	295	1.00
Cu	117	0.28

Table 5.2 Summary of magnetic measurements at room temperature.

Another set of experiments was undertaken to examine the exchange coupling effect between the IrMn (111) and Co/Pt multilayers. Three samples were sputtered using three different seed layers of NiCr, Ru and Cu. The sample structures were: Ta(5)/NiCr(5),Ru(5),Cu(5)/IrMn(10)/[Co(0.6)/Pt(1.6)]$_5$/Ta(5) as shown in Figure 5.8. The seed layer and IrMn thicknesses were chosen based on the previous studies. NiCr, Ru and Cu seed layers were used to induce different IrMn texture and hence anisotropy constants reported as K_{AF} = (3.3 ± 0.4)x10^7, (0.94 ± 0.06)x10^7 and (0.28 ± 0.02)x10^7 ergs/cm^3, respectively for identical structures. These in-plane measurements were measured using the York Protocols, [8] [59]. All layers were sputtered using 1.86mTorr process pressure and 300V bias voltage. A 5nm amorphous Ta layer was sputtered on top of the Si substrate with a sputtering rate of 0.7Å/s. Repeats of five Co/Pt multilayers were then sputtered on top of the AF layer to induce the perpendicular anisotropy. The samples were then capped with a 5nm thick Ta layer to avoid oxidation.
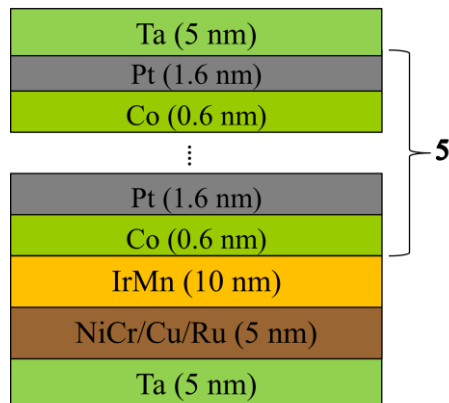
Figure 5.8 Schematic diagram of Co/Pt multilayer structure with different seed layers.

Rotational magnetic measurements were undertaken using a Model 10 Microsense VSM in order to examine the effect of the texture of the IrMn layer on the resulting exchange bias. The samples were initially set at 498K in an applied field of 20kOe

for 90 minutes perpendicular to the plane and at angles down to the in-plane direction in steps of 10°. The hysteresis loop was then measured at the setting angle.

Figure 5.9a shows one of the 70° hysteresis loop measurement and Figure 5.9b. shows the exchange bias as a function of measurement angle. The highest exchange bias was expected to occur at 70°. This is because for the (111) planes in plane, there is another set of (111) planes at 70.2°. The NiCr seed layer induced a perfect in plane 2-D texture for the IrMn (111). Therefore no exchange bias was observed at high angles. This AF layer caused only a very weak exchange bias at low angles. The highest exchange bias was measured at 0° of (18 ± 5)Oe.

The Ru seed layer induced a weaker IrMn (111) in-plane texture, [8]. Hence a maxiumum exchange bias of about (72 ± 5)Oe was observed using setting angles of up to 90°. The Cu seed layer based sample gives a random 3-D texture to the IrMn (111) [8], yet the highest value of exchange bias was measured at 70° of H_{ex} = (136 ± 5)Oe. The exchange bias then gradually decreased to a minimum value of H_{ex} = (112 ± 5)Oe at 30°.
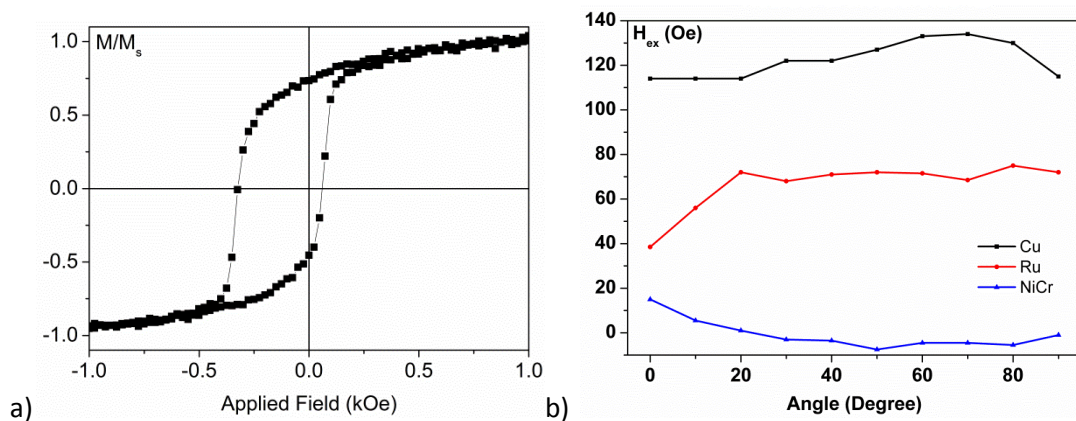
Figure 5.9 a) 70° hysteresis loop measurement of a Cu seed layer based sample. b) Exchange bias as a function of angle.

5.3. Physical Properties

The grain size distribution of the thin films was measured using a JEOL 2011 TEM. Bright field images were used to obtain the grain size distribution. A Zeiss particle size analyser was used to measure the grain size distribution of the thin film

samples. As the grains do not have a perfect circular shape the acquired grain size is that of a circle of equivalent area to the grain. The measurements are data logged from which a lognormal distribution of the grain diameters $f(D)dD$ was then calculated as discussed in Section 4.3.4.

Bright field TEM images were taken at x80k magnification with typical examples shown in Figure 5.10b and 5.11b. More than 15 images were taken from three different areas of the grid and 500 particles were counted to ensure good statistics. The lognormal distribution of the grain size diameter $f(D)$ was plotted as a function of grain diameter as shown in Figure 5.10a and 5.11a. The median grain size of the samples grown on Ru and Cu seed layers were D_m = (7.0 ± 0.2)nm and (8.6 ± 0.2)nm, respectively.

A similar experiment was reported by Barton et al. [115] on Co/Pd multilayers with perpendicular magnetic anisotropy. The samples described in this study were sputtered using a HiTUS plasma sputtering system. Co/Pd multilayers grown on Pd, with 8 repeats were used to create the required anisotropy. About 400 grains were counted and a median grain diameter of $D_m \approx$ 6nm was measured which is similar to the values reported in this work particularly as a Gaussian distribution was used.
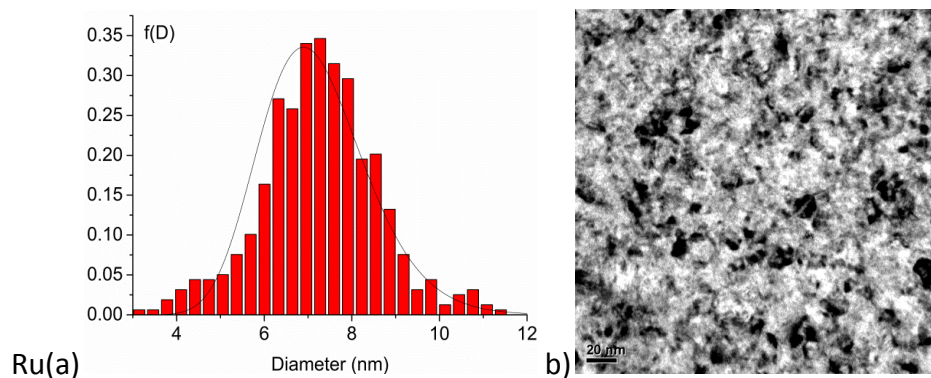
Figure 5.10 a) Ru seed layer grain size. (b) Bright field TEM image.

Cu(a)

b)
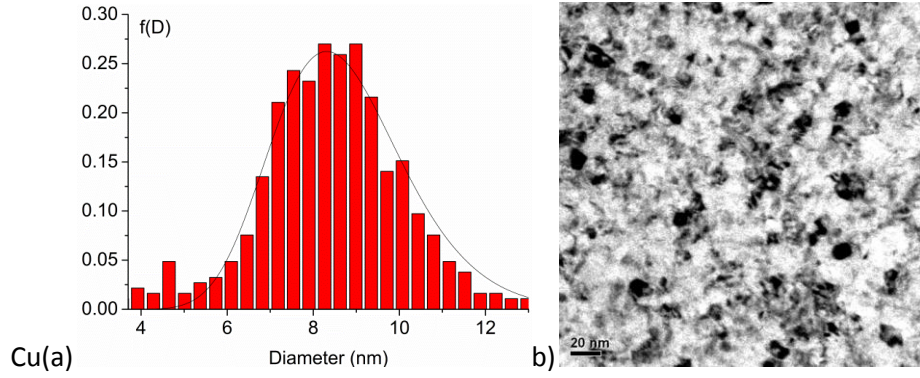
Figure 5.11 a) Cu seed layer grain size. b) Bright field TEM image.

Grain size analysis was undertaken for the other two set of samples. The TEM images were taken using x100k magnification.

Seed Layer	n	D_m (±0.2nm)	σ (±0.02)
Ru	3	7.0	0.23
	5	7.2	0.21
	10	7.3	0.24
Cu	3	8.6	0.27
	5	9.3	0.25
	10	9.1	0.25

Table 5.3 Summary of the measured grain size distribution.

The summary of the grain size analysis is shown in Table 5.3. The median grain diameter of $D_m \approx (7.2 \pm 0.2)$nm with a standard division σ of (0.21 ± 0.02) was measured for the sample grown on a Ru seed layer. Cu seed layer based samples has a larger $D_m = (9.3 \pm 0.2)$nm with a value of $\sigma = (0.25 \pm 0.02)$. The D_m of Cu seed layer is approximately 2nm larger than Ru seed layer. This is because the Cu has a sputtering rate of 1.4Å/s which is much faster than the sputtering rate of Ru of 0.4Å/s. D_m is proportional to the cube root of the sputtering rate as discussed in Section 4.1.1, [70].

It is important to note that the grain volume V_m is proportional to $D_m{}^3$. Therefore the actual grain volume of the Ru and Cu seed layer based sample are $\frac{7^3\pi}{6}$=180nm^3 and $\frac{9^3\pi}{6}$=382nm^3, respectively. Although the grain size difference between these samples was only 2nm. The grain volume of the thin film samples was increased by more than a factor of two.

There was no significant difference in the value of D_m generated using different numbers of repeats of Co/Pt. However an obvious increase in D_m of approximately 2nm was observed when the Ru seed layer was replaced by Cu. Therefore D_m is dependent upon the chosen seed layer material and it also affects the grain size distribution on the subsequent layers in the thin film samples. This is due to the polycrystalline samples sputtered using the HiTUS system exhibiting strong columnar growth, [119].

5.4 Structural Properties

IrMn is an fcc material. If the (111) planes lie perfectly in-plane, there are other (111) planes at about 72°. XRD studies were carried out to study the texture of IrMn using various seed layer materials such as NiCr, Ru and Cu. In-plane pole figure scans were measured for the sample structures as shown in Figure 5.12 to examine the texture of the other IrMn (111) planes.

| Ta (5 nm) |
| IrMn (10 nm) |
| Seed Layer (5 nm) |
| Ta (5 nm) |
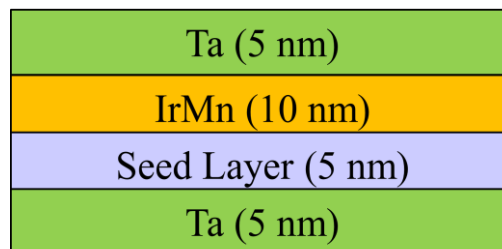
Figure 5.12. Sample structures used to determine the IrMn texture.

The selected seed layer materials were NiCr, Ru and Cu. The thicknesses and sputtering conditions were identical to those for the samples discussed in Section 5.2.

A pole figure scan around the IrMn (111) peak was carried out to examine the other possible IrMn (111) peaks as shown in Figure 5.13a, b and c. The normalised intensity was plotted against the surface normal angle α_r and shown in Figure 5.14.

The $\vartheta - 2\vartheta$ and pole figure scans indicated that NiCr and Ru induced a very strong texture of IrMn (111) parallel to the plane. However the centre spot of the scan for the Cu seed layer based sample has a very weak intensity. The results for the

texture induced in the IrMn coincided with the work of Aley et al. [8] who reported that a NiCr seed give a strong in plane (111) texture to the IrMn but a Cu seed did not.
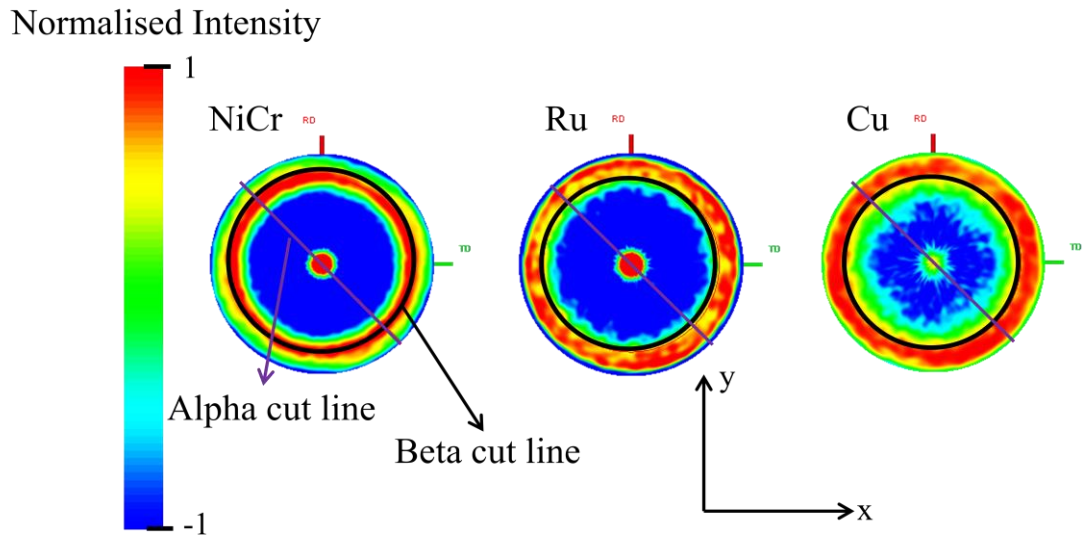
Figure 5.13 a,b,c Pole figure measurements of IrMn (111) plane for samples grown on different seed layers.
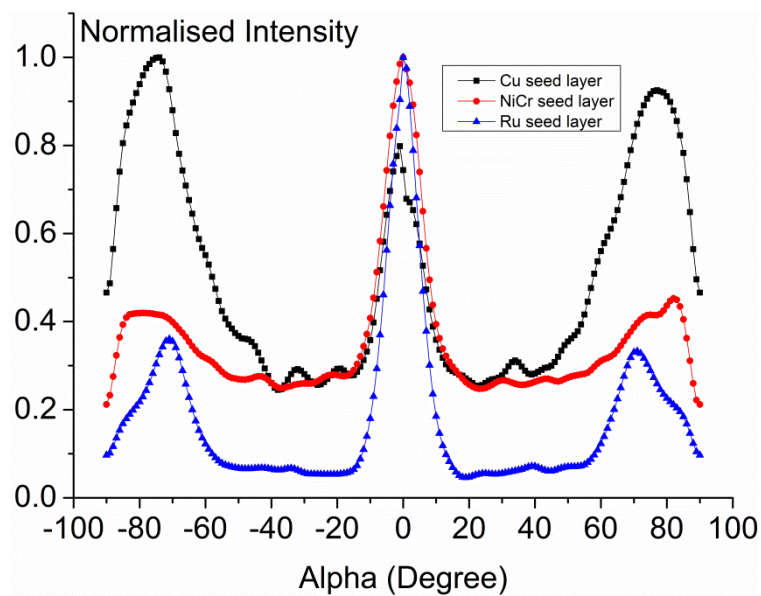
Figure 5.14. Pole figure measurements for the IrMn (111) plane.

Figure 5.14 shows the normalised intensity as a function of α_r. As can be seen from the Figure 5.14 the second IrMn (111) peak was observed at around 70° for all samples. For the case of the IrMn grown on a NiCr seed layer the IrMn (111) peak

at 72° is well textured with a FWHM of (13 ± 1)°. For the Ru and Cu based systems the peak is more diffuse therefore a larger FWHM was measured of (17 ± 1)° and (20 ± 1)°, respectively as shown in Table 5.4.

Seed layer	FWHM of IrMn (111) Degree (±1°)
Cu	13
NiCr	20
Ru	17

Table 5.4 FWHM of the 2nd IrMn (111) with different seed layer materials.

The other feature that can be noticed from Figure 5.14 is the normalised intensity of the peak at 70°. NiCr seed gives the best IrMn (111) in-plane texture however it resulted the lowest intensity of the 2nd IrMn (111) peak at 70°. Although the Cu seed induced a broader peak at 70° the peak intensity is more than three times higher than the NiCr and Ru seeds. This is because the Cu seed layer induced a random texture to the IrMn and leads to some natural growth of the (111) planes at 70°. This also explains why the intensity of the Cu seed layer based peak at 70° is higher than that at 0°.

The XRD pole figure measurements clearly show the difference of the IrMn (111) in-plane texture which was induced by various seed layer materials. It also showed that the alternative IrMn (111) plane exists at about 70° perpendicular to the plane. Therefore the Co/Pt multilayers should be able to couple with the IrMn (111) plane at 70°. Based on the magnetic measurements discussed in Section 5.2, the highest exchange bias of H_{ex} = (136 ± 5)Oe was measured using a Cu seed layer at 70° perpendicular to the plane. This indicates that the XRD measurements are in agreement with the magnetic measurements and confirm the importance of texture.

5.5 Effect of an AF layer on Co/Pt Multilayers.

An AF layer was inserted into the optimised Co/Pt multilayer system in an attempt to generate exchange bias in the perpendicular orientation. A similar study was reported by Maat et al., [113], whose hysteresis loops were measured at 10K and

exhibited an exchange bias H_{ex} = 1.2kOe after a field setting process. Five repeat units of Co/Pt multilayers were used with thicknesses of 0.4nm of Co and 0.5nm of Pt. A 1.5nm CoO layer was deposited above the multilayer to form a top bias system. Another similar experiment was reported by Dijken et al. [120] an exchange bias value of $H_{ex} \approx$ 80Oe was measured using a bottom bias system. The sample composition was SiO$_2$/Pt(2)/IrMn(10)/[Co(0.4)/Pt(2)]$_3$. The sample was set for 60 minutes in a field of 5.5T at 493K in the out-of-plane orientation.

Samples with bottom exchange bias were studied with structure: Ta(5)/Ru(5) or Cu(5)/IrMn(6)/[Co(0.6)/Pt(1.6)]$_5$/Ta(5) as shown in Figure 5.15. Sputtering conditions were 300V bias voltage with an Ar pressure of 1.86mTorr were used based on the optimisation study described in Section 5.1. 5nm Ru and Cu seed layers were deposited to induce different textures in the 10 nm IrMn layer as shown in Section 5.4. (Co/Pt) multilayers were used with 0.6nm and 1.6nm thick Co and Pt multilayers, respectively. The samples were capped with 5nm of Ta. These samples were used to measure the median blocking temperature $< T_B >$ and the anisotropy constant K_{AF} in the IrMn
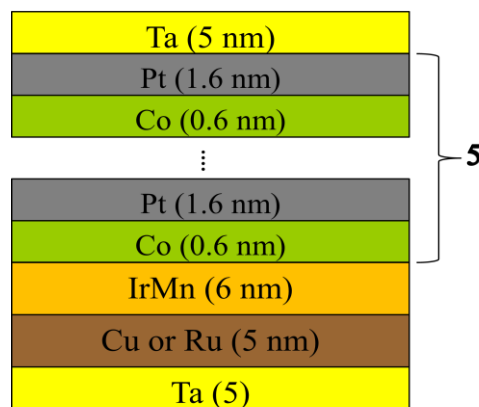
Figure 5.15 Schematic diagram of the Co/Pt multilayer structure.

The interfacial anisotropy of a sample with a 0.3 - 0.5nm Co layers in a Co/Pt multilayer is approximately 0.27ergs/cm^2, [121]. The number of repeat bilayers n = 3, 5 and 10 were used to control the coercivity of the samples.

The median blocking temperature $< T_B >$ is defined as the activation temperature at which the exchange bias goes to zero, [59]. Since the samples were grown using

a sputtering system the samples have a polycrystalline structure and therefore each grain has its own value of $< T_B >$ hence the AF can be characterised by a distribution of $< T_B >$. It is possible to control the activation and reversal of the AF grains to vary the exchange bias. This process can be achieved by heating with the F layer reversed in order to change the order of the AF from the original state as discussed in Section 3.7.

Blocking temperature measurements were undertaken for all samples using the York Protocols, [59]. Figure 5.16 shows the blocking temperature curves that were measured for the samples with Ru seed layers for different number of Co/Pt repeats. Each sample was initially set for 60 minutes in an applied field of +10kOe at 498K which saturated the Co/Pt stack. All hysteresis loops were measured at 298K where the samples were thermally stable. From Figure 5.16 it is clear that 3 repeats produces the highest value of H_{ex} and is thermally stable.
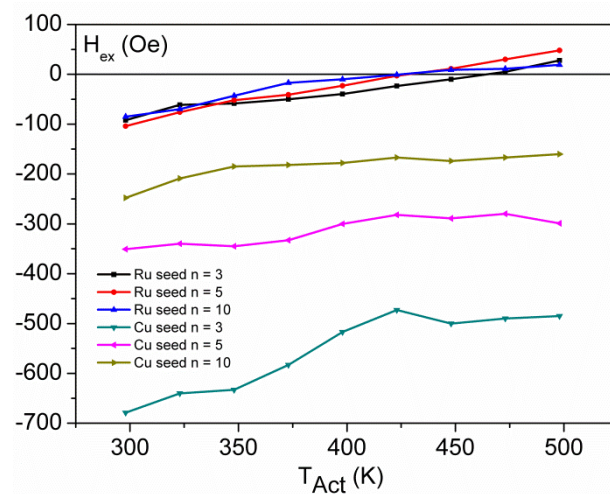
Figure 5.16 Blocking temperature measurements of Ru and Cu seed layer based samples.

The data in Table 5.5 shows a summary of the values of $< T_B >$ and H_{ex} for all samples. A number of unexpected features were observed in these measurements. The first of these is that the texture of the IrMn strongly influences the coupling. It is known from previous work that the Ta/Ru seed layer induces good (111) texture in the IrMn as discussed in Section 5.4, [8]. The Cu seed layer induces random (111) texture which will have a larger fraction of the (111) planes lying out of the plane of the film. This clearly increases the coupling and hence H_{ex} increases by up to an

order of magnitude. However increasing the perpendicular anisotropy of the $(Co/Pt)_n$ by using the optimum number of five repeats reduces the value of H_{ex} to (355 ± 5)Oe indicating that the shift in the loop comes from the texture of the IrMn layer.

Seed Layer	n	H_{ex} (±5Oe)	$<T_B>$ (±2K)	K_{AF} (10^7ergs/cc)	D_m (±0.2nm)
Ta/Ru	3	92	465	1.00 ± 0.05	7.0
	5	104	431	0.86 ± 0.04	7.2
	10	85	425	0.81 ± 0.04	7.3
Cu	3	688	>500	>0.55 ± 0.03	8.6
	5	355	>500	>0.46 ± 0.02	9.3
	10	25	>500	>0.49 ± 0.02	9.1

Table 5.5 Summary of blocking temperatures and exchange bias (H_{ex}) for all samples.

The value of $<T_B>$ can also be explained by the competing anisotropies of the Co/Pt multilayers and IrMn. The in-plane anisotropy induced in the IrMn grown on Ru is much greater than that due to the Co/Pt multilayers. Therefore the exchange coupling effect is dominated by the in-plane anisotropy of the IrMn. For the case of the sample grown on a Ru seed layer with n = 3 the perpendicular anisotropy is much lower than that for the sample with n = 10.

A further unexpected feature of the results is the effect of the $(Co/Pt)_n$ multilayer on the median blocking temperature. Previous data for in-plane F layers with identical seed layers and an IrMn thickness of 10nm gave the values of $<T_B>$ of 386K for the Ta/Ru seed layer based film and 367K for the Cu seed layer based film, [59]. It is important to note that $<T_B>$ is due to the product of $K_{AF}V_m$ where V_m is the grain volume which is given by $D_m{}^3\pi/6$. Although the median grain size diameter of Cu seed layer based system was approximately 2nm larger than the Ru seed layer based system. The actual grain volume of Cu seed layer based sample was twice that of the system grown on Ru. (i.e. $9^3 = 729$, $7^3 = 343$)

For the Cu seed layer based system the value of $<T_B>$ was greater than 500K and could not be measured due to the resulting damage to the film structure. In the case of an in-plane system which was studied by Aley et al. [8] a Cu seed layer based induced a $<T_B>$ of 347K and a K_{AF} of (0.28 ± 0.02)x10^7ergs/cc. However in

Table 5.5 it showed that the $< T_B >$ of Cu seed layer based system is greater than 500K.

Because $< T_B >$ is greater than 500K therefore a minimum value of K_{AF} for the Cu seed layer based samples was calculated using $< T_B >$ = 500K. The median grain diameter of the samples varied between 8.8nm to 9.3nm and no trend was observed with the grain size. This is because the samples were sputtered using the same bias voltage. The highest K_{AF} of (0.55 ± 0.03) x 10^7ergs/cc was measured using three repeat units of Co/Pt. This value of K_{AF} is more than twice that measured by Aley et al. [8] for an in-plane system grown on Cu of (0.20 ± 0.02) x 10^7ergs/cc.

In the previous study of Aley et al. [8] 10nm thick IrMn layers were used to couple to 3nm of CoFe. The blocking temperature measurements showed that the AF grains were unstable at room temperature. After the CoFe layer was replaced by Co/Pt mulitlayers the stability of the AF grains was increased dramatically which is shown by the blocking temperature curve in Figure 5.16. The Cu seed layer induces random magnetocrystalline anisotropy in the IrMn which causes some of the Mn spins to align with the F layer anisotropy. Therefore the thermal stability of the IrMn was improved by the Co/Pt multilayer system.

The effect of increasing the perpendicular anisotropy of Co/Pt multilayers leads to a reduction of the AF anisotropy. However even for the sample with n = 5 grown on the Cu seed layer the value of $< T_B >$ remained in excess of 500K. For the sample with n = 3 grown on a Cu seed a value of H_{ex} = (688 ± 5)Oe was found which is well within the range required for device applications. The values of exchange bias found in this experiment can be explained by the competing anisotropies of the IrMn and Co/Pt multilayers as shown in Figure 5.17.
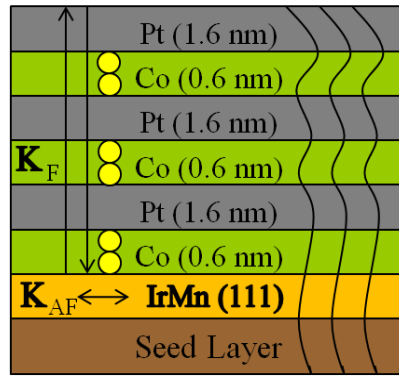
Figure 5.17 Schematic of competing anisotropy between a Co/Pt multilayer and IrMn.

NiCr seed layer

NiCr induced a strong IrMn (111) in-plane texture where the planes lie parallel to the substrate surface as shown schematically in Figure 5.18. This was confirmed in the previous work reported by Aley et al. [8] and the pole figure for samples made in this work which were shown in Section 5.4. The Co/Pt multilayer induced a perpendicular anisotropy confirmed by the magnetic measurements shown in Section 5.2. Since the anisotropy orientation between the IrMn and Co/Pt multilayers is perpendicular. No exchange bias at all was measured.
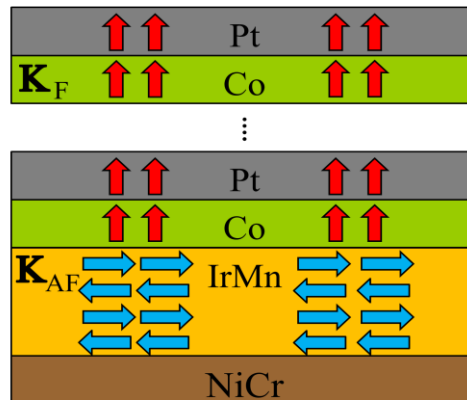
Figure 5.18 Anisotropy orientation between IrMn and $(Co/Pt)_n$ for a sample grown on a NiCr seed layer.

Ru seed layer

The Ru seed layer induces a weaker anisotropy mis-alignment of the IrMn (111) as shown schematically Figure 5.19a. This was again confirmed by the pole figure data shown in Section 5.4 and the room temperature hysteresis loop measurements

shown in Figure 5.19b. The hysteresis loops were measured at room temperature after the usual field setting process. Exchange bias values of H_{ex} = (92 ± 5)Oe, (104 ± 5)Oe and (85 ± 5)Oe were measured using different repeat units of n = 3, 5 and 10, respectively. This indicated that the weaker mis-alignment to the IrMn (111) allowed the Co/Pt multilayers to exchange couple with the IrMn in the perpendicular direction.
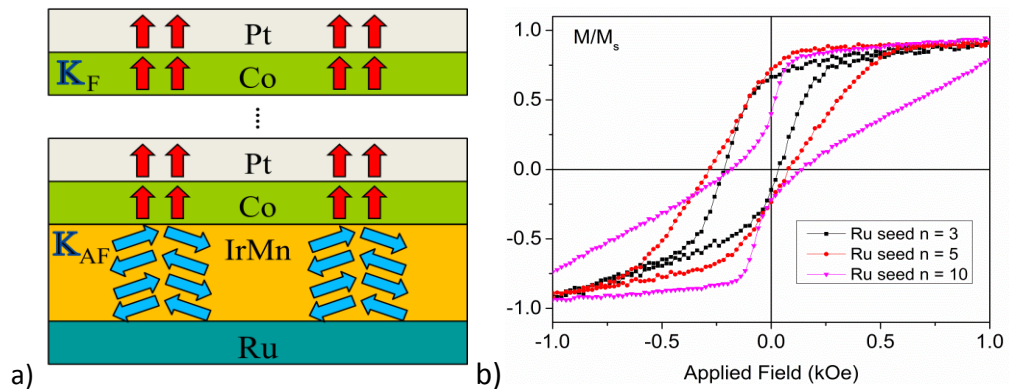
Figure 5.19a) Anisotropy orientation between IrMn and (Co/Pt)$_n$ using a NiCr seed. b) Room temperature hysteresis loops with different repeat units of the Co/Pt multilayer.

Cu seed layer

In the case of the Cu seed layer based samples a random orientation of the IrMn (111) planes resulted, as shown by the pole figure data in Section 5.4. The anisotropy orientation between the IrMn and Co/Pt multilayers is shown schematically in Figure 5.20a. The hysteresis loops were measured at room temperature after the usual field setting process. Exchange bias values of H_{ex}= (688 ± 5)Oe, (355 ± 5)Oe and (180 ± 5)Oe were measured for repeat units of n = 3, 5 and 10, respectively. This is because the random orientated IrMn (111) planes allows for stronger coupling with the Co/Pt anisotropy.
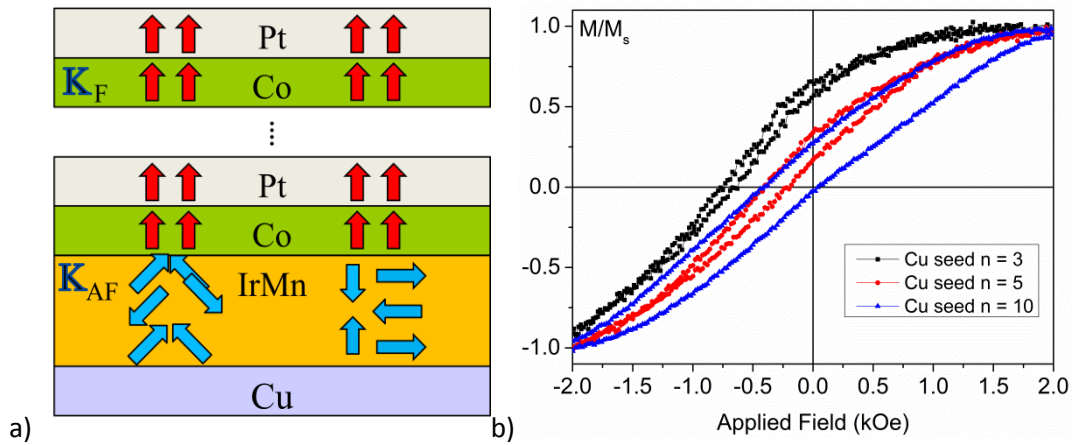
Figure 5.20a) Anisotropy orientation between IrMn and (Co/Pt)$_n$ using a Cu seed. b) Room temperature hysteresis loops with different repeat units of Co/Pt.

There were two unique features which can be observed from Figure 5.19b and Figure 5.20b. There are the value of the coercivities and the positions of H_{c1} and H_{c2} of the hysteresis loops. A significant decrease of coercivity was recorded when the Ru seed layer was replaced by Cu. This was due to the absence of (111) texture in the IrMn and so the magnetocrystalline anisotropy along the IrMn <111> direction was distributed randomly in all directions.

The other feature was the values of H_{c1} and H_{c2}. In the case of the Ru seed layer system H_{c1} was located at a negative field value but not H_{c2}. However for the samples grown using a Cu seed layer the largest exchange bias of (688 ± 5)Oe was measured. Furthermore for the samples using repeat units of n = 3 and 5 the value of H_{c1} and H_{c2} were (-703 ± 5)Oe, (-586 ± 5)Oe and (-405 ± 5)Oe, (-248 ± 5)Oe, respectively. These were both located at negative field values at room temperature as shown in Figure 5.20b and hence cannot be demagnetised by an applied field. Therefore the Co/Pt multilayer has the potential to work as a HAMR media.

In the context of this project the primary objective is to create an exchange bias in HAMR media. In Figure 5.20b it is shown that for the Cu seed layer sample with 3 repeat units is feasible for HAMR media. It also provides a proof of principle that this system can work. This is because both coercivity values are in negative field values and an exchange bias value of H_{ex} = (688 ± 5)Oe was measured.

Figure 5.20b does not indicate the required activation temperature for reversal. So that reversal of a bit of information could be achieved. It is interesting to note that in an exchange bias recording medium the information is actually stored in the AF layer rather than the F layer and hence it is not subject to normal de-magnetisation processes. However in Co/Pt multilayers the grains are strongly exchange coupled and hence utilisation of this system is likely to lead to significant spreading of the bits due to the switching in adjacent regions of the AF and the resulting expanded bit size in the Co/Pt layer. Hence to produce a high density exchange bias medium a segregated F layer will still be required. It should be noted that other than very weak surface effects, there is no intergranular exchange coupling in a polycrystalline AF layer. Hence there is no necessity for exchange decoupling in the IrMn.

The magnetic measurements shown in Figure 5.20b show that it is possible to shift both coercivities to a negative value of applied field. It is based on the competing anisotropies of the IrMn layer and Co/Pt multilayers. The Co/Pt multilayer system has a continuum thin film structure which is not suitable for HAMR media. However it may have the potential to form a patterned HAMR medium. A continuous HAMR medium requires a segregated grain structure with the use of $CoCrPt-SiO_2$ which will be discussed in the next chapter.

Chapter 6

HAMR Based on Exchange Bias

This chapter summarises the important experimental results including magnetic and crystallographic characterisation of a perpendicular exchange bias thin film media sample. The magnetic measurements are based on the York Model of Exchange Bias which explains the origin of the stability and magnitude of the coupling between a ferromagnetic (F) and antiferromagnetic (AF) layers. This chapter also provides a proof of principle that a perpendicular recording medium (PRM) based on exchange bias could be achieved at room temperature. Segregated thin film samples were demonstrated using a dual Ru seed layer.

6.1 Growth Conditions

A series of measurements were made to optimise the physical and magnetic properties of the thin film samples. A segregated grain structure plays an important role in conventional perpendicular recording media. It can be achieved by sputtering a Ru seed layer at two different process pressures where the process pressure of the second layer has to be much greater than that used for the first. Under these conditions the grain size of the second layer is smaller than that in the first layer. Therefore the grain size was reduced as well as a void structure being created. The void structure provides a ~1nm wide spacing between each grain. When the $CoCrPt-SiO_2$ layer is deposited on the seed layer, the SiO_2 becomes trapped in the voids as shown in the cross-sectional TEM image in Figure 6.1. The SiO_2 acts as an insulator and provides RKKY de-coupling between the grains.
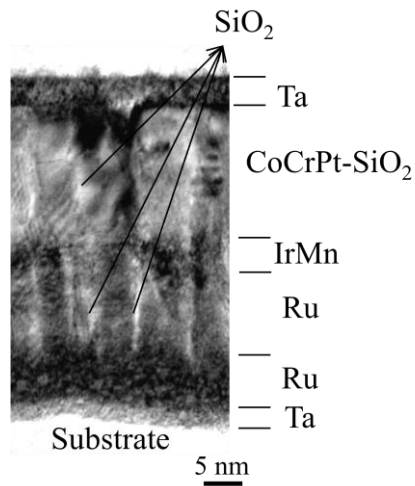
Figure 6.1 Cross section TEM image of a segregated sample.

A series of measurements were performed to optimise the segregated grain structure. Six samples were sputtered to create identical structures of Si/Ta(5)/Ru(8)/Ru(12)/CoCrPt-SiO$_2$(20)/Ta(5) as shown in Figure 6.2. However the process pressure used to grow the second Ru seed layer was varied in the range 10mTorr to 30mTorr.
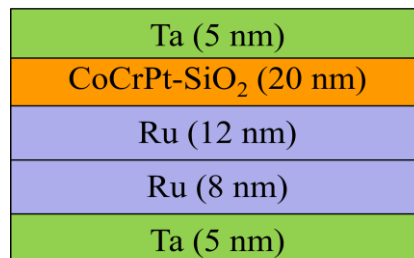
Figure 6.2 Schmatic diagram of the CoCrPt based sample structure.

5nm of Ta was grown at a sputtering rate of 0.5Å/s to create an amorphous surface to suppress crystal habit from the Si. In total 20nm of the Ru was grown as a seed layer.

A seed layer thickness of 20nm is commonly used in HAMR media and PRM, [4] [17]. A CoCrPt-SiO$_2$ layer was then sputtered on top of the seed layer using an identical process pressure to that used for the second seed layer. A recording layer thickness of 20nm was used to represent a medium providing enough signal for a read head. The samples were capped with a 5nm Ta layer to prevent oxidation.

118

Magnetic Properties

Room temperature hysteresis loop measurements were made. Because there was no AF layer in these samples, an AGFM was used to measure the magnetic properties shown in Figure 6.3. The samples were measured in the perpendicular orientation. Table 6.1 shows a summary of the magnetic properties of the samples.

Process pressure for the 2nd Ru (mTorr)	H$_c$($\pm5^{-3}$kOe)	M/M$_s$($\pm$0.02)
10	0.97	0.78
15	1.39	0.63
20	1.25	0.98
25	1.78	0.78
30	1.20	0.91
40	0.18	0.18

Table 6.1 Magnetic properties of samples with structures shown in Figure 6.2.
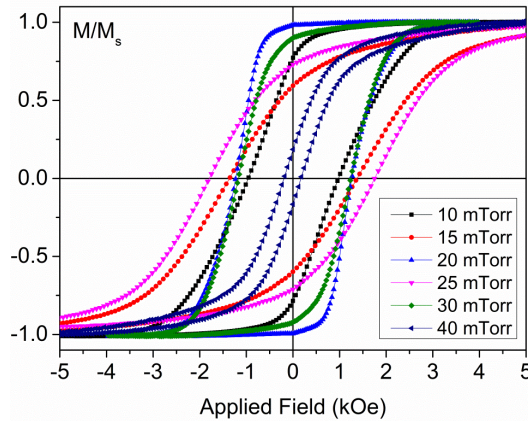
Figure 6.3 Room temperature hysteresis loop measurements for CoCrPt samples grown a different process pressures.

There are two important criteria that need to be considered in perpendicular media which are the coercivity and squareness. High coercivity is required for HAMR media because of the relationship between the magnetocrystalline anisotropy constant K_U and thermal stability. In recording media the magnetisation of a bit must be stable for 10 years. Hence thermal stability is required the criterion [12]

$$\frac{K_U V_m}{k_B T} \approx 40 \qquad (6\text{-}1)$$

119

where K_U is the magnetocrystalline anisotropy constant, V_m the grain volume, k_B Boltzmann's constant and T the temperature. As K_U is increased the grain size can be reduced and therefore a high density can be achieved. A high value of squareness is required to generate an output signal.

Using a low process pressure such as 10mTorr or 15mTorr to sputter the second Ru seed layer resulted in low squareness values of 0.78 and 0.63, respectively. This indicates that for low process pressure growth the Ru cannot induce strong perpendicular anisotropy in the CoCrPt-SiO₂ layer.

As the second Ru seed layer process pressure is increased up to 30mTorr a perpendicular anisotropy with squareness values in the range 0.78 - 0.91 and a coercivity between 1.20 to 1.78kOe are generated as shown in Table 6.1. The process pressure of the Ar plasma is approximately inversely proportional to the sputtering rate. The sputtering rate of Ru using 20, 25 and 30mTorr was 0.4Å/s, 0.3 - 0.4Å/s and 0.2Å/s, respectively. Since the deposited Ru atoms are more scattered by Ar atoms at the high process pressures the decrease of grain diameter is due to a reduction in the migration energy and the migration distance of the deposited Ru atoms as shown in Figure 6.4, [122].
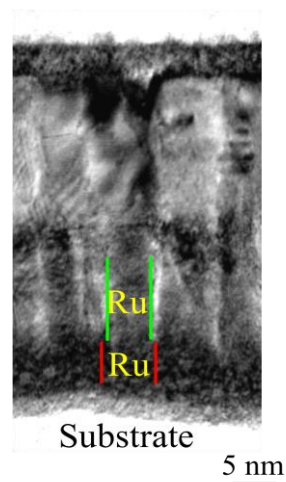
Figure 6.4 Cross sectional TEM image of a segregated sample of CoCrPt-SiO₂ system.

However the out of plane anisotropy collapses once the process pressure of the second Ru layer reaches 40mTorr. A squareness value of 0.18 was measured. This is because at 40mTorr the extremely low sputtering rate of 0.0 - 0.1Å/s resulted in

poor crystallisation of the Ru. The CoCrPt-SiO₂ layer did not have c-axis texture perpendicular to the plane leading to a low squareness.

Structural Properties

X-ray diffraction measurements were carried out on the samples for which the second Ru seed layer was sputtered using different process pressure. $\vartheta - 2\vartheta$ scans were used to measure the crystallographic texture of the samples. The direction of a X-ray diffraction can be calculated using Bragg's Law

$$\lambda = 2d \sin \vartheta \qquad \text{(6-2)}$$

where λ is X-ray wavelength, ϑ is angle between the incident beam and the crystal planes and d is the lattice spacing. Due to the crystal structure of CoCrPt-SiO₂ and Ru both being hexagonal, the lattice spacing is

$$d = \frac{1}{\sqrt{\frac{4}{3a^2}(h^2+k^2+hk)+\frac{l^2}{c^2}}} \qquad \text{(6-3)}$$

Where h, k and l are the miller indices for a particular plane and a and c are the lattice constants of the crystals as shown in Figure 6.5.
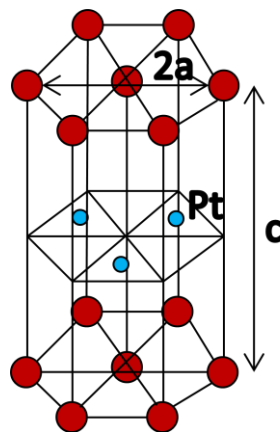
Figure 6.5 Hexagonal crystallographic structure with its lattice constants.
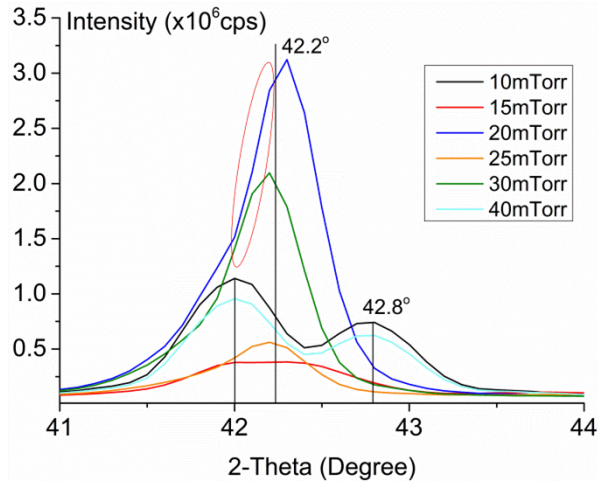
Figure 6.6 $\vartheta - 2\vartheta$ scans for samples grown using different process pressures on the second Ru seed layer.

Based on the Internation Centre for Diffraction Data (ICDD) the Ru (002) peak should be located at 42.2°. The (002) peak for the CoCrPt-SiO$_2$ is located at about 42.8°, [123]. Two peaks located at 42.0° and 42.8° can be seen in Figure 6.6. The samples were deposited using 10mTorr up to 40mTorr process pressures for the 2nd Ru seed layer. Since we are looking at the (002) peak for the Ru and CoCrPt-SiO$_2$ layer, the first term of $\sqrt{\frac{4}{3a^2}(h^2 + k^2 + hk)}$ goes to zero because h and k are both 0. Therefore the only term that contributes to the diffraction patterns is $\sqrt{\frac{l^2}{c^2}}$ which indicates that the lattice constants c are different for the Ru or CoCrPt-SiO$_2$ layers grown using various process pressures. A measurement provided by Seagate Media Research of the lattice d-spacing as a function of Pt concentration in $(Co_{87}Cr_{13})_{1-x}Pt_x$ is shown in Figure 6.7.
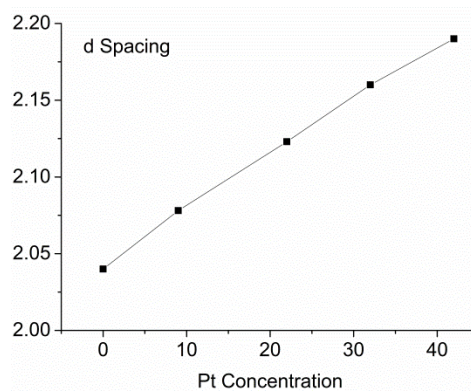
Figure 6.7 Measurement of d-spacing as a function of Pt concentration, [123].

The data in Figure 6.7 show that the d-spacing along (0002) of CoCrPt-SiO$_2$ is directly proportional to the Pt concentration and can be varied by the Pt concentration. For a CoCrPt-SiO$_2$ alloy the Pt atoms are located in the middle of the unit cell between two hexagonal rings as shown in Figure 6.8. Therefore as the Pt concentration increases it stretches the lattice constant c.
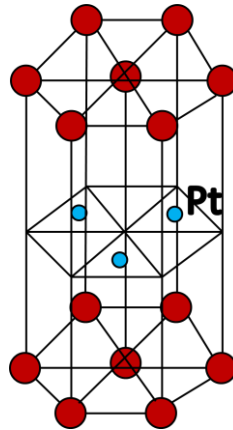
Figure 6.8 Pt atom location in CoCrPt-SiO$_2$ crystal structure.

In the case of the 2nd Ru seed layer using 15, 20, 25 and 30mTorr growth pressures the Ru and CoCrPt-SiO$_2$ peaks merge together to become a single peak. This is because of the matching of the c-axis of the CoCrPt-SiO$_2$ to that of the Ru. As the d-spacing increases the diffraction peak appears at a lower angle, eventually coming to a point where it merges with the Ru (002) peak. A small shoulder can be observed in the scans for samples grown at 20mTorr and 30mTorr as shown in Figure 6.6 circled in red. This implies that the Ru peak does not change significantly.

For the samples grown using 15mTorr and 25mTorr process pressures a broad peak at 42.2° with a FWHM of 0.73° was observed. The intensity of these peaks is relatively low with values of 5.6x10^5 and 3.8x10^{5}cps, respectively. Therefore a poor out-of-plane anisotropy resulted as shown in the magnetic measurements in Figure 6.3. In the case where the samples were grown using 20mTorr and 30mTorr process pressures the intensity of the peaks are much higher with values of 3.1x10^6 and 2.1x10^{6}cps, respectively and FWHM of 0.54° and 0.51°. This indicates that the CoCrPt-SiO$_2$ was well textured in the perpendicular direction. Hence a high value of coercivity and squareness were obtained.

Physical Structure

Samples were also grown on TEM grids for grain size analysis, [86]. Bright field TEM images were acquired using a JEOL 2011 TEM at x100k magnification. Over 500 grains were measured for each sample to ensure good statistics. The median grain diameter and the TEM images for these samples are shown in Table 6.2. The data is comparable to the grain sizes in segregated media reported in our previous work on easy axis orientation, [61]. No trends were observed for the median grain size. The grain segregation level was not complete for samples where the Ru layer was grown at low process pressures (10, 15 and 20mTorr) as shown in Table 6.2.

The key feature that can be observed from the images was that the level of grain segregation was optimised when the process pressure of the second Ru layer was 30mTorr. The separation between each grain was about 1nm. This separation level and median grain diameter of D_m = (6.2 ± 0.2)nm are similar to the HAMR media produced by Seagate Media Research, [19]. The average grain size was below 8nm in all cases with the smallest having D_m = (5.6 ± 0.2)nm for the sample which was grown on an Ru seed layer grown using a process pressure of 25mTorr.

Based on the magnetic and physical properties it was decided to fix the deposition pressure at 30mTorr for the second Ru seed layer. The main reasons for this choice are the high level of segregation between the grains and the fact that it gives the second smallest median grain size with the value of D_m = (6.2 ± 0.2)nm as shown in Table 6.2. Using a process pressure of 20mTorr induced a better squareness of 0.98, the D_m of the sample was (7.7 ± 0.2)nm which corresponds to a grain volume of $(\frac{\pi 7.7^3}{6})$ = 239nm³, whilst using a 30mTorr process pressure reduced the D_m significantly to (6.2 ± 0.2)nm with a grain volume of $(\frac{\pi 6.2^3}{6})$ = 125nm³.
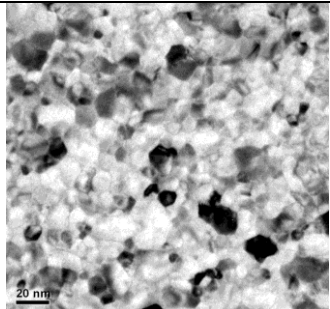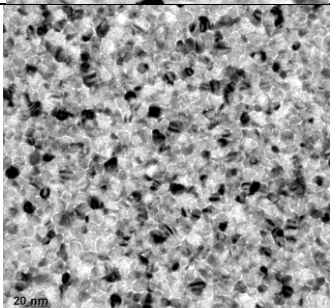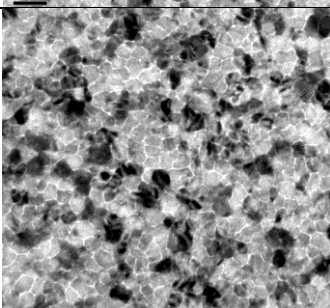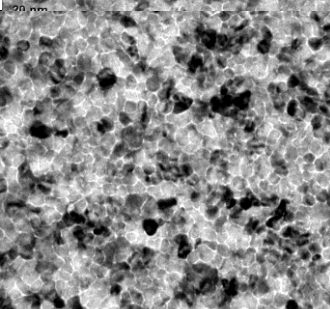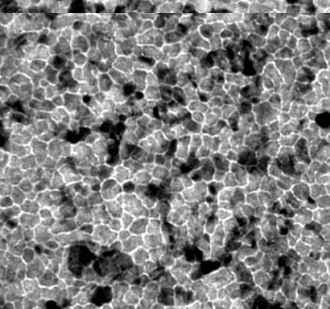
Pressure (mTorr)	TEM Image	D_m (±0.2nm)	σ (±0.02)
10		6.9	0.27
15		6.2	0.18
20		7.7	0.28
25		5.6	0.21
30		6.2	0.22

Table 6.2 Grain sizes of samples on dual Ru layers.

6.2 Seed Layers and Structural Effects

In conventional PRM two seed layer structures are used. One beneath the soft underlayer and another grows on top to promote perpendicular c-axis texture in the recording layer. This layer also serves as an exchange break layer, [17]. One of the most commonly used seed layers to promote c-axis texture is Ru. It induces a good hcp (002) texture perpendicular to the plane as discussed in Section 6.1. Another criterion for the selection of the seed layer is the c-axis dispersion. The dispersion of the recording layer influences the signal to noise ratio (SNR) of the media by broadening the switching field distribution (SFD). The thin film samples produced in this study have a columnar structure and therefore the texture of the recording layer is highly dependent on the seed layer. We have examined the use of seed layers with three different types of crystal structure; fcc, bcc and hcp.

A series of measurements were made to study the effects of a Ru seed layer since it is the seed layer material that is used in conventional PRM. The first sample was a simple structure of Ta(3)/Ru(8)/Ru(12). A process pressure of 3mTorr was used in all cases for the fast Ta layer to induce an amorphous surface and the first Ru seed layer. The second Ru seed layer was sputtered using a higher process pressure of 30mTorr to create a voided structure. These sputtering conditions were optimised as discussed in Section 6.1.

The bias voltage used for the seed layer growth was varied between 400V and 1000V in 200V steps. Figure 6.9 shows a $\vartheta - 2\vartheta$ scans for all samples. The peaks which can be observed from the $\vartheta - 2\vartheta$ scans represent the crystal plane which is orientated perpendicular to the plane. A peak was observed at 42.2° which represents Ru (002). No other Ru peaks were present in the scan indicating a well defined out of plane crystallinity. Rocking curves were measured for each sample at the (002) Ru peak to study the c-axis distribution.
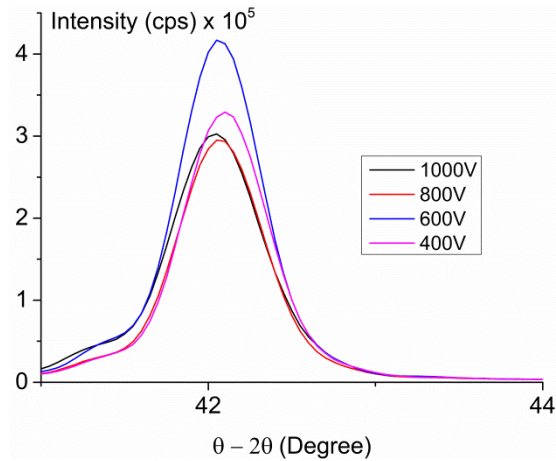
Figure 6.9 $\vartheta - 2\vartheta$ measurements for a dual Ru layer system.

The $\vartheta - 2\vartheta$ angle was set at 42.2° so that the c-axis distribution of the Ru (002) can be measured and the X-ray source and detector were then "rocked" from 10° to 30° as shown in Figure 6.10. A summary of the FWHM values for the samples grown using different bias voltages is shown in Table 6.3. The FWHM value from the rocking curves indicates the level of the distribution of the orientation of the Ru (002) axes. Because the lowest value of FWHM was measured for the sample grown using a bias voltage of 600V, this bias voltage was used for the growth of the seed layers in all subsequent experiments.
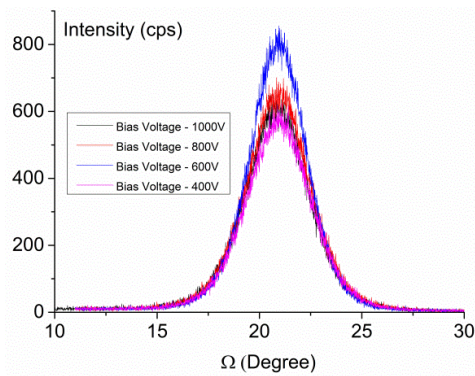
Figure 6.10 Rocking curve measurements for the dual Ru layer system.

The easy axis distribution of the CoCrPt can be measured in an alternative way via magnetic rotational measurements. Chureemart et al. [61] measured the crystal orientation dispersion of different types of recording media such as granular, ECC, ECC/CGC using magneto-optical kerr effect (MOKE). The easy axis dispersion of these media was 8.60°, 7.13° and 4.70°, respectively, [61]. This indicated that the

127

quality of the samples which were grown using HiTUS system were of a similar standard to commercial recording media.

Bias Voltage (V)	FWHM (± 0.1 Degree)
400	3.7
600	3.5
800	3.7
1000	3.8

Table 6.3 FWHM measurements for the Ru seed layer (002) peak for samples grown at different bias voltages.

Hcp Seed Layer

Once the growth conditions were set, different types of seed layer materials were studied. Sample structures Si/Co,Mg,Ti (8)/ Co,Mg,Ti (12)/CoCrPt-SiO$_2$(20)/Ta(5) were grown using the optimised sputtering conditions.

Out of plane $\vartheta - 2\vartheta$ measurements were carried out to examine the texture of the seed layers and the CoCrPt-SiO$_2$ (002) as shown in Figure 6.11. Co and Mg seed layer based samples were both able to induce an (002) perpendicular orientation. The (002) peaks were observed at 44.4° and 34.5°, respectively. However the intensity of the peaks was more than 10 times lower than that for the Ru (002) peak. Therefore the Co seed layer induced a weaker CoCrPt-SiO$_2$ (002) texture at 42.4°. Although Ti has an hexagonal crystal structure, the (002) plane was not observed from the scan. Instead a weak (100) plane was measured at 35.1°. Therefore the CoCrPt-SiO$_2$ (002) was not able to grow with perpendicular orientation on Ti and as a result there was no CoCrPt-SiO$_2$ peak present in the scan.
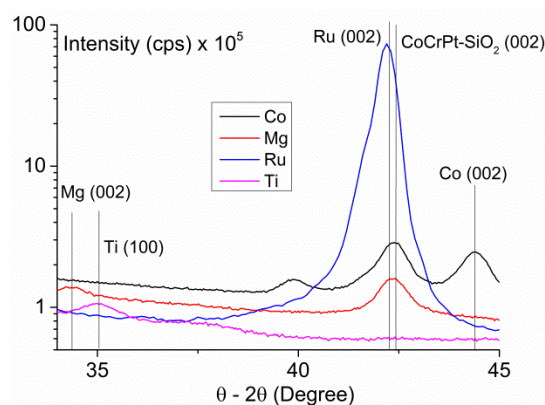
Figure 6.11 Out of plane $\vartheta - 2\vartheta$ measurements for a range of hcp materials.

The magnetic properties of all samples were measured using an AGFM at room temperature as shown in Figure 6.12. The magnetic properties are summarised in Table 6.4. The sample grown on a Ru seed layer showed the highest squareness of 0.91 with coercivity of 1.2kOe, which indicated the Ru seed layer and CoCrPt-SiO$_2$ were well textured in the perpendicular direction. Co, Mg and Ti seed layer based samples resulted in relatively low squarenesses of 0.32, 0.18 and 0.09, respectively. This is because the c-axis of the CoCrPt-SiO$_2$ was poorly textured out of the plane. Therefore the results of the XRD agree with the magnetic measurements.

Figure 6.12 Hysteresis loops for CoCrPt films gorwn on various hcp seed layers.
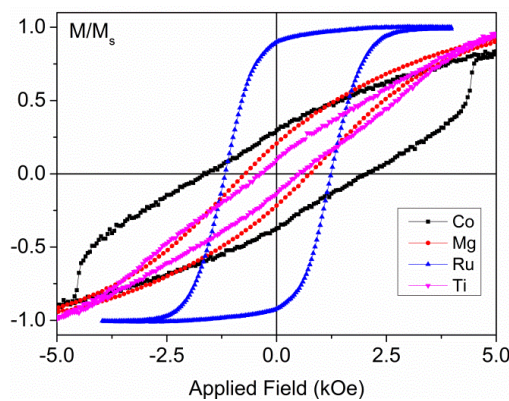
Seed Layer	H_c ($\pm 5^{-3}$kOe)	M/M$_s$ (± 0.02)
Co	1.78	0.32
Mg	0.76	0.18
Ru	1.20	0.91
Ti	0.52	0.09

Table 6.4 Summary of magnetic properties of CoCrPt samples grown on various hcp seed layers.

The grain size and its physical structure in conventional perpendicular recording media determine the areal density achievable. The median grain size for typical CoCrPt-SiO$_2$ media is reported to be about 7 - 9nm, [4]. Bright field TEM images were taken using a JEOL 2011 TEM in order to observe the grain size distributions and levels of segregation with different seed layer materials. The images were taken using x100k magnification. 15 images were acquired across three different areas per sample and a total number of 500 grains were measured to ensure good statistics.

The TEM images and the corresponding median grain sizes and standard deviations are shown in Table 6.5. Co, Mg and Ru seed layers were able to create a segregated grain structure. However it was obvious that the Ru seed layer sample generates a greater and more uniform degree of segregation compared with the samples grown on Co and Mg seed layers. Also Ru seed layer sample gives a smaller median grain

diameter and higher squareness. The Ti seed layer based sample exhibited a polycrystalline texture and no voided structure was observed. Therefore the grain decoupling is weak and leads to a low squareness and coercivity.
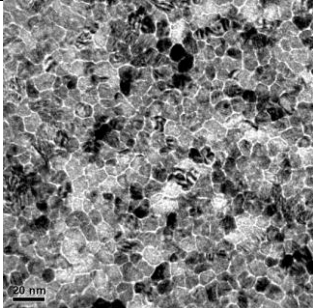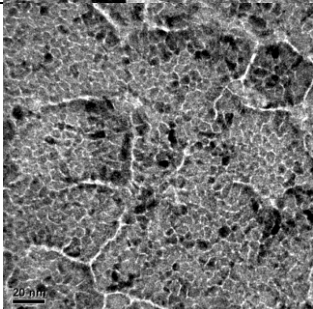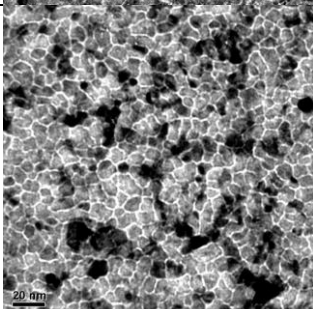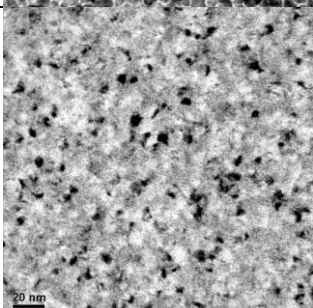
Seed layer Material	TEM Image	D_m (±0.2nm)	σ	H_c(±5⁻³kOe)	M/M_s (±0.02)
Co		7.6	0.30	1.78	0.32
Mg		6.2	0.25	0.76	0.18
Ru		6.2	0.34	1.20	0.91
Ti		7.2	0.26	0.52	0.09

Table 6.5 TEM images and summary for CoCrPt grown on different hcp seed layer.

fcc Seed Layer

An alternative way to texture CoCrPt-SiO$_2$ (002) in the out of plane orientation is by growing a (111) plane of an fcc material in the perpendicular direction. This is due to the fact that the basal plane of the hcp (002) CoCrPt is identical to the fcc (111) plane as shown in Figure 6.13. Three different materials with an fcc crystal structure were used as seed layers; Ag, CoFe and Pt. A set of three samples were sputtered with the structures of Ta(5)/Ag,CoFe,Pt(8)/ Ag,CoFe,Pt(12)/CoCrPt-SiO$_2$(20)/Ta(5) using the optimised sputtering conditions discussed previously.
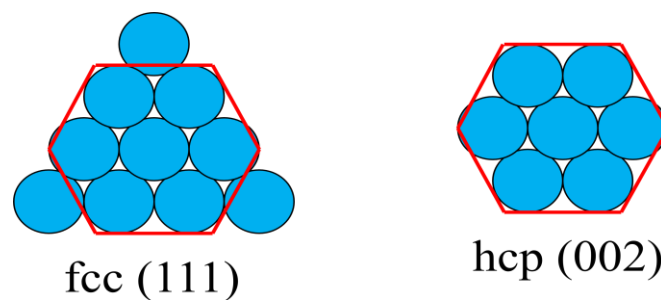
Figure 6.13 Schematic diagram of fcc (111) and hcp (002) basal plane.

The crystal structure of all samples was measured using the Rigaku X-ray diffractometer. Figure 6.14 shows the $\vartheta - 2\vartheta$ measurements for all fcc seed layer based samples. A strong CoCrPt-SiO$_2$ (002) peak was observed for the Pt seed layer based sample. This is because the Pt (111) plane at 39.6° was well textured creating a basal plane which is identical to the Ru (002). Therefore a well defined CoCrPt-SiO$_2$ (002) peak was observed at 42.2°. The Ag seed layer based sample was also able to induce a (111) plane at 38.2° but the crystallographic texture was about ten times weaker than that for the Pt (111). Therefore the CoCrPt-SiO$_2$ (002) peak was not well defined. CoFe induced a (110) plane at 45.1° and it also resulted in a poor texture in the CoCrPt-SiO$_2$ in comparison to the Pt seed layer based sample. Hence a high squareness is not expected to be observed in both Ag and CoFe seed layer based samples.
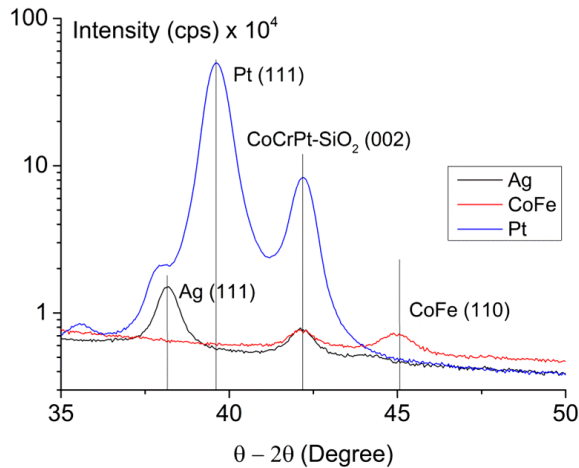
Figure 6.14 XRD measurements for fcc seed layer based samples.

Hysteresis loops were measured using the AGFM at room temperature. The magnetic properties are summarised in Table 6.6. The Pt seed layer based sample has the highest squareness of 0.87 with a coercivity of 2.16 kOe as shown in Figure 6.15. This is expected from the XRD measurements shown in Figure 6.14. This is because the Pt (111) induced a perpendicular orientation and its basal plane is identical to the hcp (002) of the CoCrPt as shown in Figure 6.13. Ag and CoFe seed layer based samples resulted a low squareness of 0.21 and 0.18, respectively. Ag induced a (111) texture perpendicular to the plane but resulted in a weak CoCrPt-SiO$_2$ (002) texture. The intensity of the Ag (111) peak is more than 10 times weaker than that of the Pt (111) peak and therefore it induced a much weaker CoCrPt-SiO$_2$ (002) texture of intensity 0.78×10^4cps. CoFe (110) has a different basal plane to the hcp (002) of CoCrPt therefore a poor texture of the CoCrPt-SiO$_2$ (002) was induced. The results of the magnetic measurements are again consistent with the XRD data.
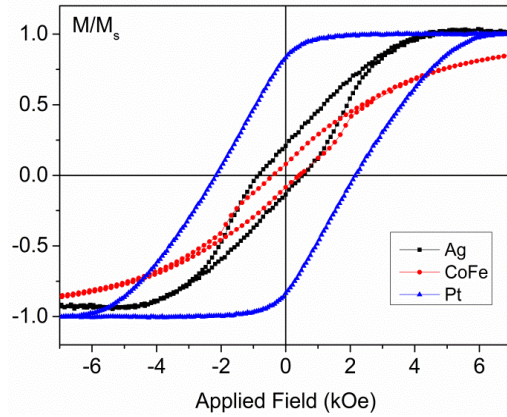
Seed Layer	H_c ($\pm 5^{-3}$kOe)	M/M_s (± 0.02)
Ag	0.87	0.21
CoFe	0.38	0.18
Pt	2.16	0.89

Table 6.6 Summary of the magnetic properties of CoCrPt layer grown on fcc seed layer based samples.

Figure 6.15 Hysteresis loops for CoCrPt grown on fcc seed layer based samples.

TEM images were taken using a JEOL 2011 TEM. More than 15 images were acquired across three different areas. A summary of the median grain size and standard deviation are shown in Table 6.7. The Ag seed layer based samples induced small grains with D_m = (4.7 ± 0.2)nm. A segregated grain structure can also be observed but some of the grains were merged together as shown in the TEM image. CoFe and Pt seed layer based samples induced a segregated grain structure with the D_m = (6.5 ± 0.2)nm and (5.8 ± 0.2)nm, respectively. Samples grown on Ag and CoFe seed layers cannot be considered for HAMR media due to the low squareness of the hysteresis loops. The Pt based film has the potential to replace Ru because of the resulting high squareness as well as inducing a strong CoCrPt-SiO$_2$ (002) texture in the perpendicular direction. The grain volume of the Pt based sample was $\frac{\pi 5.8^3}{6}$=102nm^3 which is about 20% smaller than the Ru seed layer based sample of $\frac{\pi 6.2^3}{6}$=125nm^3.
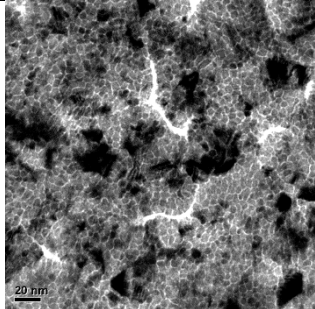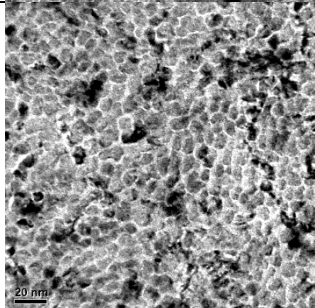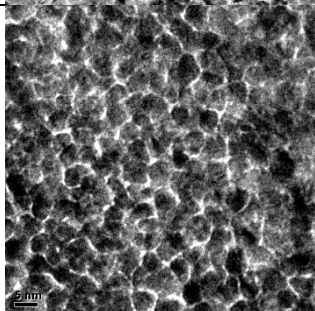
Seed layer Material	TEM Image	D_m (±0.2nm)	σ	H_c (±5^{-3}kOe)	M/M$_s$ (±0.02)
Ag		4.7	0.25	0.87	0.21
CoFe		6.5	0.27	0.38	0.18
Pt		5.8	0.28	2.16	0.89

Table 6.7 TEM images and summary of CoCrPt layer grown on fcc seed layer.

bcc crystal structure

Bcc materials; Cr, Fe and V have also been used as seed layers to study the growth of the CoCrPt-SiO$_2$ layer. A set of three samples with the structures: Ta(5)/Cr,Fe,V(8)/Cr,Fe,V(12)/CoCrPt-SiO$_2$(20)/Ta(5) were sputtered using the optimised sputtering conditions. A 5nm fast Ta layer was sputtered to create an amorphous surface. Two step seed layers were sputtered using 3mTorr and 30mTorr process pressures and followed by a 20nm CoCrPt-SiO$_2$ layer. The samples were capped with a 5nm of Ta to prevent oxidation.
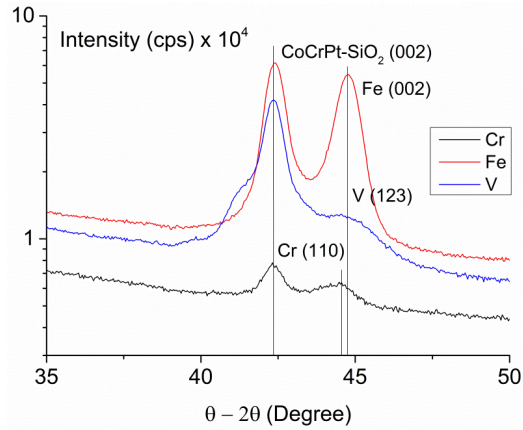
Figure 6.16 $\vartheta - 2\vartheta$ measurements for all bcc materials.

Figure 6.16 shows out of plane $\vartheta - 2\vartheta$ measurements for all samples. Cr (110), Fe (002) and V (123) planes were observed at 42.4°, 44.7° and 44.8°, respectively. Because the bcc (110), (002) and (123) basal planes are not identical to the hcp (002) of CoCrPt, a high intensity CoCrPt-SiO$_2$ (002) peak was not expected in the scan. The CoCrPt-SiO$_2$ (002) peak was observed at 42.2° for all samples but the intensity was below 10^4cps as expected. Therefore the CoCrPt-SiO$_2$ (002) peak was poorly textured on these seed layer and a low value of squareness was expected.

Figure 6.17 Hysteresis loops for CoCrPt grown on bcc seed layer based samples.
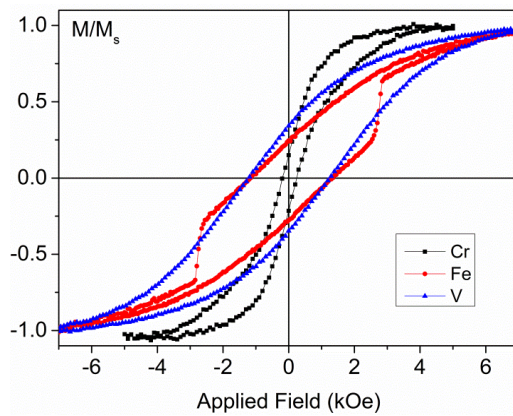
Seed Layer	H_c ($\pm5^{-3}$kOe)	M/M_s(±0.02)
Cr	0.20	0.15
Fe	1.15	0.25
V	1.21	0.35

Table 6.8 Summary of the magnetic properties of CoCrPt layer grown on bcc seed layer based samples.

The hysteresis loops were measured using the AGFM at room temperature as shown in Figure 6.17. The magnetic properties are summarised in Table 6.8. The squareness of all samples was below 0.40 which indicates the seed layer materials were not able to induce strong perpendicular anisotropy in the CoCrPt-SiO$_2$ layer.

The hysteresis loops show that the grains in the film grown on the Cr seed layer were not decoupled as shown in the TEM images and in Table 6.9.

From the TEM images the Cr seed layer sample has the largest D_m of (8.0 ± 0.2)nm Fe and V seed layer based samples have better grain segregation compared with Cr. Fe and V seed layer based samples have a value of D_m of (6.9 ± 0.2)nm and (6.7 ± 0.2)nm, respectively. However Fe based seed layer samples have an elongated grain structure and induces the Fe (002) orientation perpendicular to the plane.
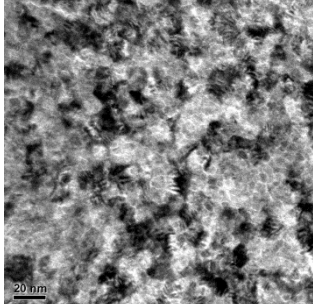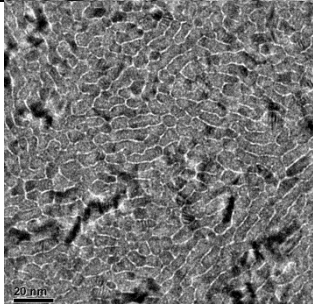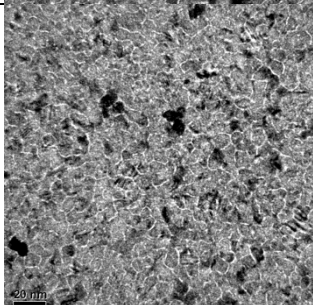
Seed layer Material	TEM Image	D_m (±0.2nm)	σ	H_c (±5⁻³kOe)	M/M$_s$ (±0.02)
Cr		8.0	0.30	0.20	0.15
Fe		6.9	0.23	1.15	0.25
V		6.7	0.25	1.21	0.35

Table 6.9 TEM images and summary of CoCrPt grown on bcc seed layer.

None of the bcc seed layers are capable of replacing Ru because the squareness of the hysteresis loop is not close to 1.00. Furthermore the grain sizes are all above 6.7nm whereas the Ru seed layer induced a median grain diameter of D_m = (6.2 ±

0.2)nm. Note that the difference in terms of grain volume is $\frac{\pi 6.7^3}{6}$=157nm^3 and

$\frac{\pi 6.2^3}{6}$=125nm^3, the grain volume is about 25% larger.

It has been found that the optimum seed layer material for HAMR media based on exchange bias is Ru. This was because it induced a high squareness of 0.91 and a coercivity of 1.2kOe in the CoCrPt layer at room temperature. Well segregated grains were also clear in the TEM image.

Exchange bias is highly dependent on the spin structure between the AF and F layers, [8]. In the next two Sections 6.3 & 6.4 the magnetic properties after deposition of an IrMn layer between the seed layer and CoCrPt-SiO$_2$ layer are described. The IrMn will also act as an exchange break layer to avoid exchange interactions between the SUL and the CoCrPt-SiO$_2$ layer in a real medium.

6.3 Rotational Measurements

Based on the XRD measurements in Section 5.4 it is known that Ru seed layers produce a weak texture in IrMn (111). Under these conditions the exchange bias induced in CoPtCr-SiO$_2$ by the presence of a IrMn layer grown on a different dual seed layers and rotational magnetic measurements were performed. 20nm thick dual Cu, Ru and NiCr seed layers were sputtered. Process pressures of 3mTorr and 30mTorr, respectively, were used to the initial and second layers. A 6nm thick IrMn layer and a 15 nm thick CoCrPt-SiO$_2$ were also grow. The full structure is shown in Figure 6.18.

| Ta (5 nm) |
| CoCrPt-SiO$_2$ (15 nm) |
| IrMn (6 nm) |
| Cu/Ru/NiCr (12 nm) |
| Cu/Ru/NiCr (8 nm) |
| Ta (5 nm) |
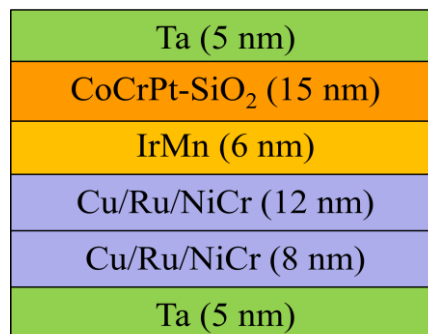
Figure 6.18 Sample structures of Cu, Ru and NiCr dual seed layers.

Rotational measurements were undertaken using a Model 10 Microsense VSM. The sample was set at 498K in a field of 10kOe perpendicular to the plane (90°) and at angles down to in-plane (0°) in steps of 10° for 60 minutes. The loop was then measured at the setting angle. The perpendicular hysteresis loop for all samples is shown in Figure 6.19a. An exchange bias of H_{ex} < 150Oe was observed for all samples and both values of coercivity were not shifted to the negative values of field.

The value of the exchange bias H_{ex} was measured as a function of the setting angle as shown in Figure 6.19b. For (111) planes of IrMn oriented in-plane there should be another set of (111) planes oriented at around 70°. As can be seen from Figure 6.19b there is a significant value of the loop shift of H_{ex} = (180 ± 5)Oe at 80° with the dual Ru seed layers. Unfortunately this falls away to H_{ex} < 110Oe for the perpendicular case. Cu and NiCr seed layer based samples result a similar shape of the curve. The highest exchange bias was measured at 80° and a reduction of H_{ex} was measured in the perpendicular direction.
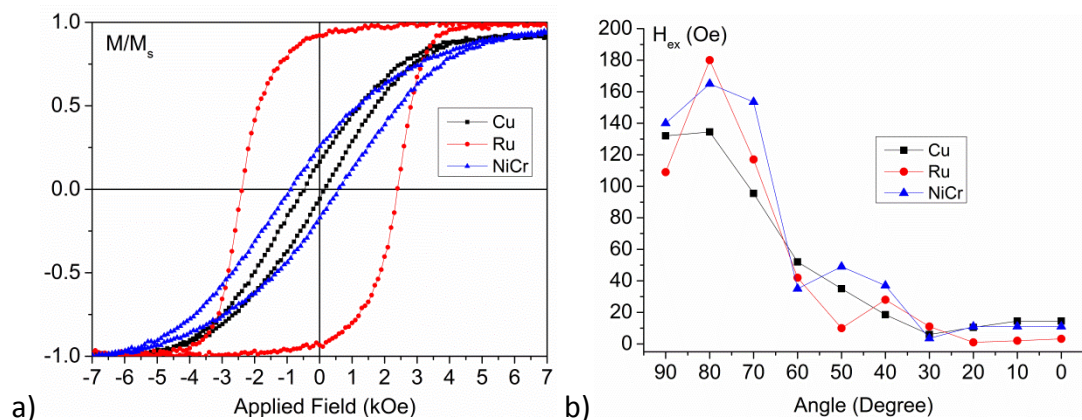
Figure 6.19a) Perpendicular hysteresis loop measurements. b) Exchange bias as a function of measurement angles.

This result is of significance because it demonstrates that coupling between the conventional recording alloy and IrMn can be achieved using a dual Ru seed layer. Another feature that can be noticed from the dual Ru seed layer based sample hysteresis loop was the high coercivity and squareness of H_c = 2.4kOe and 0.92, respectively. This indicates that the perpendicular anisotropy of CoCrPt-SiO$_2$ remains after the deposition of a 6nm IrMn layer. These results were not

comparable with Aley et al. [8] in an in-plane system using a single thin seed layer of 6nm compared to the 20nm thick layer required for grain segregation.

6.4 Perpendicular Exchange Bias Structure

Perpendicular exchange bias can be achieved as discussed in the last section. However the main objective of this study is to shift the hysteresis loop so that both values of coercivities H_{C1} and H_{C2} are located at negative values of applied field. In a paper by Chen et al. [124] perpendicular exchange bias using CoFe/IrMn bilayers system was described.

The samples reported on in this paper were sputtered using a dc magnetron sputtering system at room temperature. The samples had an unusual top exchange bias based on the structure Ta(5)/Pt(5)/Co$_{90}$Fe$_{10}$(0.8)/Ir$_{22}$Mn$_{88}$(t$_{IrMn}$)/Pt(2). The thickness of the Co$_{90}$Fe$_{10}$ layer was about 2 atoms thick and tilted the Mn spins of IrMn alloy perpendicular to the plane. The thicknesses of the IrMn layers used were 4, 6 and 10nm. The hysteresis loops were measured using the Extraordinary Hall Effect (EHE) in the perpendicular orientation at room temperature. The highest exchange bias H_{ex}= 913Oe was measured using a 4nm IrMn layer, [124]. The crystal structure was characterised using X-ray diffraction. Out of plane $\vartheta - 2\vartheta$ scans were carried out for all samples and the IrMn (111) and Pt (111) peaks were observed from the scans where the IrMn (111) has the lowest intensity using the t$_{IrMn}$ = 4nm sample. This indicates that a weak IrMn (111) texture induced the highest perpendicular exchange bias.

The exact origin of the perpendicular orientation of the exchange bias is not addressed by Chen et al., [124]. However it seems probable that the very thin CoFe layer (0.8nm or ~3 atoms) develops a strong perpendicular anisotropy similar to that which occurs in superlattices such a Co/Pt multilayer. If the IrMn layer does not have high in-plane anisotropy due to the poor (111) texture then the exchange coupling between the CoFe and the Mn ions may be sufficient to re-orient the coupling perpendicular to the plane.

To test this hypothesis a set of six samples were sputtered using different bias voltages to optimise the exchange bias of the system. 5nm of fast Ta was deposited on top of the Si substrate to create an amorphous surface. It was then followed by 5nm of Pt as a seed layer. Following Chen et al. [124] to optimise the perpendicular anisotropy, an ultra thin layer of 0.8nm Co was deposited on top of the seed layer. 4nm of IrMn was deposited on top of the F layer to create a top bias system. The samples were then capped by 5nm of Ta to prevent oxidation. The sample composition is shown in Figure 6.20.

| Ta (5 nm) |
| IrMn (4 nm) |
| Co (0.8 nm) |
| Pt (5 nm) |
| Ta (5 nm) |
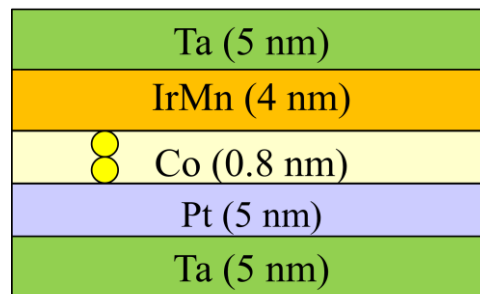
Figure 6.20 Schematic diagram of the sample composition.

Magnetic measurements were undertaken using a Model 10 Microsense VSM at 100K in order to understand the influence of the different bias voltages. A low temperature was required due to the low thickness of the AF layer in the structure defined by Chen et al., [124]. The samples were set at 498K in a field of 20kOe perpendicular to the substrate for 60 minutes. A hysteresis loop was then measured at the setting field angle. Figure 6.21 shows the hysteresis loops for the sample which was sputtered using a bias voltage of 800V. The hysteresis loop was shifted by more than H_{ex} = 1.5kOe with a coercivity of ~1kOe at 100K. No exchange bias was observed for samples grown at low bias voltages because the AF grains are too small so that they were not thermally stable at the measuring temperature of 100K. The second hysteresis loop was measured using the same setting conditions to make sure that this measurement can be reproduced.
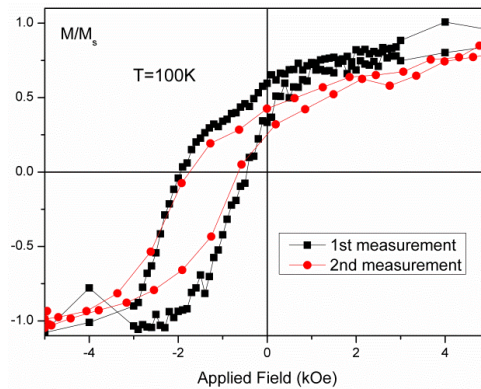
Figure 6.21 100K hysteresis loops measurements of a Co insertion layer sample.

A squareness of about 0.70 was measured indicating that the perpendicular anisotropy of the F layer was not lying perfectly out of plane. However the coercivities of the hysteresis loop H_{c1} and H_{c2}, were both located at negative values. This achieves one of the most important requirements of this study. Due to the fact that the loop has been completed shifted to one side of the origin indicates that any data written to this system can only be erased using thermal energy which fulfils one of the initial objectives of the work.

Further modifications have to be made in order for this system to be capable of forming a HAMR media. The system has to exist as a bottom exchange bias system so that the IrMn layer can act as an exchange break layer. This layer is essential for recording media because it prevents the exchange interaction between the SUL and recording layer so that it can improve the SNR. This modification will be further discussed in the following section. Another criterion is that the measurement temperature has to be at room temperature rather than 100K. The measurement temperature modifications will be discussed in detail in Section 6.6. Finally the system must use a segregated F layer to enable a small bit size.

6.5 Introduce Conventional Recording Layer to Perpendicular Exchange

In conventional PRM an SUL is used to improve the writability. The SUL is made of a soft material hence domains occur to minimise the magnetostatic energy. These domain walls would generate stray fields and induce noise during the reading

141

process. In order to minimise the noise generated from the SUL an exchange break layer was introduced into the media, [17].

The sample structure of the perpendicular bottom exchange bias system is shown in Figure 6.22. The sputtering conditions for the Ta, Pt, Co and IrMn layers were the same as those described in Section 6.4 and 10nm and 20nm CoCrPt-SiO₂ layers were deposited to optimise the magnetic properties of the sample.

| Ta (5 nm) |
| CoCrPt-SiO₂ (10, 20 nm) |
| IrMn (4 nm) |
| Co (0.8 nm) |
| Pt (5 nm) |
| Ta (5 nm) |
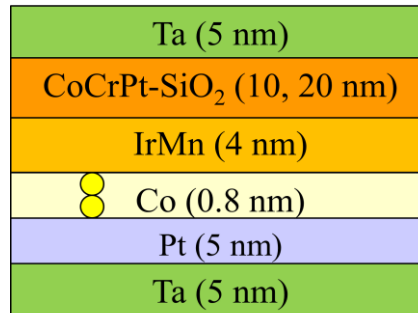
Figure 6.22 Schematic diagram of sample composition.

The concept of this design is that the ~2 atom Co layer will induce a perpendicular spin orientation on the Mn ions in the IrMn alloy which will then couple to the CoCrPt inducing an exchange bias in a conventional storage layer.

Magnetic measurements were undertaken using a Model 10 Microsense VSM at 100K in order to understand the influence of the different thicknesses of the CoCrPt-SiO₂ layer. The samples were set at 498K in a field of 20kOe perpendicular to the substrate for 60 minutes. A hysteresis loop was then measured at the setting angle. Figure 6.23 shows the hysteresis loop measurements for both samples at a measurement temperature of 100K. For the sample with a 10nm CoCrPt-SiO₂ layer, an exchange bias of H_{ex} = (240 ± 5)Oe and squareness of 0.80 were measured. With a 20nm thick CoCrPt-SiO₂ layer, a relatively low exchange bias of H_{ex} = (115 ± 5)Oe and a squareness of 0.15 were measured.

This is because it is not ideal to grow CoCrPt-SiO on top of an IrMn (111) plane. However the data is consistent with the established F layer thickness t_f dependence of H_{ex}, [125]. For in-plane exchange bias systems used in read heads the value of t_f is typically 2-5nm [126] so a much thinner CoCrPt-SiO₂ layer may be

required. Also the temperature dependence of H_{ex} in polycrystalline films derives from the thermal stability of the AF grains as described by the well established York Model, [59]. Hence given the small grain size in the films, a thicker IrMn layer may be required for room temperature performance. The XRD data will be discussed in detail in Section 6.6.
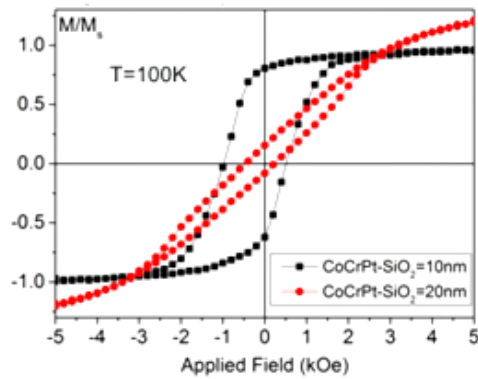
Figure 6.23 Hysteresis loops measurements at 100K.

Further optimisation in both AF and F layers is required as well as an examination of the setting temperature T_{Set} and thermal stability temperature T_{NA} which will be discussed in next section.

6.6 Structure and Temperature Optimisation

It has been proven that perpendicular exchange bias can be induced at 100K using a bottom bias system. However the coercivities were not located at negative field values. Therefore further optimisation of the sample structure and measurement temperature was carried out. The objective in this work was to produce a hysteresis loop in which both coercivities are located at a negative field at room temperature so that any data stored in the medium cannot be erased by a magnetic field.

Three samples were sputtered with the structure shown in Figure 6.24. The 5nm Ta layer was used to create an amorphous surface to suppress crystal habit from the Si or SiO_2. The selected seed layer was a 5nm thick Pt layer based on the paper by Chen et al., [124]. The Pt layer was followed by a 0.8nm thick Co layer to induce the perpendicular bottom exchange bias. The sample was capped using 5nm Ta to prevent oxidation.
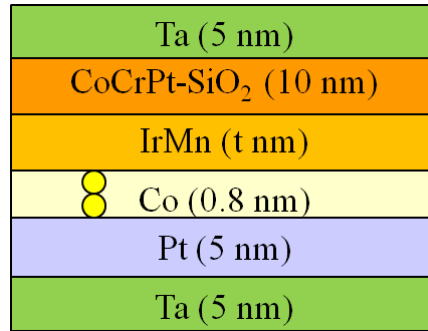
Figure 6.24 Schematic diagram of the sample structure.

Low temperature magnetic measurements were undertaken using a Model 10 VSM. The samples were initially set at 498K in a field of 20 kOe perpendicular to the plane for 60 minutes. The samples were then field cooled to 100K. A low temperature hysteresis loop was then measured. The values of exchange bias for all samples are similar as shown in Figure 6.25 but the largest exchange bias of H_{ex}= (230 ± 5)Oe was measured for the 4nm thick IrMn sample. This indicates that the exchange bias was saturated using 4nm of IrMn. Because these measurements were taken at 100K a further AF layer optimisation was carried out and is discussed later in this section.
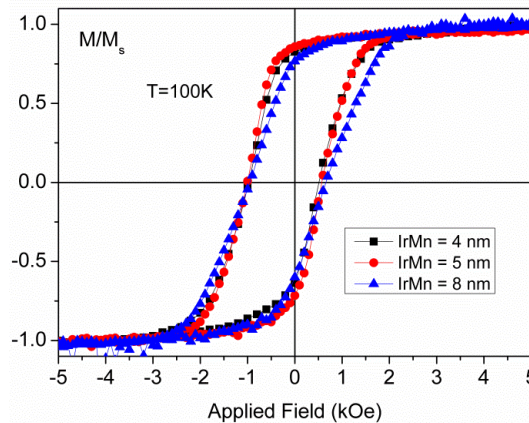
Figure 6.25 100K hysteresis loop measurements for optimising the AF layer thickness.

F layer optimisation

F layer optimisation experiments were carried out in order to maximise the exchange bias to a point where both H_{c1} and H_{c2} were both located at negative applied fields. Another set of four samples with identical sample structures were grown as shown in Figure 6.26. The thickness of the IrMn layer was fixed at 4nm because the highest exchange bias was achieved using this thickness. The thickness

of the CoCrPt-SiO$_2$ layer was varied between 2nm to 10nm in 2nm steps to maximise the exchange bias. The sputtering conditions such as the process pressure and bias voltage used were the same as in the previous experiments. We expected the exchange bias to vary as $H_{ex} \propto 1/t_f$ where t_f is the thickness of the F layer, [125].
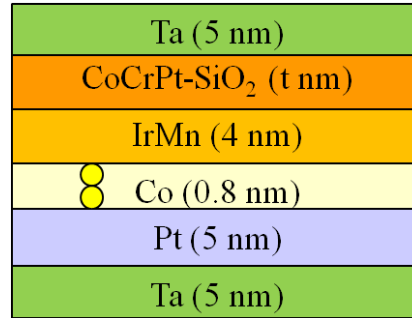
Figure 6.26 Schematic diagram of optimising CoCrPt-SiO$_2$ layer thickness.

Low temperature magnetic measurements were undertaken for all samples and the hysteresis loops are shown in Figure 6.27. Samples with 2nm and 4nm thick CoCrPt-SiO$_2$ layers induced the largest exchange bias of H_{ex} = (1131 ± 5)Oe and (688 ± 5)Oe, respectively. The special feature of these two loops was that H_{c1} and H_{c2} was both located at negative fields. However the selected thickness of CoCrPt-SiO$_2$ for further study was 4nm because at this thickness the media would generate a larger signal for the read head. Figure 6.28 shows the exchange bias as a function of the thickness of the CoCrPt-SiO$_2$ layer. This showed the expected trend of $H_{ex} \propto 1/t_f$, [125]. The exchange bias decays to H_{ex} = (230 ± 5)Oe as the thickness of the F layer increases to 10nm. The hysteresis loops of the samples using a thickness of 2nm and 4nm CoCrPt-SiO$_2$ gave this unique feature.

The transition width of a medium can be expressed as ($a_0 = \delta_{med} M_r / H_c$) where δ_{med} is the thickness of the medium, M_r the remanence and H_c the coercivity. Since the transition width is inversely proportional to the SNR therefore a minimum value of δ_{med} and M_r are required to increase the SNR. A low thickness of the F layer is required for this system to reduce the transition width and M_R can be increased by decreasing the Cr content in the CoCrPt-SiO$_2$ alloy.
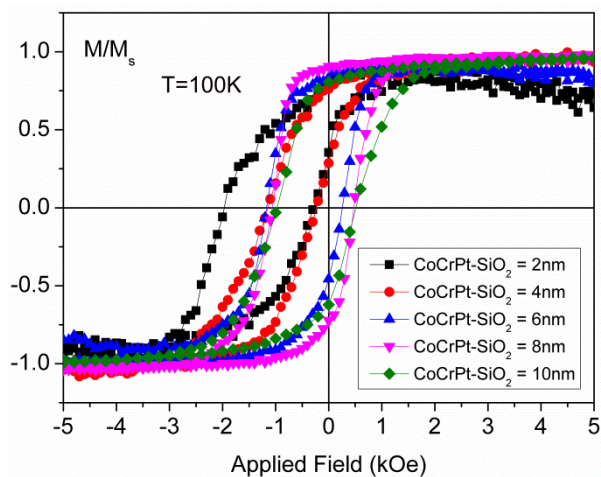
Figure 6.27 100K hysteresis loop measurements with different thickness of CoCrPt-SiO$_2$.

This result demonstrates one of the key objectives of this study. However the sample composition needs to be further optimised in order to exhibit the same magnetic properties at room temperature.
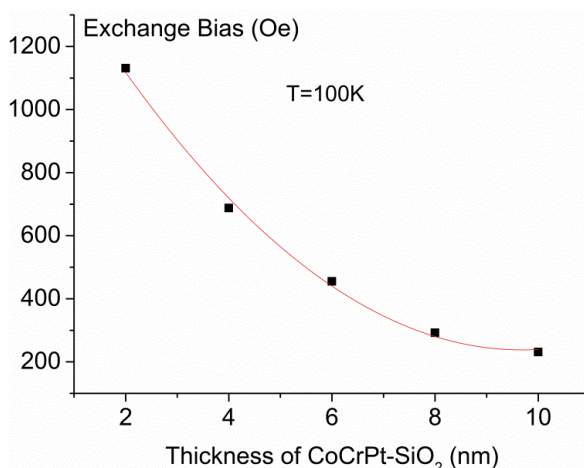
Figure 6.28 Exchange bias as a function of the thickness of the CoCrPt-SiO$_2$.

Room temperature measurements were carried out using the samples with 2nm and 4nm of CoCrPt-SiO$_2$. The samples were set at 498K in an applied field of 20kOe perpendicular to the plane for 60 minutes. The samples were then field cooled to 298K and a hysteresis loop measured as shown in Figure 6.29. Exchange bias value of H_{ex} = (269 ± 5)Oe and (142 ± 5)Oe were measured for the 2nm and 4nm thick CoCrPt-SiO$_2$, respectively. These results indicated that a significant exchange bias at room temperature can be achieved by adding the extra 2 atom Co layer underneath the IrMn layer.
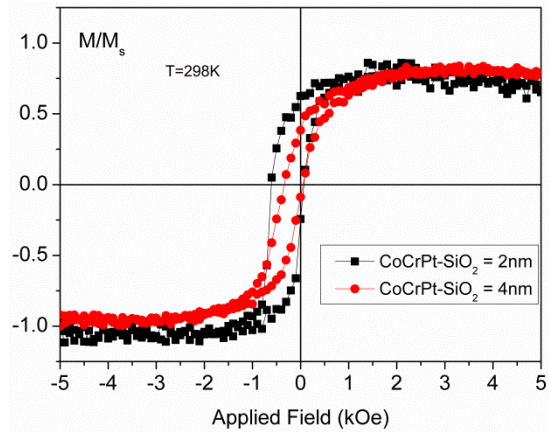
Figure 6.29 Room temperature hysteresis loop using 2nm and 4nm CoCrPt-SiO₂.

It has already been shown that perpendicular exchange bias can be achieved at room temperature as shown in Figure 6.29. However one of the coercivities was not located at a negative value of the applied field which means that the data can be demagnetised by a magnetic field. Therefore a further optimisation of the AF layer was carried out.

AF Layer Optimisation

A set of 5 samples were grown using the sample structure shown in Figure 6.30. The sputtering conditions and thicknesses for the Ta, seed layer, Co and CoCrPt-SiO₂ remain unchanged. The only variable in this sample set was the thickness of the IrMn layer which was varied between 4nm to 12nm in 2nm steps.
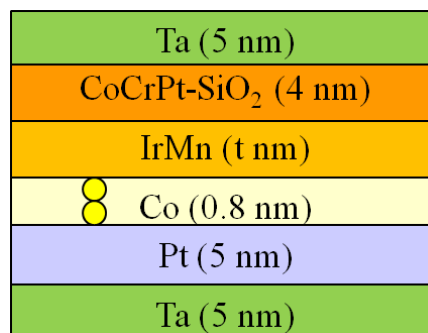
Figure 6.30 Schematic diagram of the sample structure for optimising IrMn thickness.

Room temperature magnetic measurements were undertaken for all samples. The samples were set at 498K in a field of 20kOe perpendicular to the plane for 60 minutes. The samples were then field cooled to 298K. Room temperature hysteresis

loops were then measured as shown in Figure 6.31. The exchange bias is plotted as a function of the thickness of the IrMn in Figure 6.32. The largest exchange bias of H_{ex} = (239 ± 5)Oe was measured for a sample with a 6nm thick IrMn layer. The exchange bias then gradually decreased to H_{ex} = (119 ± 5)Oe as the thickness of IrMn increases to 12nm. The exchange bias is based on the volume of the AF grains between V_c and V_{set} [79] as discussed in Section 3.7. At 6nm most of the AF grains are thermally stable and saturate at the setting conditions. Therefore it induced the highest exchange bias in this system. For an AF thickness increased to 12nm the AF grains had too large volume and cannot be fully set. Therefore the exchange bias reduces. It is clear that as the thickness of the IrMn increased above 6nm the hysteresis loop had coercivities H_{c1} and H_{c2} were both shifted to negative fields at room temperature. This is a key result.
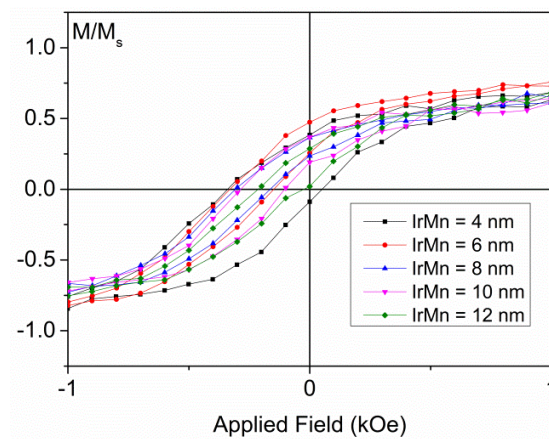
Figure 6.31 Hysteresis loop measurements with different thickness of IrMn layer.
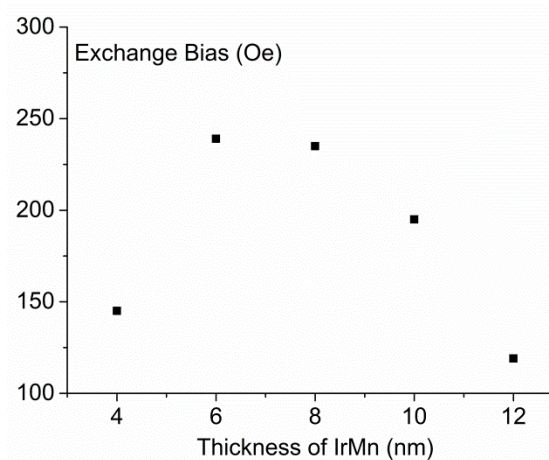
Figure 6.32 Exchange bias as a function of the thickness of IrMn.

It is essential to prove that all the AF grains on the samples were fully aligned at T_{Set} = 498K and thermally stable at T = 298K. The sample with a 6nm thick IrMn layer was used to show that T_{Set} = 498K achieves this effect. A series of five measurements were undertaken. The samples were initially set at a temperature T_{Set} in a field of 20kOe for 60 minutes. The samples were then field cooled to 298K and a hysteresis loop measured. The value of T_{Set} was varied between 498K and 518K in 5K steps. The hysteresis loops are shown in Figure 6.33. The value of the exchange bias H_{ex} remained constant for all measurements. This indicates that all the AF grains were fully aligned at T_{Set} = 498K.
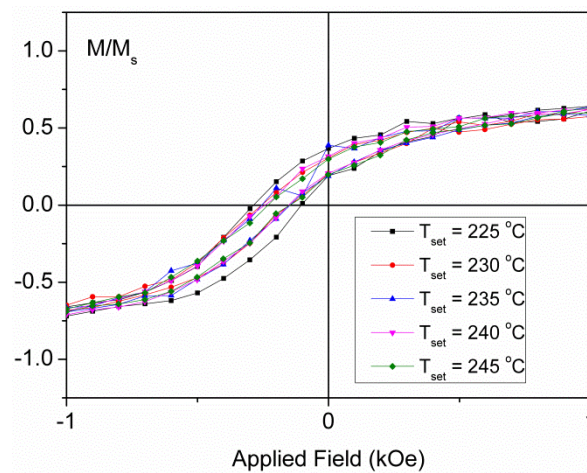
Figure 6.33 The setting temperature effect of the sample using 6nm of IrMn.

Another measurement was carried out to examine T_{NA} for the IrMn layer. The sample which was selected to perform this measurement is that with the highest exchange bias as shown in Figure 6.32. The sample was initially set at 498K in a field of 20kOe for 60 minutes. The sample was then field cooled to 298K and a first hysteresis loop measured. A large negative field was then applied for 30 minutes at room temperature. The second hysteresis loop was then measured. The first and second hysteresis loops are shown in Figures 6.34. The value of exchange bias did not vary between the first and second hysteresis loops, indicating that the samples have thermally stable AF grains at room temperature and can only be reversed by thermal energy.
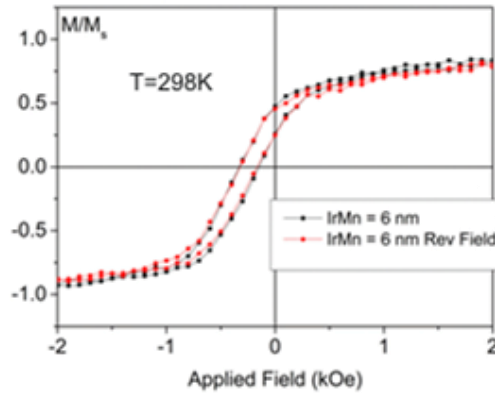
Figure 6.34 Thermal activation effect at 298K.

A segregated grain structure would be required for this system because the AF grains which constitute the storage layer are by definition exchange decoupled. However with a continuous CoCrPt layer there would be a risk that the spread of the magnetisation across more than one F grain could result in the reversal of more than one AF grain in the layer beneath.

A dual seed layer system was used to create a voided structure of the thin film as discussed in Section 6.1. The single Pt seed layer was now replaced by a dual seed layer. The thicknesses of the seed layers were 8nm and 12nm Pt and were deposited using 3mTorr and 30mTorr process pressure, respectively. The Co, IrMn and CoCrPt-SiO$_2$ were sputtered using 1.86mTorr process pressure and there was a variation of the thickness of the CoCrPt-SiO$_2$ layer to achieve the optimum value of exchange bias. The samples were then capped with 5nm of Ta layer to prevent oxidation as shown in Figure 6.35.
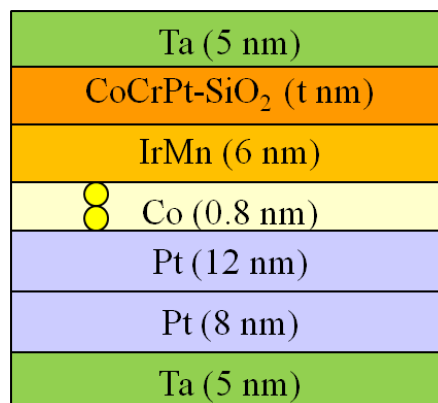
Figure 6.35 Optimisation of CoCrPt-SiO$_2$ layer using a dual Pt seed layer.

Room temperature magnetic measurements were undertaken using the Model 10 VSM. The samples were initially set at 498K in a field of 20kOe perpendicular to the plane for 60 minutes. The samples were then field cooled to 298K. Hysteresis loops were then measured as shown in Figure 6.36. All samples have a similar value of exchange bias of H_{ex} = (240 ± 5)Oe. The sample with the 3nm thick CoCrPt-SiO$_2$ layer shows the highest squareness of 0.75. The out-of-plane anisotropy collapsed once the thickness of the CoCrPt-SiO$_2$ layer was reduced to 2nm. This was because the F layer was too thin so that it did not form an out-of-plane anisotropy.
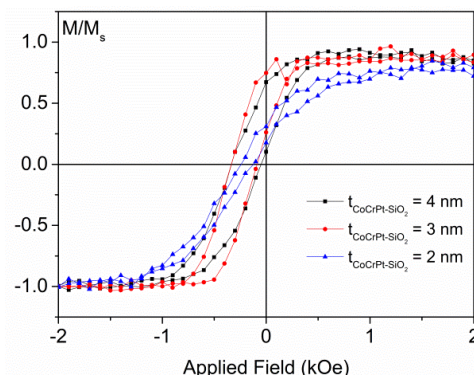
Figure 6.36 Room temperature hysteresis loops for the structures shown in Figure 6.35.

The key feature of these hysteresis loops was that the coercivities of H_{c1} and H_{c2} were both shifted to a negative field.

The particle sizes of the thin film samples were measured using a JEOL 2011 TEM. Bright field images were used to obtain the grain sizes in order to observe the grain size distribution. More than 15 images were taken across three different areas of the TEM grid and 500 particles were counted to ensure good statistics.

Figure 6.37a shows a TEM image taken at x100k magnification. No grain segregation was visible between the grains which could due to the ultra thin Co layer. Figure 6.37b shows the grain size distribution for the sample. The median grain diameter was D_m = (7.3 ± 0.2)nm with a standard deviation of σ_{lnD} = 0.23. The grain volume of this sample was $\frac{\pi 7.3^3}{6}$ = 204nm^3 which was about 40% larger than that for the Ru seed layer based sample discussed in Section 6.2.
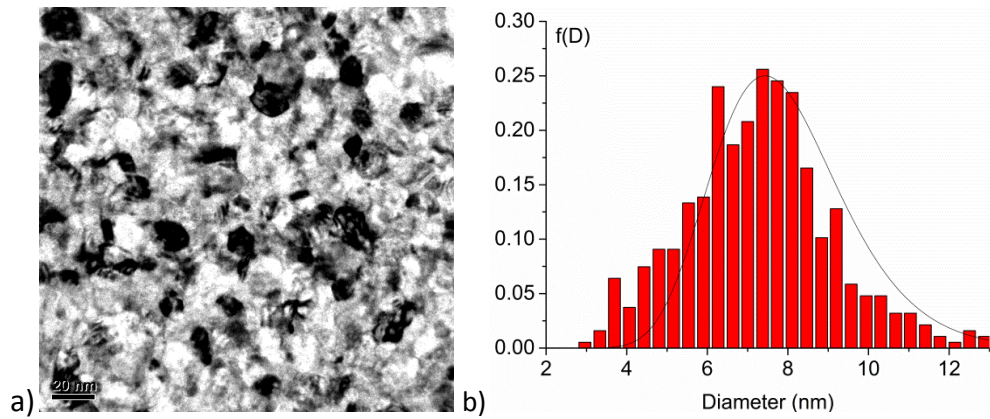
Figure 6.37a) Bright field TEM images using x100k magnification and b) Grain size distribution using 6nm IrMn and 3nm CoCrPt-SiO$_2$.

XRD measurements were carried out to determine the crystallographic texture of the samples. A set of seven samples was grown on Si substrates where the difference between samples was the sequential addition of an extra layer. The first sample had a structure of Si/Ta(5) while the structure of the last sample was Si/Ta(5)/Pt(8)/Pt(12)/Co(0.8)/IrMn(6)/CoCrPt-SiO$_2$(3)/Ta(5). This experiment was performed following a suggestion from Prof. T. Thomson of Manchester University, [127].

All samples were measured using a Rigaku SmartLab XRD system. A $\vartheta - 2\vartheta$ measurement was measured for each sample as shown in Figure 6.38. A strong peak was observed at 39.1° which indicated a strong (111) texture in the Pt layer. The second Pt layer which was sputtered using a high process pressure clearly induced a better Pt (111) texture in the sample as the sharpness of the peak increases. No peaks can be observed from the Co layer and this was because it was too thin and was not crystalline. WLa1 and Kb peaks which come from the filament and anode were observed at 35.7° and 37.9°, respectively. After depositing a 6nm thick IrMn layer, a shoulder peak was observed at 41.4° which is that for the IrMn (111) planes. A weak CoCrPt-SiO$_2$ (002) peak was observed at 42.7°. The peaks which appeared between 35° to 40° and 50° to 60° were from the Si substrate.
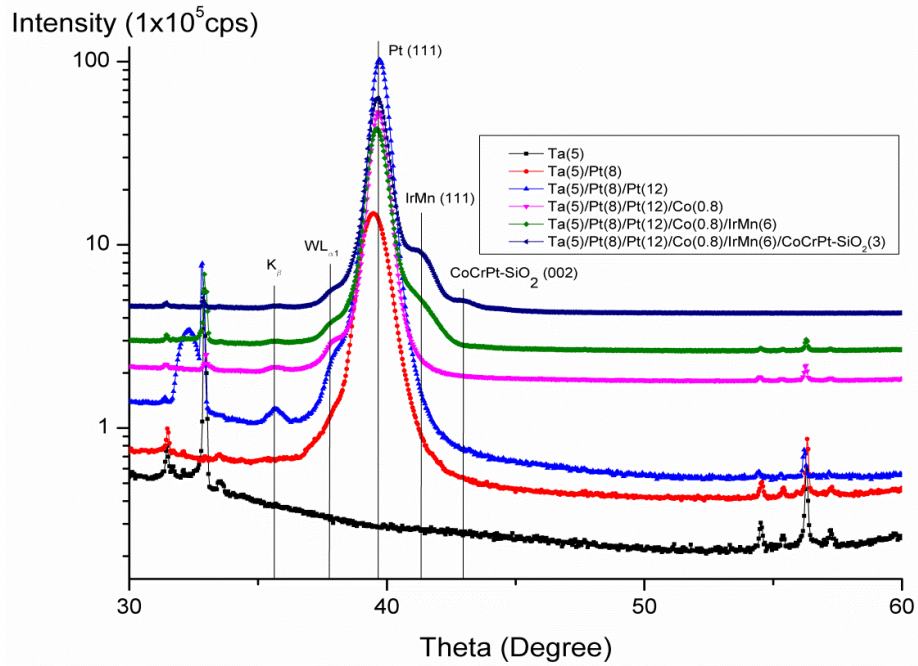
Figure 6.38 XRD out-of-plane $\vartheta - 2\vartheta$ measurements.

It is important to note that the IrMn (111) in-plane peak was observed in these scans. This indicates that we are still not able to re-orientate the IrMn (111) planes perpendicular to the plane. However an significant exchange bias of H_{ex} = (240 ± 5)Oe was observed in this sample. Therefore this is a magnetic effect due to the Mn spin alignment but not a texture effect of the IrMn (111) orientation. The exchange bias occurs using the 2-ion anisotropy of the ultra thin Co layer to induce perpendicular spin alignment in the IrMn.

The work achieved constitutes a breakthrough in terms of the overall study. We have now achieved exchange bias perpendicular to the plane in a system with a CoCrPt-SiO₂ layer. However no segregated grain structure was observed in this sample. It has been demonstrated that a recording layer as thin as 4nm is capable of generating a sufficient exchange field so as to align the grains in the IrMn layer at room temperature. Hence the feasibility of using the exchange bias effect has been demonstrated. The study has now achieved its main aim which was to provide proof of principle that a HAMR medium based on exchange bias could be achieved.

153

Chapter 7

7.1 Conclusion

There are two main objectives of this work. One of them was to develop a Co/Pt multilayer structure with perpendicular anisotropy and bottom exchange bias with IrMn layer in an out-of-plane orientation. The other one was to study perpendicular exchange bias in conventional recording media using a CoCrPt-SiO$_2$ recording layer.

A perpendicular exchange bias of H_{ex} = (688 ± 5)Oe and a blocking temperature of greater than 500K were achieved in this study. The optimisation of the Co/Pt multilayer system was achieved and the highest value of perpendicular exchange bias of H_{ex} = (688 ± 5)Oe was measured using a Cu seed layer based sample with 3 repeat units of Co(0.6)/Pt(1.6). This optimisation was achieved via the variation of the thickness of the IrMn. The optimum thickness was found to be 6nm. Two samples using 3 and 5 repeat units of Co(0.6)/Pt(1.6) resulted in a completely shifted loop at room temperature. The hysteresis loop showed that the coercivities of H_{c1} and H_{c2} were both shifted to negative values of the applied field of (-703 ± 5)Oe, (-586 ± 5)Oe and (-405 ± 5)Oe, (-248 ± 5)Oe, respectively. Therefore this system has the potential to work as a HAMR medium. The smallest grain size of the Cu seed layer based samples was (8.6 ± 0.2)nm which has to be reduced to sub 5nm and a segregated grain structure is required. The median blocking temperature of $<T_B>$ = >500K was measured; indicating that the sample was thermally stable at room temperature.

The Co/Pt multilayer samples described in this study exhibit a polycrystalline structure. Hence it is not suitable for a HAMR medium due to the coupling across more than one AF grain. However it is possible for applications as patterned media or CPP-GMR. These systems are used to store the information in a discrete unit or cell which means that there is no coupling between in each cell.

In conventional recording media a segregated grain structure is required. The sputtering conditions for this system such as process pressure and the required materials for producing a segregated grain structure were achieved. This structure is important for CoCrPt-SiO$_2$ recording media because it provides RKKY exchange de-coupling between the grains. In order to achieve a voided grain structure the seed layer has to be sputtered using two process pressures where the process pressure of the second layer has to be x10 higher than that for the first layer. Ru was used as the seed layer and sputtered using the process pressures of 3mTorr and 30mTorr, respectively. A median grain size of D_m = (6.2 ± 0.2)nm with standard deviation of 0.22 was achieved.

An insignificant exchange bias of less than H_{ex} = 100Oe was observed in the CoCrPt alloy using the dual Ru seed layer based samples. Follow a report of Chen et al. a trend were made by 2 atoms using Co to induce perpendicular spin alignment in the IrMn. However to achieve the 2-ion anisotropy of the Co layer it is necessary to grow on a Pt seed. This structure was found to be successful to inducing an exchange bias in CoCrPt alloy. The structure was optimised and found that 6nm of IrMn and 3nm of CoCrPt-SiO$_2$ gave the best result of the loop shift of H_{ex} = (240 ± 5)Oe with a squareness of 0.75. Importantly both H_{c1} and H_{c2} were shifted to a negative values of the applied field. However the use of Pt seed layer does not allow the generation of voided grain structure even though a dual seed layer were used. This important result is reproduced as below.
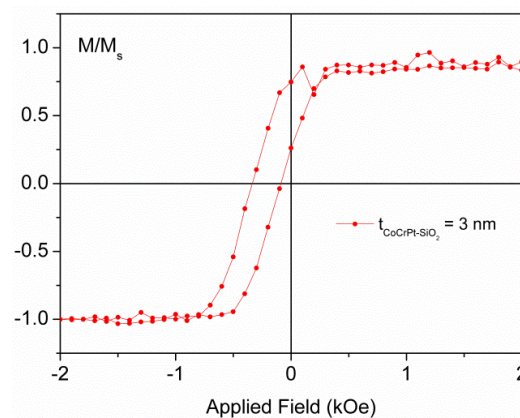
Figure 7.1 Room temperature hysteresis loop measurements.

The data shown in Figure 7.1 is an important result because the squareness of the loop persists after the application of a negative magnetic field. This system is incapable of being de-magnetised by any magnetic field and thermal energy is always required to change the order. The degree of the order is in the AF and hence the data storage in this layer is not in the F layer. The F layer becomes part of both the read and write structure. The data shown in Figure 7.1 indicates the thermal stability of the magnetic properties by holding the magnetic layer in negative saturation for 30mins. No change in the hysteresis loop was observed.

7.2 Future Work

A complete loop shift was also observed using Co/Pt multilayers. This thin film exhibits with polycrystalline structure which cannot be used in HAMR media. In patterned media the data is stored in a distinct single dot by changing its magnetisation orientation. Therefore a segregated grain structure is not required in this recording system. Since a thermal stability experiments were taken to show that the samples were thermally stable this system could possibly form a patterned HAMR medium.

Whilst it is not our aim to produce a material that would be a functional recording system, our interpretation is that the parameter $M_r\delta$ is the key parameter. Given that we have to reduce the thickness of the layer below that typically used in a conventional disc there is an obvious resolution to this issue by increasing the value of M_r so that the product $M_r\delta$ would remain approximately constant. We believe this can be achieved quite readily by lowering the Cr content in the recording layer. However within the context of this project and within the timescale remaining, we will examine this aspect by tuning the Cr content in future work. Importantly it has been demonstrated that a recording layer as thin as 4nm is capable of generating a sufficient exchange field so as to align the grains in the IrMn layer. Hence the feasibility of using the exchange bias effect has been further demonstrated.

Ideally we would like the values of squareness to be higher than 0.75. This may be possible by increasing the anisotropy of the CoCrPt alloy (ie increasing the Pt content). A segregated grain structure will also be required because with a

continuous layer there would be a risk that the spread of the magnetisation across more than one AF grain would broaden the transition. Hence a segregated F layer is required but this would need further experimentation as Ru is the only material known to produce this effect.

One of the unexplained issues is the role of the 2-atom layer of Co on top of the Pt seed layer. It has been suggested that this may be either a crystallographic or in some way a magnetic effect. This phenomenon should be studied by examining the effect of inserting a non-magnetic or magnetic layer with a similar structure between the seed layer and the IrMn. There will be few potential materials to achieve this such as Mn or CoFe. However further experimental studies are require to explain this phenomenon.

Reference to previous work undertaken in our laboratories on Heusler alloys shows that the level of shearing of the loop and in fact the degree of shift of the loop, can be significantly enhanced by the insertion of a monolayer of Mn between the F and AF layers. It is obvious that the use of such a Mn layer may have a similar effect on the systems under study here. It should be noted that the mechanism by which Mn causes this effect is not well understood. There are two possibilities, the first being that the Mn replaces a compositional deficiency in the IrMn arising from diffusional effects and the second being that the presence of the high moment Mn atoms leads to a magnetically stiffer interface with a stronger coupling between the F and AF layers. However this phenomenon was no observed in this study. Therefore the interfacial effect of the Mn layer should be further investigated in future.

Acronyms

Alternative current (ac)

Antiferromagnetic (AF)

Anisotropy magnetoresistance (AMR)

Bit patterned magnetic recording (BPM)

Charge-couple device (CCD)

Compound annual growth rate (CGR)

Coupled granular continuous (CGC)

Demagnetisation remanence curve (DCD)

Direct current (dc)

Discrete track media (DTM)

X-ray spectroscopy (EDX)

Exchange coupled composite (ECC)

Extraordinary Hall Effect (EHE)

Ferromagnetic (F)

Face centre cubic (fcc)

field generation layer (FGL)

Hard disk drives (HDDs)

Heat assisted magnetic recording (HAMR)

Hexagonal close-packed (hcp)

High Target Ulitration Sputtering (HiTUS)

Isothermal remanence curve (IRM)

Laudau-Lifshitz-Gilbert (LLG)

Longitudinal recording media (LRM)

Microwave assisted magnetic recording (MAMR)

Magneto-optical Kerr effect (MOKE).

Perpendicular recording media (PRM)

Proportional-integral-derivative *(*PID)

Precision Ion Polishing System (PIPS)

Radio frequency (RF)

Ruderman-Kittel-Kasuya-Yosida (RKKY)

Scanning electron microscope (SEM)

Switching field distribution (SFD)

Spin-torque transfer (STT)

Signal to noise ratio (SNR)

Soft underlayer (SUL)

Tunnelling Magneto Resistance (TMR)

Transmission Electron Microscopy (TEM)

Tunnelling Magneto Resistance (TMR)

X-ray diffraction (XRD)

X-ray reflectivity (XRR)

List of Symbols

A Area

A_{ex} Exchange stiffness

a Lattice constant

a_0 Transition width

a_w The Williams-Comstock transition width parameter

B_M Magnetic flux density

B_L Bit length

C^* Scaling factor

D Grain diameter

D_a Average grain diameter

$\overline{D}$ Mean grain diameter

D_m Median grain size

D_w Width of a domain wall

d_s Spacing between the head and medium

d Lattice spacing

E_a Anisotropy energy

E_{ms} Magnetostatic energy

E_{iex} Interfacial exchange energy

E_{wall} Domain wall energy

E_{ex} Exchange energy

ΔE Energy barrier

E_K Magnetocrystalline anisotropy energy

E_Z Zeeman energy

ΔF Change in frequency

F_c Coated resonant frequency of the quartz sensor

F_q Uncoated resonant frequency of the quartz sensor

f Resonant frequency

f_0	Attempt frequency
G	Growth rate
H	Applied field
H_{ac}	Microwave ac field
H_c	Coercivity
H_{cr}	Remanent coercivity
H_D	Demagnetisation field
H_n	Nucleation field
H_{GD}	Global demagnetising field
H_K^*	Pseudo anisotropy field
H^*	Exchange field from a ferromagnetic layer
H_K	Anisotropy field
H_S	Switching field
H_w	Write field
H_{ex}	Loop shift
H_I	Internal field
h_m	Flying height
J_{ex}	Exchange integral
K	Magnetocrystalline anisotropy constant
K_{AF}	Antiferromagetic anisotropy constant
K_g	Scattering vector
K_u	Uniaxial anisotropy constant
K_U	Total anisotropy constant
k_B	Boltzmann's constant
L	Effective length
M_s	Saturation magnetisation
M	Magnetisation
M_r	Remanent magnetisation

M_f Mass difference

M_q Original mass

N Number of turns

N_r Nucleation rate

N_{at} Frequency constant of the quartz sensor

n^* Refractive index

PW_{50} Width of the signal pulse at 50% amplitude

$Q_\perp$ Head field gradient

l Length

R Radius of diffraction ring

R^* Refractive index

r_A Radius of an atom

r_{3d} Radius of 3d shell

T Temperature

$< T_B >$ Median blocking temperature

T_{ms} Measurement temperature

TF_i Initial tooling factor

T_{NA} Temperature with no activation

T_{Act} Acting temperature

T_{set} Setting temperature

T_B Blocking temperature

T_c Curie temperature

t Time

Δt Surface roughness

t_0 Thickness

t_a Actual deposited thickness

t_{Act} Activation time

t_c Thickness displayed on the deposited monitor

t_{FGL} Field generation layer thickness

t_{ms} Measurement time

t_{set} Setting time

t_f Film thickness

V Volume

$<V>$ Mediam volume

V_{Act} Activated Volume

V_c Minimum AF grain volume which is thermally stable

V_{set} Maximum AF grain volume that can be set

V_m Median volume of the grains

W_{read} Read width

W_{write} Track width

W_{FGL} Field generation layer width

Y Young's modulus

Z Acoustic impedance ratio

α_a Alignment factor

α Ratio of the transition width to the grain diameter

β Semi-angle

δ Smallest distance resolution

δ_t Thickness of the granular layer

δ_{med} Thickness of the medium

ε Induced electromotive force

θ Scattering angle

θ_U Angle between easy axis and magnetisation

λ Wavelength

μ Mean

μ_0 Permeability of free space

ρ Density

ρ_q Density of deposited film

σ Standard deviation

σ^* Standard deviation of the normalised grain size distribution

σ_w Domain wall energy per unit area of wall

φ Flux

φ_W Work function

τ Relaxation time

Reference

[1] J. D. Dutson, D. Litvinov, M. R. J. Gibbs, Y. Inaba, H. Muraka and K. O'Grady, J. Magn. Magn. Mater., 304, 51-54, (2006).

[2] H. J. Richter, J. Phys, D: Appl. Phys., 40, 9, R149, (2007).

[3] Seagate Research, Private communication.

[4] D. Weller, G. Parker, O. Mosendz, E. Champion, B. Stipe, X. Wang, T. Klemmer, G. Ju and A. Ajan, IEEE Trans. Magn., 50, 1, 3100108 (2014).

[5] Y. J. Xu, J. Zhang, J. R. Shi, R. Ji and J. P. Wang., J. Appl. Phys. 91, 8337, (2002).

[6] T. Klemmer, Y. Peng, X Wu, and G. Ju, IEEE Trans. Magn., 45,2, (2009).

[7] M. H. Kryder, E. C. Gage, T. W. McDaniel, W. A. Challener, R. E. Rottmayer, G. Ju, Y-T Hsia and M. F. Erden, IEEE Trans. Magn., 96, 11, (2008).

[8] N. P. Aley, G. Vallejo-Fernandez, R. Kroeger, B. Lafferty, J. Agnew, Y. Lu, K. O'Grady. IEEE Trans. Magn., 44, 11, 2820-2823, (2008).

[9] A. Moser, K. Takano, D. T. Margulies, M. Albrecht, Y. Sonobe, Y. Ikeda, S. Sun, E.E. Fullerton, J. Phys. D: Appl. Phys., 35, R157. (2002).

[10] H. N. Bertram, H. Zhou and R. Gustafson, IEEE Trans. Magn., 34, 4, 1845-1847, (1998).

[11] The International Disk Drive Equipment and Materials Association, ASTC Technology Road Map, http://idema.org/?page_id=5868. (2016).

[12] S. H. Charap, P-L. Lu and Y. He, IEEE Trans. Magn., 33, 1, (1997).

[13] E. C. Stoner and E. P. Wohlfarth, Phil. Trans. Roy. Soc. London., 240, 826, 599-642, (1948).

[14] S. Iwasaki, K. Takemura, IEEE Trans. Magn., 11, 1173, (1975).

[15] S. Iwasaki, Y. Nakamura, IEEE Trans. Magn., 14, 436, (1978).

[16] S. Iwasaki, Y. Nakamura, K. Ouchi, IEEE Trans. Magn., 15, 1456, (1979).

[17] S. N. Piramanayagam, J. Appl. Phys., 102, 011301, (2007).

[18] S. N. Piramanayagam, K. Srinivasan, J. Magn. Magn. Mater., 321, 485-494, (2009).

[19] J. Chureemart "Orientation and Thermal Stability of Advanance Recording Media", Ph.D. Thesis, The University of York, (2013).

[20] Y. Sonobe, D. Weller, Y. Ikeda, M. Schabes, K. Takano, G. Zeltzer, B. Yen, M. E. Best, S. Greaves, H. Muraoka, and Y. Nakamura, IEEE Trans. Magn., 37, 4, 1667-1670, (2001).

[21] J. Yasumori, Y. Sonobe, S. J. Greaves, and K. K. Tham, IEEE Trans. Magn., 45, 850 – 855, (2009).

[22] K. K. Tham, Y. Sonobe and K. Wago, IEEE Trans. Magn., 43, 2, (2007).

[23] H. Muraoka, Y. Sonobe, K. Miura, A. M. Goodman, and Y. Nakamura, IEEE Trans. Magn., 38, 4, 1632-1636, (2002).

[24] Y. Sonobe, H. Muraoka, K. Miura, Y. Nakamura, K. Takano, A. Moser, H. Do, B. Yen, Y. Ikeda, N. Supper, and W. Weresin, IEEE Trans. Magn., 38, 5, 2006-2011, (2002).

[25] H. J. Richter, J. Phys D: Appl. Phys., 32, 21, R147, (1999).

[26] Y. Y. Zou, J. P. Wang, C. H. Hee, and T. C. Chong, Appl. Phys. Lett., 82, 15, 2473-2475, (2003).

[27] K. Z. Gaond H. Bertram, IEEE Trans. Magn., 39, 2, 704-709, (2003).

[28] R. H. Victora and X. Shen, IEEE Trans. Magn., 41, 10, 2828-2833, (2005).

[29] R. H. Victora and X. Shen, IEEE Trans. Magn., 41, 2, 537-542, (2005).

[30] D. Suess, T. Schrefl, S. Fahler, M. Kirschner, G. Hrkac, F. Dorfbauer, and J. Fidler, Appl. Phys. Lett., 87, 1, 012504, (2005).

[31] J. P. Wang, W. Shen and J. Bai, IEEE Trans. Magn., 41, 10, 3181-3186, (2005).

[32] D. Suess, J. Lee, J. Fidler, T. Schrefl, J. Magn. Magn. Mater., 321, 545-554, (2009).

[33] J. P. Wang, W. Shen, and S-Y Hong, IEEE Trans. Magn., 43, 2, (2007).

[34] R. L. White, R. M. H. New, R. F. W. Pease, IEEE Trans. Magn., 33, 1, 990, (1997).

[35] B. D. Terris and T. Thomson, J. Phys. D: Appl. Phys., 38(12), R199, (2005).

[36] X. Chen and M. Tomizuka, International Federation of Automatic Control, 5279-5285, (2011).

[37] A. Kikitsu, J. Magn. Magn. Mater., 321, 526-530, (2009).

[38] R. Wood, Magnetic recording. Presented at IEEE magnetics society summer school, (2011).

[39] Y. Kamata, A. Kikitsu, H. Hieda, M. Sakurai, K. Naito, J. Bai, S. Ishio, Jpn. J. Appl. Phys., 46, 999, (2007).

[40] Y. Shiroishi, K. Fukuda, I. Tagawa, H. Iwasaki, S. Takenoiri, H. Tanaka, H. Mutoh, and N. Yoshikawa, IEEE Trans. Magn., 45, 10, 3816-3822, (2009).

[41] J. G. Zhu, X. Zhu, and Y. Tang, IEEE Trans. Magn., 44, 1, 125-131, (2008).

[42] C. Thirion, W. Wernsdorfer, and D. Mailly, Nature Mater., 2, 524-527, (2003).

[43] S. Okamoto, N. Kikuchi, and O. Kitakami, in Proc. HW-03, Intermag 2008, Madrid, Spain, (2008).

[44] Y. Tang and J. -G. Zhu, IEEE Trans. Magn., 44, 11, 3376-3379, (2008).

[45] S. Anthony, "Seagate hits 1 terabit per square inch, 60TB hard drives on their way", http://www.extremetech.com/computing/122921-seagate-hits-1-terabit-per-square-inch-60tb-drives-on-their-way (2012).

[46] K. Inoue, H. Shima, A. Fujita, K. Ishida, K. Oikawa and K. Fukamichi, Appl. Phys. Lett., 88, 102503, (2006).

[47] L. Zhang, Y. K. Takahashi, A. Perumal, K. Hono, J. Magn. Magn. Mater., 322, 2658-2664, (2010).

[48] M. H. Kryder, E. C. Gage, T. W. McDaniel, W. A. Challener, R. E. Rottmayer, G. Yu, Y.-T. Hsia and M. F. Erden, IEEE Trans. Magn., 96, 11, 1810-1835, (2008).

[49] W. Challener, C. Mihalcea, C. Peng, and K. Pelhos, Opt. Exp., 13, 7189–7197, (2005)

[50] R. Rottmayer, S. Batra, D. Buechel, W. Challener, J. Hohlfeld, Y. Kubota, L. Li, B. Lu, C. Mihalcea, K. Mountfield, K. Pelhos, C. Peng, T. Rausch, M. A. Seigler, D. Weller, and X. Yang, IEEE Trans. Magn., 42, 10, 2417 – 2421, (2006).

[51] D. Weller, H. Brandle, G. Gorman, C. -J. Lin, H. Notrays, Appl. Phys. Lett., 61, 2726, (1992).

[52] J.-M. Qiu, J. H. Judy, D. Weller, J. –P. Wang, J. Appl. Phys., 97, 10J319, (2005).

[53] N. Shukla, C. Liu, A. G. Roy, Mater. Lett., 60, 995, (2005).

[54] S. N. Piramanayagam and K. Srinivasan, Appl. Phys. Lett., 91, 142508, (2007).

[55] W. K. Shen, J. H. Judy, J. P., J. Appl. Phys., 97, 10H301, (2005).

[56] D. Weller, O. Mosendz, G. Parker, S. Pisana and T. S. Santos. Physica Stat Sol (a), 210, 1245-1260, (2013).

[57] http://techon.nikkeibp.co.jp/english/NEWS_EN/20121002/243229/ Oct (2012).

[58] R. Ruiz, H. Kang, F. A. Detcheverry, E. Dobisz, D. S. Kercher, T. R. Albrecht, J. J. de Pablo, and P. F. Nealey, Science, 321, 936, (2008).

[59] K. O'Grady, L. E. Fernandez-Outon, G. Vallejo-Fernandez, J. Magn. Magn. Mater, 322, 883-899, (2010).

[60] B. D. Cullity and C. D. Graham, 2nd ed. John Wiley and Sons Ltd., Inc., Hoboken, New Jersey., (2009).

[61] J. Chureemart, P. Chureemart, R. Evans, R. W. Chantrell and K. O'Grady, J. Phys. D: Appl. Phys., 44, 45, 455002, (2011).

[62] J-M. Meaujour, C. Tran, D. Weller, B. York and B. Gurney, IEEE Trans. Magn., 52, 2, (2016).

[63] S. Emori and G. S. D. Beach, J. Appl. Phys., 110, 033919, (2011).

[64] J. Akerman, Science 308, (5721), 508, (2005).

[65] A. D. Kent, Nat. Mater. 9(9), 699, (2010).

[66] T. N. A. Nguyen, Y. Fang, V. Fallahi, N. Benatmane, S. M. Mohseni, R. K. Dumas, and J. Akerman, Appl. Phys. Lett., 98(17), 172502 (2011).

[67] T. R. Albrecht, D. Bedau, E. Dobisz, H. Gao, M. Grobis, O. Hellwig, D. Kercher, J. Lille, E. Marinero, K. Patel, R. Ruiz, M. E. Schabes, L. Wan, D. Weller, and T. W. Wu, IEEE Trans. Magn., 49(2), 773, (2013).

[68] O. Hellwig, E. E. Marinero, D. Kercher, T. Hennen, A. McCallum, E. Dobisz, T. W. Wu, J. Lille, T. Hirano, R. Ruiz, M. K. Grobis, D. Weller, and T. R. Albrecht, J. Appl. Phys. 116(12), 123913, (2014).

[69] C. W. Barton and T. Thomson, J. Appl. Phys., 118, 063901, (2015).

[70] V. Vopsaroiu, G. Vallejo Fernandez, M. J. Thwaites, J. Anguita, P. J. Grundy and K. O'Grady, J. Phys. D: Appl. Phys, 38, 490-496, (2005).

[71] M. A. Ruderman and C. Kittel, Phys. Rev., 96, 99, (1954).

[72] T. Kasyua, Prog. Theor. Phys., 16, 45, (1956).

[73] K. Yoshida, Phys. Rev., 106, 893, (1957).

[74] E. Fulcomer, S. H. Charap, J. Appl. Phys., 43, 4190, (1972).

[75] E. Fulcomer, S. H. Charap, J. Appl. Phys., 43, 4184, (1972).

[76] G. Vallejo-Fernandez, N. P. Aley, J. N. Chapman and K. O'Grady, Appl. Phys. Lett., 97, 222505, (2010).

[77] A. Johnstone, Seagate Technology, private communication.

[78] A. Kohn, A. Kovacs, R. Fan, G. J. Mclntyre, R. C. C. Ward, and J. P. Goff, Nature Scientific Reports, 1-7, (2013).

[79] G. Vallejo-Fernandez, L. E. Fernandez-Outon and K. O'Grady, J. Phys. D: Appl. Phys., 41, 112001, (2008).

[80] G. Vallejo-Fernandez, L. E. Fernandez-Outon and K. O'Grady, Appl. Phys. Lett., 91, 212503, (2007).

[81] L. William, R. L. Comstock, AIP Conference, 5, 738, MAG-14, 861, (1971).

[82] R. W. Chantrell and K. O'Grady, J. Phys. D: Appl. Phys., 25, 1, 1, (1992).

[83] D. Weller and A. Moser, IEEE Trans. Magn., 35, 6, 4423-4439, (1999).

[84] P. Chureemart, E. F. L. Evans, R. W. Chantrell and K. O'Grady, J. Phys. D: Appl. Phys., 44, 45, 455002, (2011).

[85] A. M. de Witte, M. El-Hilo, K. O'Grady and R. W. Chantrell, J. Magn. Magn. Mater., 120, 184-186, (1993).

[86] M. Vapsaroiu, M. J. Thwaites, G. Vallejo-Fernandez, S. Lepadatu and K. O'Grady, J. Opt. and Adv. Mat., 7, p.2713, (2005).

[87] W. A. Johnson and R. F. Mehl, Trans. Am. Inst. Min. Eng., 135, 416, (1939).

[88] C. V. Thompson, Ann. Rev. Mater. Sci. 30, 159, (2000).

[89] G. Z. Sauerbrey, Phys. Verhand., 8, 193, (1957).

[90] C. Lu, Lewis O., J. Appl. Phys., 43, 4385, (1972).

[91] N. Paul Aley, "Structure and anisotropy in exchange bias system" Ph.D. dissertation, Department of Physics, The University of York, (2009).

[92] H. Zijilstra, Rev. Sci. Insts., 41, 1241, (1970).

[93] P. J. Flanders, Rev. Sci. Instrum., 61, 839-847, (1990).

[94] P. J. Flanders, J. Appl. Phys., 63, 3940-3945, (1988).

[95] S. Foner, Rev. Sci. Insts., 30, 7, 548-557, (1959).

[96] VSM Safety Manual Booklet.

[97] K. O'Grady, R. W. Chantrell, I. L. Sanders. IEEE Trans. Magn., 29, (1), 286, (1993).

[98] Jing Wu, L. Holloway, H. Laidler, K. O'Grady, S. Khizroev, J. K. Howard, R. W. Gustafson, D. Litvinov, IEEE Trans. Magn., 38, 4, (2002).

[99] T. Deakin, C. Bunce, S. Z. Wu, K. O' Grady, IEEE Trans. Magn., 44, 11, (2008).

[100] R. J. M. van de Veerdonk, X. Wu and D. Weller, IEEE Trans. Magn., 38, 12, 2450-2452, (2002).

[101] L. E. Fernandez-Outon, K. O'Grady and M. J. Carey, J. Appl. Phys., 95, 6852, (2004).

[102] David B. Williams, C. Barry Carter, Transmission electron microscopy, vol 1.

[103] R. C. Weast, M. J. Astle, W. H Beyer, Handbook of Chemistry and Physics, 64th edition, (1983 – 1984).

[104] M. Tsunoda, K. Imakita, M. Naka and M. Takahashi, J. Magn. Magn. Mater., 304, 59, (2006).

[105] N. P. Aley and K. O'Grady, J. Phys. D: Appl. Phys., 109, 07D719, (2011).

[106] K. O'Grady and A. Bradbury, J. Magn. Magn. Mater., 39, 91-94, (1983).

[107] Rigaku Automated Multipurpose X-ray Diffractometer Instruction Manual.

[108] Rigaku Official Web Page, http://www.rigaku.com/en/products/xrd/smartlab/app025.

[109] K. Nagao and E. Kagami, X-ray thin film measurement techniques VII. Pole figure measurement, The Rigaku Journal, 27(2), 2011.

[110] Rigaku Film Thickness Analysis User Manual Booklet.

[111] Rigaku Global Fit Reflectivity Analysis User Manual Booklet.

[112] Y. F. Liu, J. W. Cai and S. L. He, J. Phys. D: Appl. Phys., 42, 115002, (2009).

[113] S. Maat, K. Takano, S. S. P. Parkin and Eric E. Fullerton, Phys. Rev. Lett., 87, 8, (2001).

[114] O. Hellwig, T. Hauet, T. Thomson, E. Dobisz, J. D. Risner-Jamtgaard, D. Yaney, B. D. Terris and E. E. Fullerton, Appl. Phys. Letts., 95, 232505, (2009).

[115] C. W. Barton, T. J. A. Slater, R. M. Rowan-Robinson, S. J. Haigh, D. Atkinson and T. Thomson, J. Appl. Phys., 116, 203903 (2014).

[116] J-Y. Chen, J-F. Feng, Z. Diao, G. Feng, J. M. D. Coey and X-F. Han, IEEE Trans. Magn., 46, 6, (2010).

[117] X. Peng, A. Morrone, K. Nikolaev, M. Kief, M. Ostrowski. J. Magn. Magn. Mater. 321, 2902, (2009).

[118] J. Chatterjee, T. Tahmasebi, S. Mertens, G. S. Kar, T. Min and J. De Boeck. IEEE Trans. Magn., 50, 11, (2014).

[119] J. Sagar, C. N. T. Yu, L. Lari and A. Hirohata, J. Phys. D: Appl. Phys., 47, 265002 (2014).

[120] S. van Dijken, M. Besnier, J. Moritz and J. M. D. Coey, J. Appl. Phys., 97, 10K114 (2005).

[121] J. V. Harzer, B. Hillebrands, R. L. Stamps, G. Guntherodt, D. Weller, Ch. Lee, R. F. C. Farrow and E. E. Marinero, J. Magn. Magn. Mater., 104-107, 1863-1864, (1992).

[122] H. Momiji, K. Akagi, K. Adachi, M. Futamoto, J. Magn. Magn. Mater. 182, 396-402, (1998).

[123] T. Klemmer, Seagate Media Research (Fremont). (Private communication)

[124] J. Y. Chen, N. Thiyagarajah, H. J. Xu and J. M. D. Coey, Appl. Phys. Lett., 104, 152405, (2014).

[125] J. Nogues, Ivan K. Schuller, J. Magn. Magn. Mater., 192, 203-232, (1999).

[126] R. Stearett, W. G. Wang, X. Kou, J. F. Feng, J. M. D. Coey, J. Q. Xiao, and E. R. Nowak, Phys. Rev. B, 86, 1–11, (2012).

[127] T. Thomson, Manchester University, Private communication.